

Advanced chemical investigations of the volatile element flerovium (Fl, Z=114)

Dissertation
zur Erlangung des Grades
“Doktor der Naturwissenschaften”
im Promotionfach Kernchemie

am Fachbereich Chemie, Pharmazie und Geowissenschaften
der Johannes Gutenberg-Universität
in Mainz



Lotte H. L. Lens

geb. in Port-Elizabeth, Südafrika

Mainz, den 10. Dezember 2018

Abstract

The determination of the chemical properties of flerovium (Fl, Z=114) is a topic of high interest for theoretical as well as experimental research. Due to the relativistic stabilization of the quasi-closed electron shell configuration of Fl, early theoretical calculations predicted it to be inert and volatile like a noble gas. More recent calculations predict Fl to be more volatile than its lighter homolog Pb or than Hg. Nevertheless, it is expected to have a distinct metallic character. Previous experiments provided incompatible conclusions. Whereas one experiment, in which three decay chains attributed to Fl were registered was interpreted to show that Fl is noble-gas like, a second one -performed by a different group- recorded two chains and inferred metallic properties. This conflict motivated our recent and improved experiments with the goal to clarify the chemical behavior of Fl.

The isotopes $^{288,289}\text{Fl}$ were produced in a fusion evaporation reaction by bombarding a ^{244}Pu target with ^{48}Ca projectiles. By using the gas-filled recoil separator TASCAs, in combination with the COMPACT gas chromatography detector setup, it was possible to detect the characteristic α and spontaneous fission (SF) fragments under almost background free conditions. In order to obtain better statistics for Fl and to compare its chemical behavior with elements of a wide volatility range, the experimental setup was optimized and the chemical separation in the detector channel was improved. The optimizations were tested with short-lived isotopes of Hg, and Pb, as also with Tl as pre-test for future nihonium (Nh, Z=113) studies. The experiments were performed under the same experimental conditions as used for the Fl studies. The produced isotopes passed through TASCAs, were thermalized inside a stopping chamber and flushed together with a carrier gas into a series of COMPACT detectors covered with SiO_2 and Au surfaces. The detectors were operated at room temperature (21°C) as also a negative temperature gradient was applied along the detectors. As a result of the optimizations the transportation time in the setup was reduced significantly, and the overall chemical yield was doubled. By using COMPACT detector arrays with different surfaces a good chemical separation between the non-volatile metal Pb and the volatile metal Hg was achieved. This allowed to directly compare the chemical behavior of Fl with those of non-volatile to very volatile elements (e.g. Rn). Two successful Fl experiments were performed, in which six decay chains attributed to $^{288,289}\text{Fl}$ were observed. Furthermore, three incomplete chains of ^{289}Fl starting from ^{285}Cn were observed as well as eight spontaneous fissions. The distribution of the Fl decay chains in the COMPACT setup showed two deposition zones, three Fl events were observed on the Au surface at room temperature, and the other three on a thin ice layer covering the Au. In order to understand the adsorption behavior of Fl on the Au surface, a dedicated analysis was performed. The analysis showed that the Au layer presented an inhomogeneous structure, with different grain sizes, heights and different crystallite orientations. Studies of the adsorption process of Hg on an inhomogeneous Au surface described in the literature, indicate that Hg atoms diffuse to an energetically more favorable position on the surface (e.g. grain boundary or defect). An extended Monte Carlo Simulation (MCS) code, which included the diffusion

step, was developed. It provided a good description of the experimentally determined Hg distributions. The MCS adapted to the FI experiments could reproduce well the two deposition zones of the FI deposition on the real inhomogeneous Au surface. This led to the conclusion that FI is a volatile element weakly bound to Au, however shows a metallic character on energetically favorable sites of the Au surface.

Zusammenfassung

Die Bestimmung der chemischen Eigenschaften von Flerovium (Fl, $Z=114$) ist sowohl für die theoretische als auch für die experimentelle Forschung von großem Interesse. Aufgrund der relativistischen Stabilisierung der quasi-geschlossenen Elektronenschalenkonfiguration von Fl sagten frühe theoretische Berechnungen voraus, dass Fl chemisch inert sei. Neuere relativistische Berechnungen besagen ebenfalls ein weniger reaktives Verhalten als sein leichteres Homologes Pb, es soll aber dennoch einen ausgeprägten metallischen Charakter aufweisen. Experimentell konnte aufgrund von widersprüchlichen Schlussfolgerungen noch keine eindeutige Klärung herbeigeführt werden. In einem Experiment, in dem drei Zerfallsketten Fl zugeordnet wurden, wurde ein Edelgas ähnliches Verhalten für Fl vorhergesagt. In einem zweiten Experiment, welches von einer anderen Gruppe durchgeführt und zwei Zerfallsketten von Fl detektiert wurden, wurde ein metallischer Charakter impliziert. Dieses Konflikt, motivierte unsere jüngsten und verbesserten Experimente mit dem Ziel das chemische Verhalten von Fl aufzuklären.

Die Isotope $^{288,289}\text{Fl}$ wurden in einer Fusionsverdampfungsreaktion erzeugt, indem ein ^{244}Pu -Target mit ^{48}Ca -Projektilen beschossen wurde. Durch die Verwendung des Gas gefüllten Rückstoßseparators TASCA in Kombination mit hintereinander geschalteten COMPACT Gas Chromatographie Detektoren, war es möglich die charakteristischen α und Spontan Spaltungs Fragmente (SF) bei untergrundfreien Bedingungen zu messen. Um eine bessere Statistik für Fl zu erhalten und sein chemisches Verhalten mit Elementen eines breiten Flüchtigkeitsbereichs zu vergleichen, wurde der Versuchsaufbau optimiert und die chemische Trennung im Detektorkanal verbessert. Die Optimierungen wurden anhand von kurzlebigen Isotopen von Hg und Pb getestet. Desweiteren wurden Vorstudien mit Tl durchgeführt für zukünftige chemische Untersuchungen mit Nihonium (Nh, $Z=113$). Die Experimente wurden unter identischen Bedingungen durchgeführt, wie sie für die Fl-Studien verwendet wurden. Die produzierten Isotope wurden nachdem sie durch TASCA geflossen waren in einer Kammer gestoppt und mithilfe eines Trägergases in die COMPACT Detektoren welche mit SiO_2 und Au beschichtet waren transportiert. Die Detektoren wurden bei Raumtemperatur (21°C) sowie mit einem negativen Temperaturegradienten betrieben. Die Ergebnisse der Optimierungen zeigten, dass die Transportzeit im experimentellen Aufbau signifikant reduziert und die chemische Ausbeute verdoppelt wurde. Durch die Verwendung von COMPACT Detektoren mit verschiedenen Oberflächen, konnte eine gute chemische Trennung zwischen dem nicht-flüchtigen Metall Pb und dem flüchtigen Metall Hg erreicht werden. Dieser erstmalig verwendete experimentelle Aufbau ermöglichte es, das chemische Verhalten von Fl unmittelbar mit dem Verhalten von nicht-flüchtigen bis hin zu sehr flüchtigen Elementen (z.B. Rn) zu vergleichen. Zwei erfolgreiche Fl Experimente wurden durchgeführt, in denen sechs vollständige Zerfallsketten von $^{288,289}\text{Fl}$ detektiert wurden. Darüber hinaus wurden drei unvollständige Ketten ausgehend von ^{285}Cn beobachtet, sowie acht koinzidente Spontan Spaltungs Fragmente. Die Verteilung der Fl Zerfallsketten in den COMPACT Detektoren zeigten zwei

Depositionszonen, eine auf der Au-Oberfläche bei Raum Temperatur und die Andere auf einer dünnen Eisschicht, die das Au bedeckte. Um das Adsorptionsverhalten von FI auf der Goldoberfläche zu verstehen, wurde eine umfangreiche Oberflächenanalyse durchgeführt. Die Analysen zeigten eine inhomogene Au-Schicht, deren Struktur verschiedene Korngrößen, Höhen und unterschiedliche Kristallorientierungen aufwies. Untersuchungen des Adsorptionsprozesses von Hg an einer inhomogenen Au-Oberfläche zeigten, dass Hg-Atome an eine energetisch günstigere Stelle auf der Oberfläche diffundieren können, wie z.B. an eine Korngrenze oder einen Defekt. Ein erweiterter Monte Carlo Simulations (MCS) Code, der den Diffusionschritt enthielt, wurde entwickelt. Die experimentell bestimmten Hg-Verteilungen konnten durch die Simulationen sehr gut beschrieben werden. Die MCS wurde an die FI-Experimente angepasst und konnte die beiden Depositionszonen von FI auf der realen inhomogenen Au-Oberfläche gut reproduzieren. Dies führte zu der Schlussfolgerung, dass FI ein flüchtiges Element ist, welches schwach an Au gebunden ist, jedoch einen metallischen Charakter an energetisch günstigen Stellen der Au-Oberfläche aufweisen kann.

Contents

Abstract	1
1 Introduction	11
1.1 Stability of SHE	11
1.1.1 Liquid Drop Model	12
1.1.2 Nuclear Shell Model	12
1.1.3 Corrections to the Nuclear Shell Model	14
1.1.4 SHE region	15
1.2 Production of SHE in nuclear fusion reactions	16
1.3 Chemical properties of SHE	19
1.3.1 Relativistic effects	19
1.4 Chemical investigation techniques	20
1.4.1 Chromatographic methods and adsorption	22
1.4.2 Monte Carlo Simulation	24
1.5 Investigation of flerovium (Fl, Z=114)	26
1.5.1 Production and decay	26
1.5.2 Theoretical predictions of the adsorption behavior	28
1.5.3 Previous experimental results	30
2 Experimental setup	33
2.1 TASCA - TransActinide Separator and Chemistry Apparatus at UNILAC	33
2.2 Detection system: Focal Plane Detector	36
2.3 Recoil Transfer Chamber and Gas- Transport System	37

2.4	Detection system: COMPACT	40
2.5	Data acquisition system	42
3	Technical optimizations of the experimental setup	45
3.1	Technical Optimizations	46
3.1.1	TASCA	46
3.1.2	Recoil Transfer Chamber	46
3.1.3	Gas Chromatography and Detection System COMPACT	48
3.1.4	Gas- Transport System	50
3.2	Online and Offline Experiments	50
3.3	Analysis	54
3.3.1	Transportation time	54
3.3.2	Overall chemical efficiency	55
3.4	Results	56
3.5	Discussion	58
4	Chemical adsorption studies of Hg, Tl, and Pb on SiO₂ and Au surfaces	63
4.1	Previous experimental results of studies on Hg, Tl, and Pb	63
4.2	Experiments and Methods	64
4.2.1	Experimental setup	64
4.2.2	Monte Carlo Simulation parameters	66
4.2.3	Background reduction	67
4.3	Adsorption of Hg on SiO ₂ and Au surfaces	68
4.3.1	Results	68
4.3.2	Discussion	68
4.4	Adsorption of Pb on SiO ₂ and Au surfaces	71
4.4.1	Results	71
4.4.2	Discussion	72
4.5	Adsorption of Tl on SiO ₂ and Au surfaces	73

4.5.1	Results	73
4.5.2	Discussion	74
5	Adsorption on a real gold surface- Analysis of the COMPACT gold layer	77
5.1	Analytical Methods	77
5.1.1	Scanning Electron Microscopy and Energy Dispersive X-ray spectroscopy (SEM-EDX)	77
5.1.2	X-ray photoelectron spectroscopy (XPS)	78
5.1.3	X-ray diffraction spectroscopy (XRD)	78
5.1.4	Atomic force microscopy (AFM)	79
5.2	Previous experimental results on studies of a Au layer	79
5.3	Results of the COMPACT Au layer measurements	80
5.3.1	Scanning Electron Microscopy and Energy dispersive X-ray spectroscopy (SEM-EDX)	80
5.3.2	X-ray photoelectron spectroscopy (XPS)	81
5.3.3	X-ray diffraction spectroscopy(XRD)	82
5.3.4	Atomic force microscopy (AFM)	83
6	Chemical adsorption studies of FI on SiO₂ and Au surfaces	85
6.1	Experimental setup	85
6.2	Results: Analysis of the experimental data	88
6.2.1	^{288,289} FI decay chain correlation search	89
6.2.2	Background conditions	90
6.2.3	Random rate determination	91
6.3	Results: Observed correlated decay chains	92
6.3.1	Observed events in experiment T039 (2014)	93
6.3.2	Observed events in experiment T041 (2015)	94
6.3.3	Distribution of the observed events	96
6.4	Discussion	97
6.4.1	Production and Efficiency	97

6.4.2	Chemical interpretation	98
7	Conclusion and Future studies	107
	Appendices	121
A		123
A.1	HIVAP predictions	123
A.2	Source codes of the Monte Carlo Simulations	126
A.2.1	Monte Carlo code based on the simple adsorption-desorption mechanism	126
A.2.2	Extended Monte Carlo Code including the surface diffusion step	132
A.2.3	Specifications gas purification cartridges	141
	Acknowledgements	147

Chapter 1

Introduction

Uranium (U) with atomic number $Z=92$, is the heaviest element which has been found in large quantities in nature, since it is the last element whose lifetime is comparable to the age of the earth. It is positioned in the actinide series in the periodic table of elements. Elements with a higher Z and mass, can be synthesized artificially in nuclear reactions [1]. Rutherfordium (Rf, $Z=104$) is the first element of the transactinide elements, which are also called SuperHeavy Elements (SHE) [2]. To date, the periodic table of the elements includes elements with Z up to 118. Most recently, the discovery of the elements with $Z=113$, $Z=115$, $Z=117$, and $Z=118$ was confirmed, and these were named nihonium (Nh), moscovium (Mc), tennessine (Ts), and oganesson (Og), respectively [3].

Theoretical and experimental research on SHE has been of great interest in nuclear chemistry and physics for the last decades [2, 4–7]. For physicists, such studies offer unique possibilities for an insight into the nature of nuclear structure at extremes of stability because of their high atomic numbers. For chemists, the placement of new elements in the periodic table raises the question of whether they will follow the trends within their chemical group, or whether the influence of relativistic effects [8–10] causes a deviation from periodicities in the group. Performing experimental research on the SHE is challenging since the number of available atoms is drastically limited to a few atoms per hour or day (or even month), and their lifetimes become very short with increasing Z , from milliseconds to minutes at most [5].

1.1 Stability of SHE

The nucleus consists of protons and neutrons, which are held together by strong short-range nuclear cohesive forces. The Coulomb repulsion between the protons counteracts this stability. With increasing Z the repulsion of the protons increases, but can be compensated by the addition of neutrons up to a certain limit. When the proton repulsion exceeds the strong nuclear force, the nucleus becomes unstable and undergoes radioactive decay.

The stability of SHE ultimately affects the possibility of their identification. Due to their large number of protons, SHE should have a very low nuclear stability against spontaneous fission (SF) and also against α -decay. According to the Liquid-Drop-Model (LDM) [11, 12], SHE should decay immediately by SF and thus can only exist due to nuclear shell stabilisation [13, 14].

1.1.1 Liquid Drop Model

The Liquid Drop Model (LDM) is a macroscopic approach to explain the collective structure of the nucleus [11]. Within this framework, the atomic nucleus is considered to be a drop of incompressible nuclear matter: a quantum liquid with uniform density. The spherical shape of the nucleus remains constant and the surface tension (nuclear strong force) holds the nucleus together, while the Coulomb interaction of the protons counteracts this.

In order to understand the limits of nuclear stability, the determination of the binding energy is crucial. Binding energy is defined as the energy which is required to break up the nucleus into its constituent neutrons and protons. To calculate the binding energy per nucleon, a semiempirical formula was developed by Weizsäcker [11], which was later simplified by Bethe and Bacher [15] to the form known as the Bethe-Weizsäcker formula:

$$BE(A, Z) = a_v A - a_s A^{2/3} - a_c Z \frac{(Z-1)}{A^{1/3}} - a_a \frac{(N-Z)^2}{A} \pm \delta, \quad (1.1)$$

where N , Z and A are the neutron, proton and mass number respectively and the constants a_v , a_s , a_c and a_a are determined empirically. The volume term $a_v A$ determines the binding energy of the nucleons. It is not dependent on Z since the strong nuclear cohesive force acts on all nucleons alike. Instead it scales with the atomic mass. The surface term $a_s A^{2/3}$ corrects the binding energy for the nucleons situated at the surface of the nucleus, which have fewer nearest neighbors to interact with. The Coulomb repulsion between the protons in the nucleus is determined by the Coulomb term $a_c Z(Z-1)/A^{1/3}$. The asymmetry term $a_a (N-Z)^2/A$ is a result of the Pauli exclusion principle. It reflects the increased stability of nuclei with approximately equal numbers of protons and neutrons. The last term δ is the quantum mechanical pairing energy [13, 16]. It takes into account that nuclei with even proton and neutron numbers are more stable (δ positive) than nuclei with odd numbers (δ negative), or than nuclei with even-odd proton and odd neutron numbers (δ zero).

The LDM binding energy per nucleon shows that nearly all nuclei lie within the predicted area, which corresponds to a binding energy per nucleon of 7.5 MeV. For the elements at the upper end of the nuclear chart ($Z > 100$) lower binding energies are predicted.

1.1.2 Nuclear Shell Model

With the help of the LDM, gross features of the nuclear stability of known nuclides can be reproduced. However, there are local deviations between the masses determined by the LDM and those determined experimentally for elements with certain proton and neutron numbers (Fig. 1.1) [17, 18]. An extra stability for nucleon numbers 2, 8, 20, 28, 50, 82, and 126 is observed, these numbers are called magic numbers [19]. Nuclei with magic numbers of protons and neutrons are called doubly-magic nuclei, e.g. ^{208}Pb . Their mass deviation from the LDM is even more pronounced.

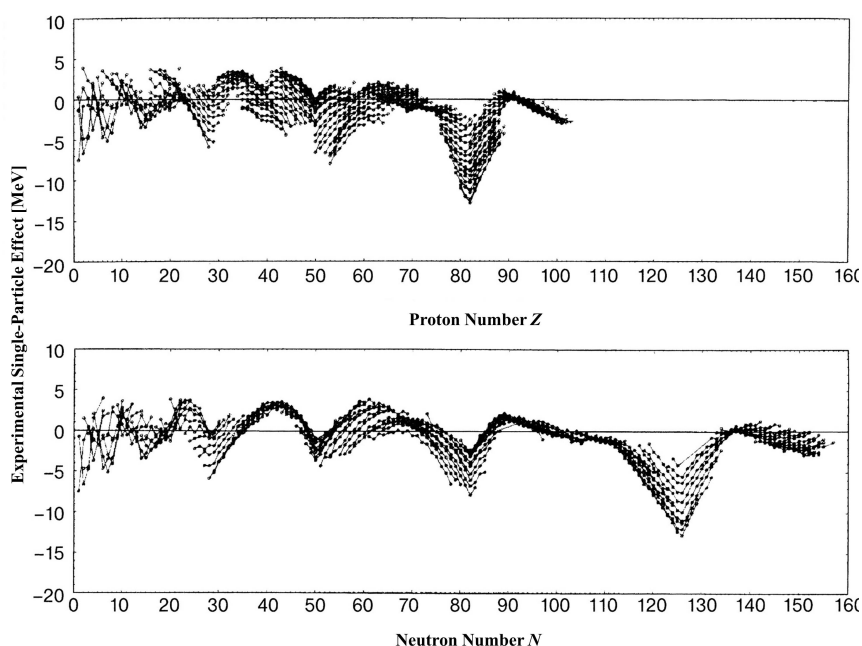


Figure 1.1: Comparison of the ground-state masses in MeV between experimentally observed data, and LDM calculations. Pronounced deviations are observed at nucleon numbers 28, 50, 82 and 126: the so-called magic numbers. The figure is adapted from Ref. [20].

The nuclear stability of nuclei with magic numbers can be explained by the nuclear shell model, which considers each nucleon to be moving in a single-particle orbit within the nucleus. Hereby, the shells for protons and neutrons are independent of each other.

By calculating the energies of "single-particle spectra" using a square and harmonic-oscillator potential it is possible to explain the magic numbers [21, 22]. The energy levels resulting from the calculations with the harmonic-oscillator potential are presented in Fig. 1.2. In order to reproduce the magic numbers correctly, Mayer [13] and Haxel, Jensen and Suess [14] proposed independently that a spin-orbit interaction should be added to the centrally symmetric potential. With increasing angular momentum number (l) the magnitude of splitting increases as well, which results in substantial energy gaps, free of any particle state. Thus, once all of the levels below a major gap are occupied by nucleons, the nucleus contains a filled shell (comparable to the electronic shells known in chemistry) and exhibit enhanced stability. Although a filled shell increases the stability of the nucleus, the nuclei near closed shells exhibit enhanced stability as well, compare Fig. 1.1. Nuclei with closed shells are usually spherical. Nevertheless, the stability cannot be explained by the spherical nuclear shell model for some regions.

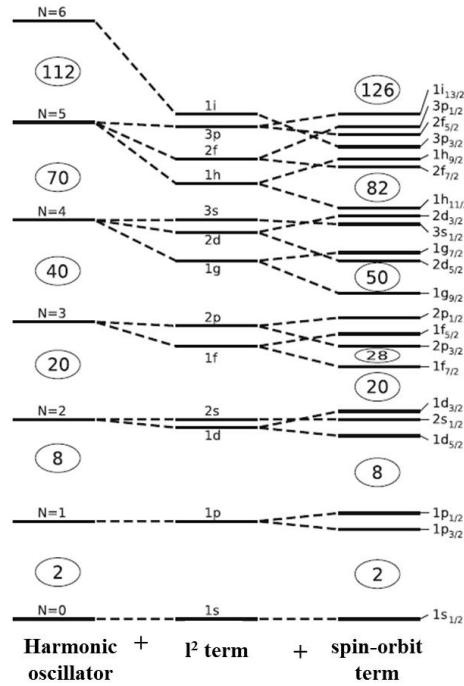


Figure 1.2: Schematic representation of the energy levels in the nuclear shell model, taken and modified from Ref. [2]. The levels on the left are those of the harmonic-oscillator potential. These are split by the l^2 term to produce the second set of levels, and then again by the spin-orbit term to produce the experimentally observed shell gaps in the levels on the right. This diagram is schematic and not to scale.

1.1.3 Corrections to the Nuclear Shell Model

Since the nuclear shell model fails in describing non spherical nuclei, Strutinsky proposed a method that introduced corrections to extend the shell model to deformed systems and calculated the corrected energy levels of those configurations [23, 24]. The shell-correction energies are calculated using the density of single-particle states from the Nilsson model for deformed nuclei [25].

In the model, a modified harmonic-oscillator potential is used to investigate the effect of deformation on the nuclear energy levels. The energy splitting as a function of deformation is shown in Fig. 1.3. In the case of no nuclear deformation, i.e. $\epsilon=0$, the nucleus is spherical and the nuclear shell model is adequate to describe the energy levels. As the deformation increases, the Nilsson states appear and the correction to the shell model become more relevant. At a deformation of about $\epsilon \sim 0.6$, there is a cross-over of the Nilsson states, which results in single-state energy levels. The energy levels of this new region of minimum Nilsson states is lower than those predicted by the spherical shell model.

The corrected energy ($E_{corr.}$) of the nucleus, and also called a macroscopic-microscopic calculations, is the sum of two terms: the energy determined by the liquid drop model (E_{LDM})(macroscopic part), and the shell (δS) and pairing (δP) corrections (microscopic part). The equation is given in 1.2.

$$E_{corr.} = E_{LDM} + \sum_{p,n} (\delta S + \delta P) \quad (1.2)$$

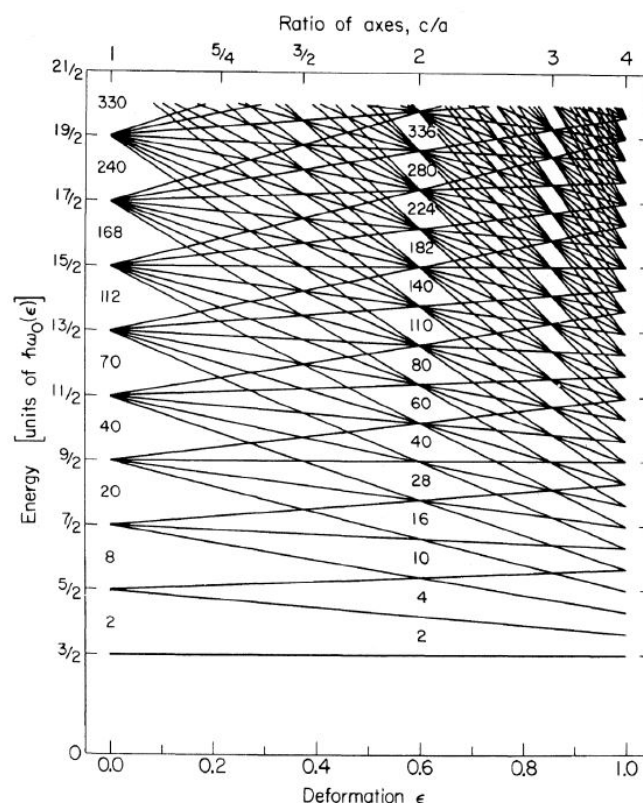


Figure 1.3: Nilsson model, which describes the nuclear energy levels of a modified harmonic-oscillator potential as a function of the deformation of the nucleus. The graph is taken and adapted from Ref. [26,27].

The shell-correction energy tends to lower the ground-state masses of nuclei with magic or near-magic numbers, which means that the discrepancy between the calculated-and experimentally-determined masses (Fig. 1.1) are reduced.

1.1.4 SHE region

SHE cannot be understood without taking into consideration their shell structure effects. Without these effects, the nuclei would immediately decay because of the Coulomb repulsion between the protons. In the middle of the 1960s theoretical calculations with a spherical nuclei configuration concluded that reasonable candidates with a magic number (closed shell configuration) next to the experimentally known $Z=82$ and $N=126$ (^{208}Pb) could be $Z=114$ and $N=184$ (^{298}Fl) [6, 28, 29]. In the 1980s, considerations on the deformation of SHE nuclei were adopted to the theoretical calculations and predicted relatively long half-lives for the deformed nuclei around ^{270}Hs to be observed [6]. Recent calculations on relativistic mean-field theory (RMF) confirm a closed shell configuration for ^{298}Fl , as also predict a higher stability for $Z=106$, $N=166$ instead of $Z=108$ as predicted before [30]. Using the Hartree-Fock method, an increased stability due to nuclear shell effects is predicted at $Z=126$ and $N=162$. In comparison to the other theoretical predictions, no magic number is predicted for ^{298}Fl , but for $Z>114$ and $N=184$ [31]. The nuclei with a closed shell configuration would form an "island" of relative stability with half-lives from seconds up to days [5].

In the simplified LDM, the calculated nuclear masses are closely related to the description of the ability to undergo nuclear fission. The fission for heavy nuclei predicts a rapid fall in the fission barrier height E_{fiss} with increasing fissility parameter $x = Z^2/A$ [5]. In Fig. 1.4, the shape and height of the fission barrier (E_{fiss}) as a function of the deformation parameter (δ) of a spherical nucleus for several fissility parameters (x) is shown. Furthermore, the shape of the nucleus during deformation for symmetric fission into two spherical fragments with $A/2$ and $Z/2$ is illustrated.

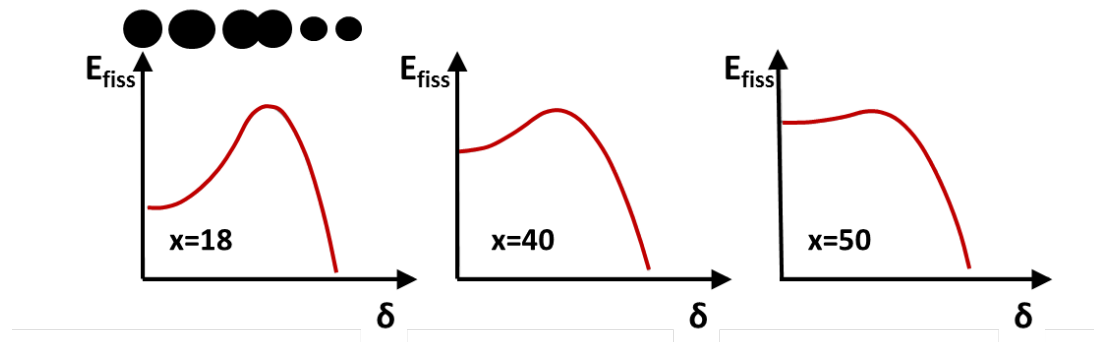


Figure 1.4: Schematic illustration of the fission barrier in function of the deformation parameter of a spherical nucleus (δ) for several fissility parameters (x), according to the LDM. The shape of the nucleus during deformation is also illustrated. More detailed information can be taken from the text. Figure is taken from Ref. [5].

At a fissility parameter of 18, the energy needed to overcome the fission barrier for spontaneous fission of the nucleus is very high. A strong deformation to the nucleus has to be applied to force a spontaneous fission. According to this model, the limit of stability against SF is around $x \approx 40$, corresponding to ^{256}Rf ($Z=104$): the first element of the transactinide series. With a fissility parameter of ~ 50 , the fission barrier almost completely vanishes. This means that according to the LDM for fission, a small deformation of the nucleus causes SF to occur, resulting in the statement that SHE should not be stable against SF and decay very quickly with half-lives shorter than 10^{-14} s [5]. However, experiments have shown that a large number of nuclei beyond the fissility limit of 40 exist and decay predominantly through α or SF-decay with measured half-lives of up to several seconds. The nuclear shell model showed that closed shells of protons and neutrons stabilize nuclei beyond the limits defined by the LDM. Hence, SHE exist solely because of enhanced nuclear stability due to shell effects [5].

The nuclear shell effects do not only have an influence on the half-lives of the nuclei, but also on the height of the fission barrier B_f [6]. The fission barrier height is an important quantity which determines if the CN suffers neutron evaporation or fission. For a spherical compound nucleus, B_f decreases as the nuclear deformation increases. On the contrary, in a deformed CN the B_f increases with increasing nuclear deformation, meaning that the system needs to overcome a bigger energy barrier to undergo fission.

1.2 Production of SHE in nuclear fusion reactions

SHE have not been found in nature so far. However they can be synthesized artificially in nuclear fusion reactions at suitable particle accelerators. Due to the increasing Coulomb repulsion with increasing Z , a

limited number of elements which can be synthesized is expected. Theoretical investigations predict the formation of bubbles or semi-bubbles in the hyperheavy region of $Z \geq 150$, to compensate the coulomb repulsion [32]. The bubble nuclei form a spherical shell, so that the central density is equal to zero [32]. Based on this, the production limit of superheavy/hyperheavy elements is predicted by some theorists to be in the range of $Z \approx 300$.

For the production of SHE, a target is irradiated with a high-intensity heavy-ion beam. If the beam energy is large enough to overcome the Coulomb barrier between the target and the projectile nuclei, they may undergo capture, and the fraction will evolve into a compound nucleus (CN) in an excited state. The CN can decay by overcoming two distinct saddle-points by fission or neutron emission [33]. The relative decay probability of neutron emission or fission is the ratio N_n/N_f , where N_n and N_f are the number of levels in the energy intervals between the total available energy and the energy of the neutron emission or fission saddle points. Therefore, the decay probability is independent of the energy of the CN [33]. A scheme of the nuclear fusion process leading to the creation of SHE is shown in Fig. 1.5.

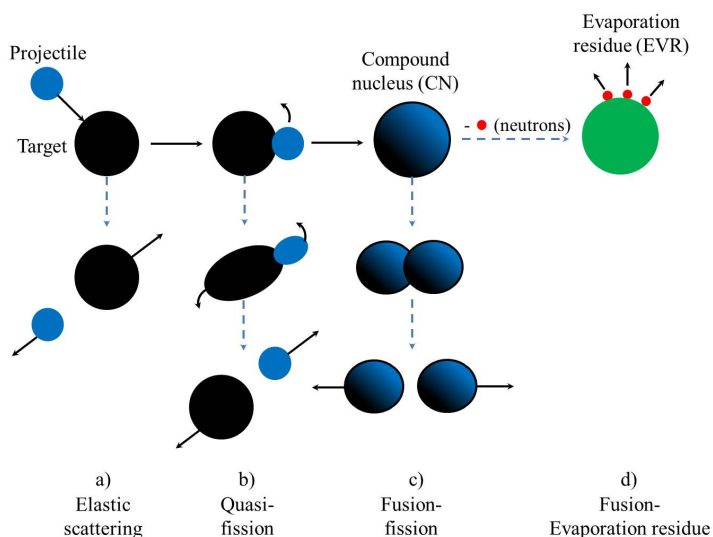


Figure 1.5: Schematic illustration of the fusion reaction towards creation of SHE. The letters under the figure describe the different stages: a) shows the collision of projectile and target nuclei with possible elastic scattering. b) shows inelastic scattering and quasi-fission, c) shows the CN nucleus in a highly excited state which can either undergo prompt fission, or de-excites rapidly by emission of neutrons and γ -rays, to the survival CN (d)).

When a beam projectile hits the target nucleus, three interaction possibilities are in competition:

- Elastic scattering, which does not result in the fusion of target and projectile nuclei (Fig. 1.5 a).
- Deep inelastic scattering or quasi-fission. When the target and projectile nuclei collide in a non central position, the nuclei touch each other and transfer some neutrons, but can be re-separated by centrifugal forces (Fig. 1.5 b).
- When the target and projectile nuclei hit at very small impact parameters, they can undergo fusion and form a CN in a highly excited state. As the fission barrier is lower than the excitation energy, the newly-created excited CN undergoes fission within 10^{-14} s unless the excitation energy is reduced by

evaporation of one or more neutrons and γ emission (Fig. 1.5 c). A so-called Evaporation Residue (EVR) of interest in its ground state is formed in only a few cases.

In conclusion, the fusion of SHE is very challenging due to the high probability of re-separation in the entrance channel and a high probability for SF in the exit channel. The survival probability (P_{surv}) that the CN evaporates a neutron, is the product of the probability to emit one neutron, rather than fission in the first deexcitation stage process, times the probability $P_{<}$ that its remaining excitation energy is lower than the energy threshold for fission or a second neutron evaporation. The probability is given as,

$$P_{surv} = \frac{\Gamma_n}{\Gamma_t} \cdot P_{<} \quad (1.3)$$

where Γ_n is the probability of neutron evaporation, Γ_f the probability for fission of the compound nucleus and $\Gamma_t = \Gamma_n + \Gamma_f$ [33]. The production cross-section (σ_{prod}) of the EVR is composed out of the capture cross-section (σ_{cap}) of a projectile by the target, the probability for the formation of the CN (P_{CN}) and the survival probability of the CN (P_{surv}) [33]. It is expressed by the following equation:

$$\sigma_{prod} = \sigma_{cap} \cdot P_{CN} \cdot P_{surv}. \quad (1.4)$$

Nuclear fusion reactions leading to SHE can be divided into two groups [2, 7, 34, 35]:

- "hot" fusion reactions, in which the excitation energy (E^*) of the CN is ~ 30 -50 MeV (corresponding to an evaporation of 3 to 5 neutrons).
- "cold" fusion reactions, in which the E^* of the CN is ~ 10 -20 MeV, resulting in the evaporation of 1 to 2 neutrons.

Hot fusion reactions are asymmetric reactions, in which light projectiles (e.g. oxygen (O), neon (Ne), magnesium (Mg), or chlorine (Cl)) in combination with actinide targets are used. These result in larger production cross-sections but reduced survival probabilities due to the higher E^* of the CN. The elements nobelium (No, $Z=102$) up to seaborgium (Sg, $Z=106$) were discovered with this reaction type. Cold fusion reactions are more symmetric reactions, in which massive projectiles like iron (Fe), zinc (Zn), or nickel (Ni) and targets as bismuth (Bi) or lead (Pb) are used. These reactions lead to low E^* , resulting in a higher survival probability for the CN, but the production probability is reduced due to small values of P_{CN} . In general, cold fusion reactions are not very common and lead to more neutron-deficient isotopes than hot fusion reactions. The elements bohrium (Bh, $Z=107$) up to nihonium (Nh, $Z=113$) were synthesized for the first time using cold fusion reactions [5]. Experiments revealed, as shown in Fig. 1.6, that the cross-sections for the production of EVRs decreases sharply with increasing Z . The potential of cold fusion reactions is exhausted for SHE in the region of $Z \geq 114$. At the same time warm fusion reactions become more favorable. The warm fusion reaction is a combination of hot and cold reactions in which a double-magic projectile (^{48}Ca) hits an actinide target (e.g. ^{244}Pu , ^{243}Am). In this way, a relatively large production cross section for $Z \geq 112$ is obtained (Fig. 1.6), with the advantage that E^* is lower than in

hot fusion reactions. With the warm fusion reaction, the elements flerovium ($Z=114$) up to oganesson ($Z=118$) have been produced and discovered [3].

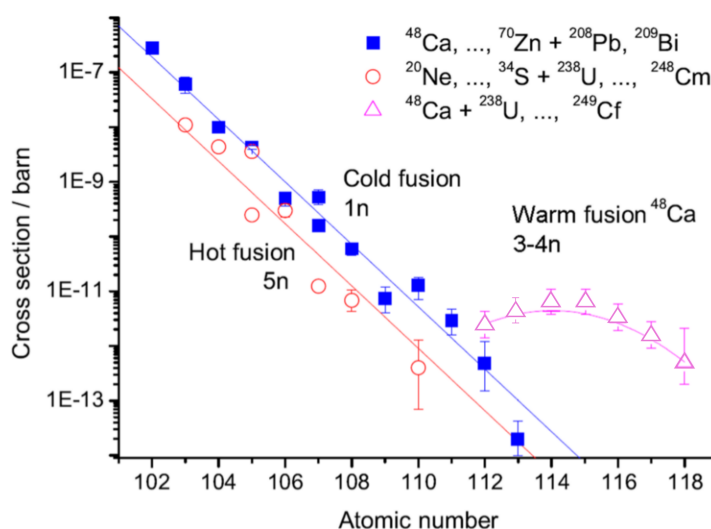


Figure 1.6: Experimental cross-sections for the formation of nuclei with $Z \geq 102$ in (■) the 1n evaporation channel of cold fusion reactions, (○) the 5n of hot fusion reactions, and (△) fusion reactions of the type $^{48}\text{Ca} + \text{actinide targets}$. Figure taken from Ref. [4] and adapted with values taken from Ref. [7].

1.3 Chemical properties of SHE

The position of an element in the periodic table is defined by its electronic configuration and therefore by its atomic number. When a new element is placed in a chemical group, the interesting question is whether its properties follow the chemical trends within its group. Deviations can occur due to the influence of relativistic effects on the valence shells of the elements [8–10]. Since these effects scale with Z^2 , the influence of the relativistic effects should be most pronounced in the SHE region. A general introduction into the relativistic effects and their influence on heavy elements will be given in the next section. More detailed explanations can be found in Ref. [8].

1.3.1 Relativistic effects

With increasing atomic number of the heavy elements, the Coulomb force attracting the electrons to the nucleus grows. Electrons near the nucleus are accelerated to relativistic velocities, and their mass (m) increases as

$$m = \frac{m_0}{\sqrt{1 - \left(\frac{v}{c}\right)^2}}, \quad (1.5)$$

where m_0 is the rest mass, v is the velocity of the electron and c is the speed of light. The orbital radius (r) of the electron can be determined by the Bohr model for hydrogen-like species:

$$r = \frac{Ze^2}{mv^2}, \quad (1.6)$$

in which the mass, velocity (v), atomic number, and charge of the electron (e) are important. With increasing electron mass, the orbital radius decreases, leading to a contraction and energetic stabilization of the orbitals. This effect is called the direct-relativistic effect and acts on s - and $p_{1/2}$ -orbitals, which are spherical. The energetic stabilization (E) of the orbital can be calculated via equation 1.7. It includes the principal quantum number (n) and also Planck's constant (h):

$$E = -\frac{2\pi^2 e^4}{n^2 h^2} m Z^2. \quad (1.7)$$

The second, so-called indirect-relativistic effect is a consequence of the direct-relativistic effect. The relativistic contraction of the s and $p_{1/2}$ orbitals leads to a strong shielding of the nuclear charge for electrons in orbitals with a node at the location of the nucleus. This results in a destabilization and expansion of the $p_{3/2}$, d and f orbitals. These non-radially symmetric orbitals, which have no electron density at the core, are energetically destabilized by this shielding and expand.

The third relativistic effect is the spin-orbit (SO) splitting of levels with quantum number $l > 0$ (p, d, f, \dots orbitals) into sublevels with the total angular momentum quantum number $j = l \pm \frac{1}{2}$. The magnitude of the SO splitting increases with decreasing numbers of sub shells, i.e. the $np_{1/2} - np_{3/2}$ splitting is larger than the $nd_{3/2} - nd_{5/2}$ splitting, and both are larger than the $nf_{5/2} - nf_{7/2}$ splitting. The magnitude of the spin-orbit splitting in transactinide nuclei can be comparable to the strength of chemical bonds [2, 36].

The increasing velocities of electrons to relativistic speeds make simple theoretical studies in which the chemical properties of SHE are extrapolated from those of the lighter elements unreliable. Relativistic quantum theories and quantum-chemical methods have been developed to accurately treat relativistic effects for heavy elements. Alongside experimental investigations, theoretical studies on the chemical properties of the SHE are important to predict and help to interpret experimental outcomes. Only a comparison of the observed behavior of the elements with those predicted on the basis of relativistic versus non-relativistic calculations allows the importance and magnitude of the relativistic effects to be assessed.

1.4 Chemical investigation techniques

The production of SHE is extremely challenging, as are the chemical procedures required for their study. Chemical information can currently only be accessed for elements with half-lives of the order of seconds or longer. Due to the low production rates of SHE (section 1.2), experiments can only be performed at a single atom-at-a-time level. Since the half-lives of the produced atoms are very short, unique experimental methods were developed and have to be improved constantly. The chemical studies on SHE can be divided into four basic steps:

- Synthesis of SHE,

- rapid transport of the EVRs to the chemical apparatus,
- selective and efficient chemical separation procedures,
- detection of the EVRs via their characteristic nuclear decay properties.

The production rate of the EVRs is proportional to the target thickness, within limits, and the beam intensity. The target thickness must be large enough to produce EVRs at a measurable rate, but sufficiently thin for recoils to escape [37]. Thicknesses are limited to about $<0.8 \text{ mg/cm}^2$, for experiments behind a kinematic recoil separator with ^{48}Ca -induced reactions [5]. Furthermore, the target is required to be mechanically stable to maintain integrity through handling and irradiation, and must be chemically stable in the highly-ionizing environment created by the beam. The limiting factor for the beam is mainly the target backing and the target itself. On the one hand the beam intensity should be as high as possible, but on the other hand destruction of the target must be avoided.

The interaction of the beam particles with the target material can lead to the formation of desired EVRs. However, several other nuclear reactions like transfer reactions take place simultaneously, which produce a large amount of unwanted byproducts. These lead to an increased background in the detectors which can hamper the identification of decay chains originating from SHE. The second major problem that can complicate or hamper the detection of SHE is the accelerated heavy ions of the beam. Only a small amount of the accelerated ions react with the target material and a large fraction passes through the target. A detector installed directly behind the target would be destroyed in short time due to the high energy and flux of the ions. Additionally, some chemistry experiments would not be possible due to the severe influence on chemical reactions by the production of a plasma by the ion beam [38]. In order to prevent these complications, pre-separation with a kinematic recoil separator can be used. Two types of recoil separators have been developed: the gas-filled separator and the vacuum separators, e.g, Wien-filter or energy separator. Gas-filled separators use the different magnetic rigidities of the different reaction products and projectiles traveling through a gas-filled volume in a magnetic dipole field to separate them. In a Wien-filter, the EVRs are separated from unwanted byproducts through differences in their E/q . Examples of gas-filled separators are the TransActinide Separator and Chemistry Apparatus (TASCA) at GSI in Darmstadt, Gas-Filled Recoil Ion Separator (GARIS) at RIKEN in Tokio, or Dubna Gas-Filled Recoil Separator (DGRFS) at FLNR in Dubna [5]. Examples of Wien-filter separators are the Separator for Heavy Ion reaction Products (SHIP) at GSI in Darmstadt, and Separator for Heavy Element Spectroscopy (SHELS) at FLNR in Dubna [5]. For this work, the gas-filled separator TASCA was used. More details on the working principle will be given in chapter 2.

The choice of chemical separation system is based on a number of requirements, which all have to be fulfilled simultaneously to reach the required sensitivity:

- **Speed:** Since the half-lives of the SHE are very short, the time between their production and detection has to be kept as short as possible. The transport time is one of the main factors determining the overall yield.
- **Selectivity:** As already mentioned in the section above, unwanted byproducts from transfer reactions or primary beam passing through the target can cause a large background in the detection systems

and hamper the identification of decay chains originating from SHE. Kinematic pre-separation is well suited to efficiently suppress the background if the chemical selectivity is insufficient.

- **Single atom sensitivity:** Since the production rates for SHE nuclei are very low, they have to be chemically processed on an "atom-at-a-time" scale. This means that the chemical separation must be repeated at a high rate or be continuous. Many experiments have to be performed to ensure statistical significance. For this to be fulfilled, fully-automated, continuously-operating chromatography systems were developed (section 1.4.1).
- **Detection:** The unambiguous detection of the separated atoms is the most essential part of the whole experiment. To this date, the detection of characteristic nuclear decay signatures of transactinide nuclei remains the only possibility to unambiguously detect the presence of single atoms of SHE after chemical separation. Thus, final samples must be suitable for high resolution α -particle and SF spectroscopy and ideally allow the coincident detection of both SF fragments. Most transactinide nuclei have characteristic decay chains that involve the emission of α -particles or the SF of daughter nuclei. The detection of such correlated decay chains requires event-by-event recording of the data.
- **Speciation:** Since the SHE are detected via their nuclear decay, the speciation cannot be determined directly. This is why the chemical behavior of the lighter homologs must be studied in an identical experimental setup as that used for the SHE chemistry experiments. The chemical system must be chosen in such a manner that a certain chemical state is probable and stabilized by the chemical environment.

Four different approaches, which involve the direct detection of the nuclear decay of the separated atoms in combination with chromatography systems, have been successful in studying the chemical properties of transactinide elements. Two of the systems work in combination with liquid-phase chromatography, whereas the other two are designed to investigate volatile transactinide compounds in combination with gas-phase chromatography. A short overview on the gas-phase chromatography methods will be given in the next section.

1.4.1 Chromatographic methods and adsorption

For many years, gas-and liquid-phase chromatography methods have been established to study the chemical properties of SHE. In 1966 the first gas chromatography experiments were performed to investigate the volatility of rutherfordium compounds [39]. In 1970, the first liquid-phase chromatography experiments were also performed on Rf compounds [40].

The liquid-phase chromatography methods [41–45] were not suited to investigate the chemical properties of SHE above $Z=105$, due to long separation times and decreasing half-lives of the elements. Only low overall chemical yields were achieved. Until today, gas-phase chromatography methods are favored for SHE with higher atomic numbers because they are fast and efficient and can be performed continuously. Furthermore, the chromatography technique can be directly combined with detection of the decay chains originating from the SHE. Examples for this are the chromatography and detection systems COLD (Cryo On-Line Detector) [46] and COMPACT (Cryo On-Line Multidetector for Physics And Chemistry of

Transactinides) [47]. A short overview and principle of the gas chromatography methods will be given here, while a detailed explanation can be found in Refs. [5, 48]. For the experiments presented in this work, COMPACT detector arrays were used. A more detailed explanation on COMPACT will be given in section 2.4.

Gas-phase experiments are based on the principle of gas-solid chromatography. The separation of volatile species occurs due to the repeated interaction of the atoms carried through a chromatographic column by a carrier gas (mobile phase) and a stationary phase (column surface). The stationary phase usually consist of silicon photodiodes, which are covered with metallic surfaces like Au (gold), or non-metallic surfaces like SiO₂ (quartz). Two techniques have been used to obtain thermochemical data of transactinide compounds in gas-phase experiments. These are called thermochromatography (TC) and isothermal chromatography (IC) [49] and are schematically shown in Fig. 1.7.

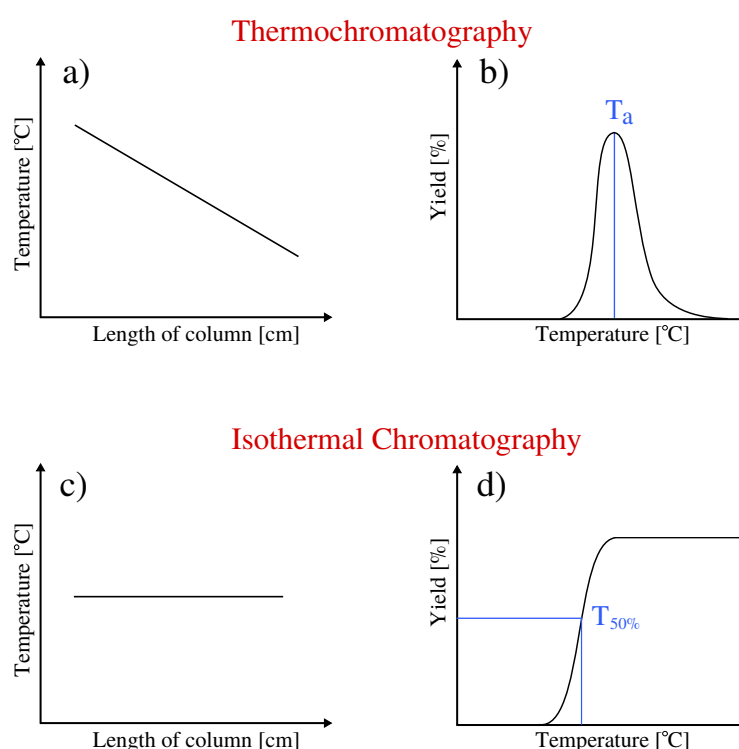


Figure 1.7: Working principle of thermochromatography (TC) (a and b) and isothermal chromatography (IC) (c and d). More explanations are given in the text.

In both techniques, the volatile species are transported through the chromatography column with a carrier gas. In TC, a negative temperature gradient is applied along the column length (Fig. 1.7a)). Due to the decreasing temperature in the column, the time the species spend in the adsorbed state on the column surface increases exponentially. Different species having different adsorption interactions with the Au or SiO₂ surfaces form separated deposition peaks at characteristic temperatures (T_a) (Fig. 1.7b)).

In IC (Fig. 1.7c)), the temperature along the column is kept at an isothermal constant value. Depending on the temperature of the column and the adsorption interaction of the species with the column surface, they travel slower through the length of the column than the carrier gas. The retention time can be determined either by injecting a short pulse of the volatile species into the carrier gas and measuring the time at which it emerges from the exit of the column, or by continuously introducing a short-lived nuclide into

the column and detecting the fraction that survived passing the column. At a high isothermal temperature, the retention time is very short and almost 100% of the species reach the exit of the column (Fig. 1.7d). When the temperature is lowered, the retention time increases. At the temperature $T_{50\%}$, where the yield is 50% of the maximum yield, the retention time equals the nuclear half-life of the radionuclide contained in the species. It can be shown that for similar gas flow rates and column dimensions, $T_a \approx T_{50\%}$. Online isothermal chromatography is an ideal method to rapidly and continuously separate short-lived volatile radionuclides from less volatile species [4].

Two main types of adsorption on the surface can exist:

- **Physisorption:** Physisorption describes adsorption only due to van der Waals interactions between adsorbate and adsorbent. The interaction is an electrostatic attraction of a permanent or induced dipole moment of two species. Generally it is characterized by relatively low adsorption enthalpies ($-\Delta H_{ads} < 50$ kJ/mol) [49].
- **Chemisorption:** In the chemisorption process, a chemical bond is formed between the surface and the adsorbate. The adsorption enthalpy ($-\Delta H_{ads}$) is > 50 kJ/mol. In chemical bond formation, an activation energy has to be overcome. The adsorption kinetics is dependent on the temperature. The lower the temperature of the surface, the more time is needed to form a chemical bond of the species with the surface. Between extreme cases of physisorption or chemisorption there is possibility that both can occur simultaneously.

1.4.2 Monte Carlo Simulation

From the adsorption temperatures measured in the TC and IC experiments, the adsorption enthalpy ($-\Delta H_{ads}$) of the volatile species on the column material can be evaluated. A Monte Carlo Simulation (MCS) procedure based on a simple microscopic model of an adsorption process [50] has shown that a reversible adsorption process without superimposed chemical reaction (i.e., the transported species remain unchanged during adsorption and desorption) takes place within the column. The simulation was adapted for rectangular detector channels [51], which is applicable to the COMPACT detector arrays.

In the simulation, the path of the atom or molecule through the detector column is simulated. A detailed explanation of the method is described in Ref. [50], and schematically shown in Fig. 1.8.

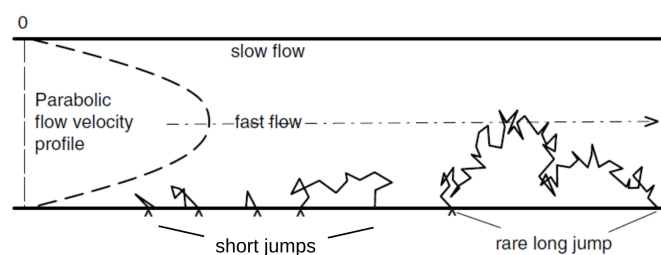


Figure 1.8: Microscopic model of the adsorption process of a molecule in a column. Taken from Ref. [50].

Starting the simulation a random lifetime is determined based on the half-life of the isotopes. The atom spends its lifetime alternating between being adsorbed on the surface, or in the carrier gas being transported

along the column. After every adsorption and desorption step, the lifetime is compared to the total time of all the adsorption and flight steps. If this sum exceeded the lifetime of the atom, the position at which it decayed is recorded and the next atom is simulated. By repeating such simulations for one single atom 10^7 times, the distribution pattern of nuclei decaying in the column is obtained for a given $-\Delta H_{ads}$.

The mean time (τ) an atom spends on a surface is expressed in the Frenkel equation 1.8.

$$\tau = \tau_0 \cdot \exp\left(-\frac{\Delta H_{ads}}{R \cdot T}\right) \quad (1.8)$$

Hereby R is the universal gas constant and τ_0 is the period of vibration perpendicular to the surface in the adsorbed state. In our case, τ_0 is equal to the reciprocal of Debye's phonon frequency of the column surface [52]. The other two factors which influence the adsorption time are the local temperature (T) of the surface, and the adsorption enthalpy ($-\Delta H_{ads}$).

When the atom desorbs from the surface back into the carrier gas its flight through the column is described by several jumps in the range of the order of centimeters (see Fig. 1.8). Due to collisions with the carrier gas, these jumps are oriented in random directions.

Assuming that the carrier gas in the column has a laminar flow, then the gas velocity at the wall of the column is low. This results in a reduced collision rate of the atoms with carrier gas, which means that the atom quickly adsorbs back onto the surface. Most of the jump lengths near the wall of the column are very short. Only in very few cases the atom is transported in the center of the laminar flow and has a long jump length.

In order to determine the mean flight distance of an atom through the detector channel, Golay proposed an equation which was adapted later by Poppe [5, 53, 54]. In this equation the theoretical plate height (H) is determined:

$$H = \frac{\sigma_z^2}{z} = \frac{2D_{1,2}}{v} + \frac{(f_0 + f_1 k + f_2 k^2) \cdot v \cdot y^2}{105 \cdot (k + 1)^2 \cdot 2D_{1,2}}, \quad (1.9)$$

where z is the migration distance in the flow direction, σ_z^2 the ratio of the width of the chromatography peak, and $D_{1,2}$ is the diffusion coefficient. The velocity of the carrier gas (v), the column height (y) and the ratio of the total time in adsorbed state in dependence of the lifetime of the nuclei (k) also appears in the equation 1.9. The values for the coefficients f_0 , f_1 , and f_2 are dependent on the width to height ratios of the chromatography column.

The diffusion coefficient ($D_{1,2}$) is calculated by the semi-empirical Gilliland's equation [55]:

$$D_{1,2} = \frac{0.0044 \cdot T^{3/2}}{p[(M_1/\rho_1)^{1/3} + (M_2/\rho_2)^{1/3}]^2} \cdot \left(\frac{1}{M_1} + \frac{1}{M_2}\right)^{1/2}, \quad (1.10)$$

where T is the temperature, p is the gas pressure, ρ_1 is the density of the diffusing gas, ρ_2 is the density of the diffusion medium and M_1 , M_2 are the molecular weights of the diffusing gas and medium, respectively. The diffusion coefficient for heavy molecules in common carrier gases at a pressure of around one atmosphere

is 0.01-0.1 cm²/s [48].

The total time an atom spends at the wall in one certain part of the chromatography channel depends on τ and the frequency of collisions with the wall. According to the molecular gas theory the number of collisions with the wall Z_z over a distance z in the gas flow direction is

$$Z_z = \frac{u_m \cdot z a_z}{4 \cdot Q} \quad (1.11)$$

Z_z is a function of the ratio of column surface $z a_z$ to volume flow Q and the mean speed of the molecule u_m , given by

$$u_m = \sqrt{\frac{8k_B T}{\pi m_{1,2}}}, \quad (1.12)$$

where T is the temperature, k_B is the Boltzmann-constant and $m_{1,2}$ is the reduced mass.

These equations form the basis for the Monte Carlo Simulation. It takes into account not only the geometry of the detector column, but also information on the carrier gas, e.g. density, mass, pressure and flow rates and the temperature along the detector column. Furthermore, the period of oscillation on the column surface, the half-life of the isotope, the molecular masses of the molecule, and the $-\Delta H_{ads}$ are inputs to the simulation. In this way, it is possible to simulate the distribution patterns of the isotope under experimental conditions. This method was successfully used for the analysis of several experimental data given in Refs. [47, 56–58] and will be used for the analysis of the experimental data discussed in this thesis, see chapters 4 and 6.

1.5 Investigation of flerovium (Fl, Z=114)

1.5.1 Production and decay

The heaviest chemically investigated element to date is Fl. It is positioned in group 14 of the periodic table, and its lighter homolog is lead (Pb, Z=82). Currently, six Fl isotopes, ^{284–289}Fl, have been successfully synthesized in ⁴⁸Ca+^{239,240,242,244}Pu reactions [59, 60]. Their decay chains, together with decay modes, half-lives and α -lines are given in Fig. 1.9. Due to very short half-lives of ^{284–286}Fl (<0.15 s), they are not suitable for chemical investigations. On the contrary, the isotopes ²⁸⁷Fl ($T_{1/2}=0.48^{+0.14}_{-0.09}$ s), ²⁸⁸Fl ($T_{1/2}=0.66^{+0.14}_{-0.10}$ s), and ²⁸⁹Fl ($T_{1/2}=1.9^{+0.7}_{-0.4}$ s) are used to investigate the chemical properties of Fl [59]. They can be synthesized in the fusion reactions ²⁴²Pu(⁴⁸Ca, 3n)²⁸⁷Fl, and ²⁴⁴Pu(⁴⁸Ca, 3-4n)^{288,289}Fl [59]. The chemical investigations discussed in this thesis were performed with the two most long-lived Fl isotopes ^{288,289}Fl.

The production cross-sections for different evaporation channels in the reaction ⁴⁸Ca+²⁴⁴Pu have been determined experimentally. Fig. 1.10 shows the experimentally determined excitation functions for the 3n (red squares), 4n (blue circles), and 5n (cyan triangle down) evaporation channels. The solid-symbolized

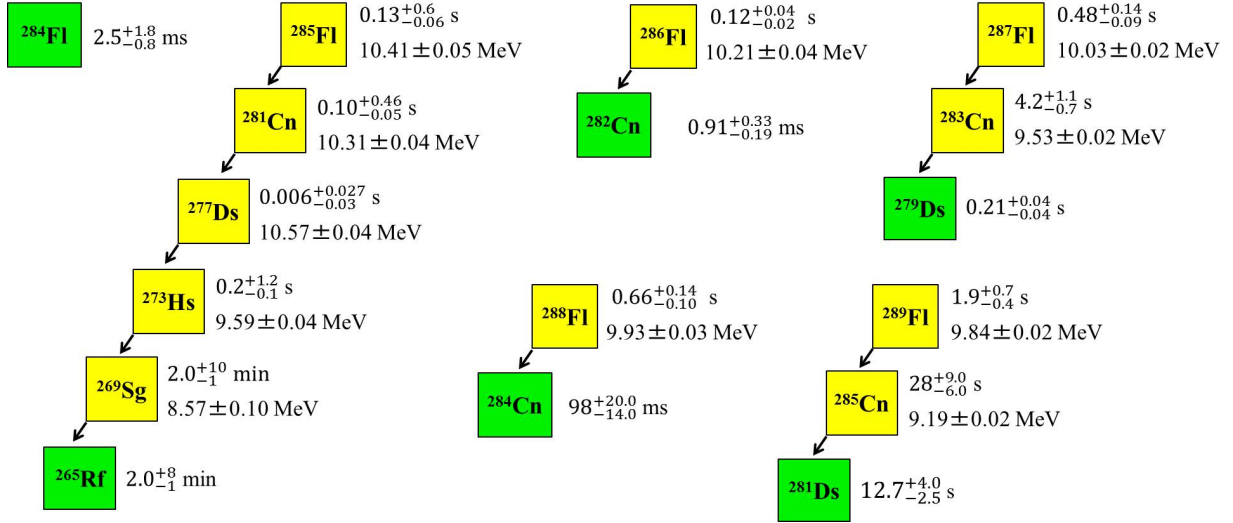


Figure 1.9: Decay chains of $^{284}\text{--}^{289}\text{Fl}$, together with their half-lives, and α -decay line energies [59, 60]. The decay mode is illustrated by the color of the boxes, where yellow and green boxes correspond to α -decay and SF, respectively.

data points were measured at the DGFERS [59, 61, 62], whereas the data points shown as open symbols were measured at the Berkely Gas filled Separator (BGS) [63, 64] and at TASCA [65, 66].

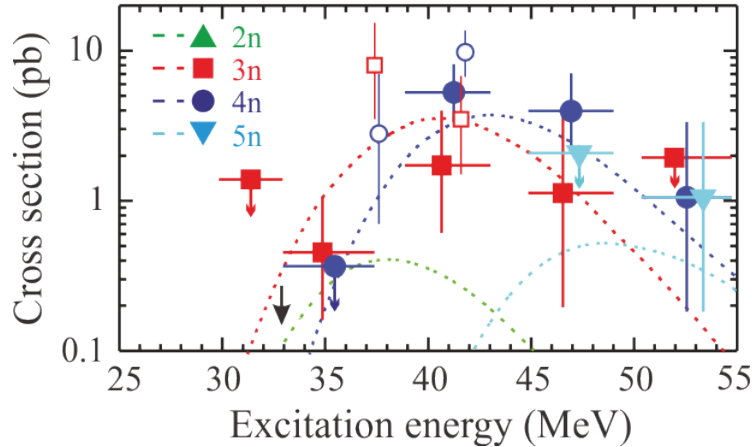


Figure 1.10: Comparison of the excitation functions determined experimentally and with theoretical calculations for the fusion reaction $^{48}\text{Ca} + ^{244}\text{Pu}$. The experimentally determined production cross-sections for complete fusion reactions measured at the FLNR institute (Dubna) are illustrated with solid symbols [59, 61, 62]. The measured cross-sections at the LBNL institute in Berkely [63, 64] and at GSI Darmstadt [65, 66] are illustrated with open symbols. The dashed lines show the results of theoretical calculations. Vertical error bars correspond to statistical uncertainties. Horizontal error bars represent the range of excitation energies populated at given beam energies. The figure is adapted from Ref. [59].

Depending on the excitation energy of the CN, the production cross-sections vary. An excitation energy of around 36 to 39 MeV for the 3n channel results in the highest possible production cross-section for ^{289}Fl of $8.0^{+7.4}_{-4.5}$ pb. For ^{288}Fl , the highest production cross-section is observed at an excitation energy in the range of 39 to 44 MeV with $9.8^{+3.9}_{-3.1}$ pb [66].

The dashed lines in Fig. 1.10 show the results of theoretical calculations [35, 67]. For elements in the middle-mass region, the cross-sections can be predicted with the help of a statistical model code called

HIVAP [68], which was developed at GSI Darmstadt. It is very challenging to perform this statistical method in the SHE region due to the complexity of the competing reaction mechanisms, e.g., fusion and quasi-fission. Many estimations have to be made, that reduce the accuracy of the model [67]. However, special theoretical calculations (described in Ref. [67]) have been performed, from which the estimated production cross-sections for $^{288,289}\text{Fl}$ are in good agreement with the experimentally determined values (compare Fig. 1.10).

1.5.2 Theoretical predictions of the adsorption behavior

On the basis of relativistic calculations, theoretical predictions on the chemical properties of SHE can be made. They allow the assessment of the importance and magnitude of relativistic effects and help to interpret the experimental outcomes. To date, the most common molecular calculation framework is the relativistic Density Functional Theory (DFT) [69, 70]. With this calculation method, systems with a large number of atoms like molecules, clusters or supercells can be treated with sufficient accuracy.

For SHE, DFT calculations of adsorption energies of the SHE and their homologs on Au and SiO_2 surfaces at different adsorption positions have been performed. Homogeneous supercells of hydroxylated(001) α -quartz surfaces and homogeneous Au(111) clusters were used [71–74]. Fig. 1.11 shows a schematic example of the different adsorption positions of an adatom on an Au(111) cluster [75]. In the top position, the adatom adsorbs on top of one of the surface atoms in the cluster. Bridge position means that the adatom adsorbs in between two surface atoms. In the hollow1 position, the adatom adsorbs on top of an atom in the second layer (calculated from the top) of the cluster, whereas hollow2 is the adsorption of an atom on the third layer of the cluster. A different energy is determined for every adsorption position. For every adatom, the weakest adsorption energy was found for the top or bridge position. The hollow positions are the energetically most favorable and show the highest adsorption energies [71–74]. Most recently, theoretical calculations on the adsorption energies of the SHE and their homologs have been performed for inhomogeneous Au surfaces, in which vacancies and grain boundaries exist in the Au cluster. The adsorption energies on vacancies were found to be even higher than for the hollow positions [76].

In Fig. 1.12, the predicted adsorption energies (E_{ads}) in kJ/mol for Cn, Nh, and Fl, and their homologs mercury (Hg, Z=80), thallium (Tl, Z=81), and lead (Pb, Z=82) on Au(111) (curves a, b) and hydroxylated α -quartz (001) (curve c) surfaces are illustrated. For the Au surface, calculations were performed for an adsorption of an adatom in hollow2 position (curve b), and for the adsorption in a vacancy (curve a). Both curves reflect the stronger binding of all atoms in a vacancy to the hollow2 position.

Copernicium, the α -decay daughter of Fl, is positioned in group 12 of the periodic table. Its lighter homolog within the group is Hg. All group members have a closed shell ground-state configuration $(n)s^2(n+1)d^{10}$ (e.g. for Cn $6d^{10}7s^2$). Due to the increasing relativistic effects with increasing Z, there is a relativistic stabilization and contraction of the 7s atomic orbital (AO). This means that the s-electrons are less accessible for chemical binding, causing Hg (for example) to be unique as a metal with respect to its liquid standard state. Furthermore, it is the only element apart from the noble gases whose vapor is almost entirely monatomic [5]. In the case of Cn, the relativistic effects are further amplified so that originally it was assumed that Cn is very volatile and rather inert like a noble gas. In addition to its chemical reactivity, the possibility was discussed that Cn might be a gas or a very volatile liquid under ambient conditions [77].

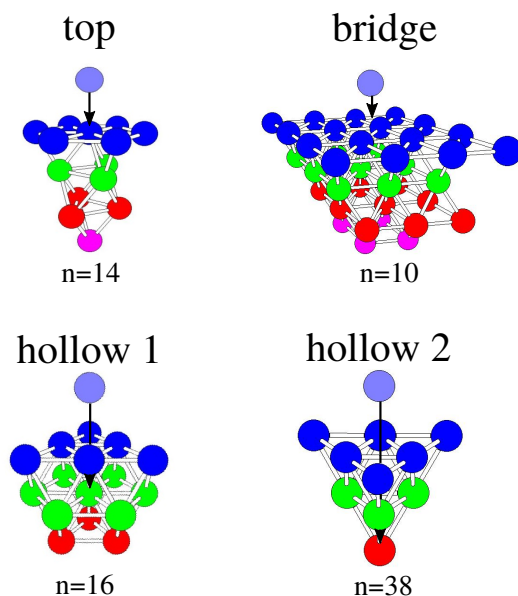


Figure 1.11: Schematic example of different adsorption positions of an adatom onto an Au(111) cluster [75]. The cluster size is given by n . Explanations can be found in the text. Figure is taken from Ref. [75].

As shown by curves a and b in Fig. 1.12, more recent theoretical calculations predict Cn to be indeed more volatile than its lighter homolog Hg, but still it should retain a metallic character allowing bond formation with metallic surfaces like Au [71,76]. On inert surfaces like SiO₂, however, no adsorption is expected for Cn nor for Hg (Fig. 1.12 curve c) [72].

The electronic ground-state configuration for Fl is $7s^27p_{1/2}^2$. The increasing relativistic effects also cause a very large spin-orbit splitting in the $7p$ AO and a strong stabilization of the $7p_{1/2}$ AO for Fl. Resulting from this, Fl has a quasi-closed shell configuration in which the electrons are inaccessible for chemical bonding. Similar to Cn, early theoretical calculations predicted Fl to have a high volatility and chemical inertness [77]. Empirical extrapolations and recent relativistic calculations predict Fl to chemically be more inert than its lighter homolog Pb, in which the relativistic effects are pronounced by the change of oxidation state with respect to the other lighter homologs along the group. As shown in Fig. 1.12, Fl should nevertheless still have a pronounced metallic character, thus forming metal-metal bonds with Au [71,74,76]. Comparing Fl and Cn with each other, it is predicted that Cn is more volatile than Fl. Similar to Cn, Fl is also not expected to adsorb on a SiO₂ surface, whereas Pb shows a strong adsorption on Au as also on SiO₂ (Fig. 1.12) [71,72].

To show the predicted adsorption trend from group 12 up to group 14, Nh and its lighter homolog Tl are also included in Fig. 1.12. Nihonium is expected to be rather reactive on Au and SiO₂ surfaces in comparison to Cn and Fl. This can be explained by the availability of one unpaired electron in its ground-state configuration $7s^2p_{1/2}$ [71,73,76]. However, the strong relativistic contraction and stabilization of the $7s$ and $7p_{1/2}$ AOs and the large spin-orbit splitting are also expected to significantly reduce its reactivity when compared to that of its lighter homolog Tl, such that its interaction strength with the surfaces is expected to be reduced [71,73,76].

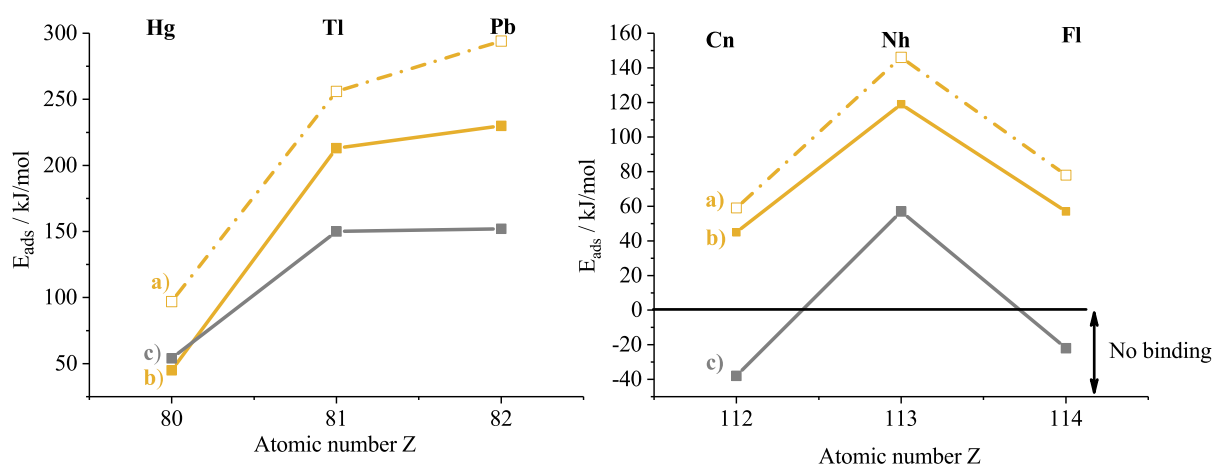


Figure 1.12: Theoretical calculations of the adsorption energy (E_{ads}) for the SHE Cn, Nh, and Fl (right panel) and their homologs Hg, Tl, and Pb (left panel) on Au(111) (curves a and b) and hydroxylated α -quartz (001) surfaces (curve c). The adsorption energies on Au are given for the adatom adsorption in hollow2 position (curve b), and in a vacancy (curve a). The E_{ads} values are taken from Ref. [71–74, 76].

1.5.3 Previous experimental results

The adsorption behavior of the elements Cn and Fl were investigated by gas-solid chromatography on a Au surface [56, 78–85].

First attempts to chemically identify Cn were performed at the Flerov Laboratory of Nuclear Reactions (FLNR) Dubna and GSI Darmstadt, in which ^{283}Cn ($T_{1/2}=3.8^{+1.2}_{-0.7}\text{s}$) was produced in the fusion reaction $^{48}\text{Ca}+^{283}\text{U}$ [78–80]. Due to the low production cross section of 1.5 pb [7] in this fusion reaction, no clear identification of ^{283}Cn could be done and the chemical properties remained unsolved. After the unsuccessful ^{48}Ca on ^{283}U experiments, an attempt was made to investigate the chemical properties of Cn using a reaction that first produced Fl. The reason for this, was the observation of significantly increasing cross-sections from Cn to Fl using ^{48}Ca induced fusion reactions (cf. subsection 1.5.1). However, the produced Fl isotope had to decay rapidly so that its chemical properties could not be measured. On the contrary, the Cn daughter nucleus had to have a sufficient long half-life. The ideal case that fulfilled these requirements was the reaction $^{48}\text{Ca}+^{242}\text{Pu}$, producing ^{287}Fl ($T_{1/2}=0.48^{+0.16}_{-0.09}\text{s}$). This fusion reaction was used for the experiments described in Refs. [81, 84, 85]. The produced ^{283}Cn atoms recoiled from the target into a recoil stopping volume, where they were thermalized and flushed with a carrier gas into the Au-covered chromatography system COLD [46]. A negative temperature gradient was applied along the detector, in which the initial temperature was varied between 35°C and -24° down to -184°C or -164°C , respectively. Aerosol particles produced by beam-induced sputtering processes were stopped directly behind the outlet of the recoil stopping volume on a quartz wool filter heated to 850°C . Only volatile nuclear reaction products could pass the quartz wool filter. The detector was connected to the filter via a 8-m long perfluoroalkoxy- Teflon capillary. A transport time of about 2 s was estimated. No pre-separator was used in the experiments.

In total six α -SF decay chains starting from ^{283}Cn were observed at deposition temperatures of -5, -7, -21, -28, -39, and -124°C [81, 84, 85]. Based on the observations an adsorption enthalpy of Cn on a Au surface was evaluated ($-\Delta H_{ads}^{Au}(\text{Cn})=52_{-3}^{+2}$ kJ/mol (68% c.i.)), which pointed at the formation of a weak metal-metal bond with Au [84]. The adsorption enthalpy demonstrated a higher inertness of Cn compared to its lighter homolog Hg, which is in accordance to the theoretical predictions shown in Fig. 1.12. Another experiment with a similar setup was performed on the chemical investigations of Cn behind the Dubna gas-filled magnetic separator using the reaction $^{48}\text{Ca}+^{244}\text{Pu}$, producing $^{288,289}\text{Fl}$ and its daughter $^{284,285}\text{Cn}$ [82]. One decay chain assigned to ^{285}Cn ($T_{1/2}=28_{-6.0}^{+9.0}$ s) was observed at -93°C [82]. This result was in agreement with the previous observations. A general conclusion was made that copernicium conforms well to the trend in group 12 of the periodic table [84].

Pioneering chemical works on Fl were performed by a collaboration of the Paul-Scherer Institute (PSI), FLNR, and the Lawrence Livermore National Laboratory (LLNL). The experiments were conducted at FLNR in Dubna, Russia. In the above described experiments attributed to determine the chemical properties of ^{283}Cn , one three-member decay chain was registered in the COLD detector at a temperature of about -88°C [84]. This decay chain was attributed to an event of ^{287}Fl reaching the detector, despite of its short half-life and very long transport times in the experiment. An additional experiment with the same experimental setup as used for the Cn studies without pre-separator was conducted at FLNR, in which $^{288,289}\text{Fl}$ was synthesized in the fusion reaction $^{48}\text{Ca}+^{244}\text{Pu}$ [81]. This experiment revealed in two further decay chains that were attributed to ^{288}Fl at temperatures of about -4 and -90° [81], with the same long transport time, three times larger than the half-life of ^{288}Fl ($T_{1/2}=0.66_{-0.10}^{+0.14}$ s). Another problem to the measurement which raised criticism within the scientific community was the significantly large background in the nuclear spectra, since no pre-separator was used. Due to this, the identified Fl decay chains were questioned [86]. The collaboration reported an adsorption enthalpy of $-\Delta H_{ads}^{Au}(\text{Fl})=34_{-11}^{+54}$ kJ/mol (95% c.i.) which was interpreted to reflect a physisorption bond of Fl on Au, resulting in a noble gas like behavior [81]. Nevertheless, the large error bars do not allow to draw a conclusion on whether Fl has a chemisorption or physisorption bond with the Au surface. For the analysis of the Fl results in this thesis, the adsorption enthalpy value is used as a weak adsorption value of Fl on Au. For comparison, the adsorption behavior of the noble gas ^{219}Rn was investigated in the same experimental setup. It was observed that its deposition only occurred at very cold temperatures far below 0°C [56, 81]. The same collaboration performed further Fl experiments behind the GFRS separator at FLNR institute to increase the statistics and prove the determined adsorption interaction of Fl with Au, but no further Fl events were observed. Only decay chains starting from its daughter nuclei Cn were detected, which were distributed on the Au surface in a wide temperature range [57, 83].

The first chemistry experiment with Fl behind the gas-filled separator TASCAs was performed at GSI (Darmstadt, Germany) [56]. $^{288,289}\text{Fl}$ were produced in the reaction $^{48}\text{Ca}+^{244}\text{Pu}$. The Fl isotopes recoiled from the target into TASCAs, in which primary beam and background trajectories of secondary reactions were deflected. In the focal plane of TASCAs a stopping chamber was installed in which the Fl atoms were thermalized and flushed with a carrier gas into the chromatography and detection system COMPACT [47]. The stopping chamber was connected to the detector via a 2-cm long polyfluorethylen (PTFE) capillary. The transportation time was determined to be 0.81 ± 0.06 s [56]. For the first time, two gas chromatography Au-covered detectors COMPACT [47] were operated in series. In this work, the first detector was operated

at room temperature (21°C) as IC, whereas the second was operated with a negative temperature gradient up to -162°C as TC. In total, two Fl decay chains were observed: one attributed to ^{288}Fl and the other to ^{289}Fl . Both decay chains were observed at room temperature. These results confirmed that Fl is volatile, but it was suggested to have a rather metallic character due to its strong adsorption (chemisorption) on the Au surface. An adsorption enthalpy of $-\Delta H_{ads}^{Au}(\text{Fl}) > 48 \text{ kJ/mol}$ (95% c.i.) [56] was determined, which was in accordance to theoretical prediction as shown in Fig. 1.12.

Motivation

Due to limited statistics and contradictive interpretations of the obtained results in the first chemistry experiments of Fl at FLNR and GSI, advanced experimental studies appeared essential to clarify whether Fl has a metal or a noble gas like behavior. Prior to new Fl experiments, the experimental setup was optimized in order to increase its sensitivity. In addition, the chemical procedure was improved to decrease the transportation time, increase the chemical efficiency, and separate elements with different volatilities from each other.

In this thesis, the experimental optimization procedures and new Fl experiments conducted at GSI Darmstadt using the gas-filled separator TASCA in combination with chemical setups are described. The analysis of the obtained data are presented, discussed and compared to theoretical predictions.

Chapter 2

Experimental setup

The experiments discussed in this thesis were conducted at the GSI Helmholtzzentrum für Schwerionenforschung in Darmstadt, Germany. A short overview of the experimental setup will be given here, which will be followed by more detailed explanations of the experimental components in sections 2.1 to 2.5.

The UNiversal Linear Accelerator (UNILAC) accelerated ions to a specific energy towards a thin target [87]. Fusion-evaporation reactions of the ions with the target nuclei produced the desired EVRs, which exited the target into the kinematic recoil separator TASCA [88]. In TASCA, the EVRs were separated from primary beam and unwanted byproducts. In the focal plane of TASCA, a Focal Plane Detector (FPD) could be installed to detect the separated EVRs. Alternatively, an interface for chemistry experiments, the Recoil Transfer Chamber (RTC) could be installed in the focal plane of TASCA [89]. The gas-filled RTC was separated from TASCA by a thin polyethylene terephthalate (trade name Mylar) window. The EVRs passed through the window, were thermalized inside the RTC and were then transported with the help of a carrier gas into the gas-chromatography and detection system COMPACT [47]. In Fig. 2.2 a schematic layout of TASCA in combination with a COMPACT detector array setup is shown.

2.1 TASCA - TransActinide Separator and Chemistry Apparatus at UNILAC

The gas-filled recoil separator TASCA [88] is installed at the X-branch of the linear accelerator UNILAC, as shown in Fig. 2.1.

In the UNILAC, ions of elements from hydrogen up to uranium can be accelerated. Ions from three different ion sources (two located at the (HSI) high-current injection line and one in the high-charge injection line (HLI)) are accelerated to 1.4 MeV/u and then injected into the main LINAC section of the UNILAC, where they can be accelerated to energies up to 11.4 MeV/u. Since the UNILAC provides pulsed beams with a maximum pulse length of about 5 ms and max. repetition rate of 50 Hz, it is possible to conduct several experiments at different experimental stations with different ions in parallel. Typical repetition rates for main users at UNILAC are 43 to 45 Hz.

For chemistry experiments on SHE and their homologs at TASCA, primarily $^{48}\text{Ca}^{10+}$ and $^{50}\text{Ti}^{8+}$ ions are accelerated to energies of 5 to 6 MeV/u. The Ti ions are typically extracted from the Penning Ionization Gauge (PIG) ion source located at the HSI of the UNILAC, whereas the Ca ions are typically extracted

from the Electron Cyclotron Resonance (ECR) ion source, located at HLI. The major advantage of the ECR source is a constant and stable ion beam and very low material consumption for long durations of accelerator operation.

In order to be able to work with high beam intensities up to 10^{13} particles/s, there is no vacuum window between TASCA and the UNILAC. The pressure difference between TASCA (~ 0.8 mbar) and the UNILAC (10^{-7} mbar) is maintained by differential pumping with one Roots pump and two turbo pumps. In this way, the beam intensity is only limited by the UNILAC itself or by the target, as described in section 1.4.

The beam from the UNILAC passes the differential pumping section of TASCA and impinges on the target wheel. The beam intensity is measured by two transformers (trafos). One trafo (UX8DT3) is located closely to the target area, whereas the second trafo (UXADT2) is located towards the UNILAC at the beginning of the X-branch. The beam transmission is determined by the difference between the two measured currents at the trafos.

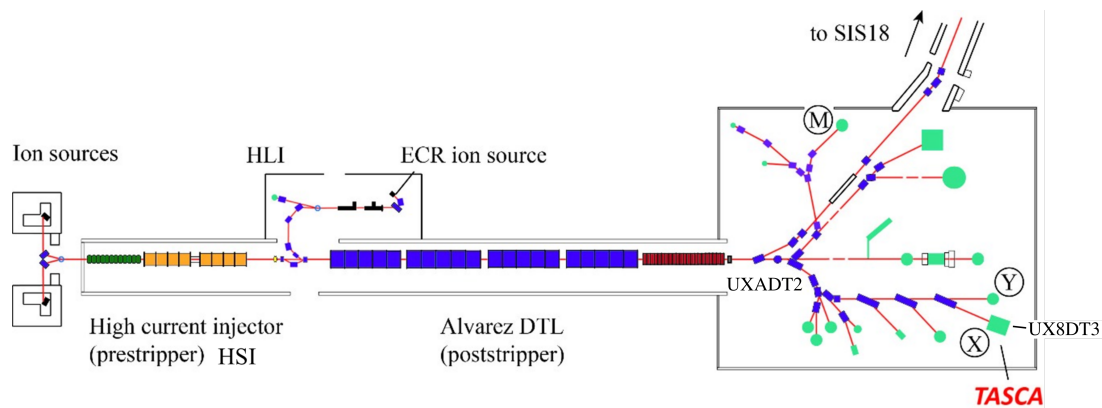


Figure 2.1: Simplified schematic drawing of the linear accelerator UNILAC. Ions, extracted from the ion source are accelerated and lead to the experimental cave X8. Figure taken and adapted from Ref. [90].

The target wheel has a diameter of 10 cm, and consists of 4 segments of 6 cm^2 area, each containing target material on thin Ti foils. It is installed inside a target cassette to prevent contamination of the accelerator or TASCA with target material, which can be highly radioactive (e.g. ^{249}Bk) [91]. Furthermore, several vacuum valves are installed around the target area as barriers in case of a vacuum breakdown at TASCA or the UNILAC. The target wheel rotates synchronously with the macro structure of the beam. The advantage of a rotating target wheel compared to a stationary target is a larger area for irradiation and less thermal stress for the target. One beam pulse only irradiates one target segment, so that during this time, the other segments can cool down [92]. The target temperature is monitored online by means of a pyrometer.

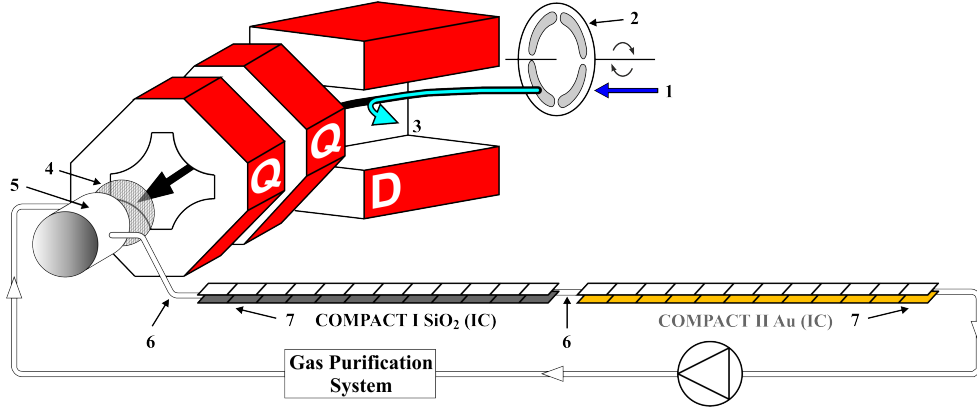


Figure 2.2: A schematic layout of a TASCA+COMPACT arrangement used for gas chromatographic investigations of SHE and homologs. The primary beam (1) passes through a rotating target assembly (2). The separator TASCA consists of one dipole (D) magnet, where unwanted nuclear reaction products and unreacted primary beam (3) are separated from evaporation residues and subsequently focused by means of two quadrupole (Q) magnets. At the exit of TASCA, a vacuum window (4) separates the low-pressure region in TASCA from the high-pressure region in the recoil transfer chamber (RTC) (5). After passing the window, the EVRs are thermalized in the gas inside the RTC and are transported with a carrier gas through polytetrafluoroethylene (PTFE) capillaries (6) into a series of two COMPACT detector arrays (7). To purify the carrier gas, a gas purification system is installed, through which the carrier gas is pumped in a loop. For measurements with the focal plane detector (FPD), which is installed in the position of the RTC (5), the COMPACT detector arrays (as well as the gas loop system) are removed.

The interaction of the beam particles with the target material can lead to the formation of the desired EVRs, which recoil from the target into TASCA due to the transfer of impulse. TASCA consists of one dipole (D) and two quadrupole (Q) magnets [93, 94]. Its magnetic configuration is DQQ in the direction of the beam (Fig. 2.2). The three magnets are filled with ~ 0.8 mbar of He gas. The ions which recoil from the target interact with the He gas and are brought to an average charge state q_{ave} [95] for which holds

$$q_{ave} \propto vZ^{\frac{1}{3}}. \quad (2.1)$$

The velocity of the recoiling ion v depends on the beam energy, nuclear reaction, and target thickness. Z is the proton number of the ion.

Inside the dipole magnet of TASCA, the EVRs are separated from the primary beam and the transfer products according to their magnetic rigidity [95], which is defined as:

$$B \cdot \rho = \frac{mv}{q_{ave}e_0}, \quad (2.2)$$

where B is the magnetic flux, ρ is the gyroradius of the ion due to the magnetic field, m is the mass of the ion, v is the velocity of the ion, q_{ave} is the average charge state and e_0 is the elementary charge.

The two quadrupole magnets are set to focus the EVRs in the horizontal and vertical directions into the focal plane of TASCA, where a FPD (section 2.2) or chemistry device RTC and COMPACT (sections 2.3 and 2.4) is installed.

TASCA can be operated in different ion-optical modes: the High Transmission Mode (HTM) (magnetic configuration: DQ_hQ_v , where the indices refer to vertical (v) and horizontal (h) focusing) and the Small Image Mode (SIM) (DQ_vQ_h) [88]. The advantages and disadvantages of the ion-optical modes will be discussed in section 3.1.1.

2.2 Detection system: Focal Plane Detector

As already mentioned in the section before, the Focal Plane Detector (FPD) can be installed behind TASCA. With this detector, the EVRs reaching the focal plane of TASCA can be measured. For chemistry experiments we use a small FPD (Fig. 2.3) to determine the rate of EVRs passing through the exit window. This is an important reference value to determine the overall chemical yield of the EVRs.

The FPD is a (48x72) mm² Double-Sided Silicon Strip Detector (DSSD), with 16 strips in both the x - and y -directions. The calculated geometrical efficiency for detecting an emitted α -particle following the radioactive decay of an implanted EVRs in the FPD, is about 55%.



Figure 2.3: Photograph of a DSSD, which can be installed behind the exit window in the focal plane of TASCA.

The FPD is calibrated with a four line α -particle source consisting of ²⁴¹Am, ²³⁹Pu, ²⁴⁴Cm and ¹⁴⁸Gd material, which is located externally upstream to the detector. The calibration of the FPD is performed prior to online measurements. In Fig. 2.4, a typical calibration spectrum showing the peaks of the α -particle source is illustrated. In Tab. 2.1 the expected α -decay energies together with the α -decay branches are shown.

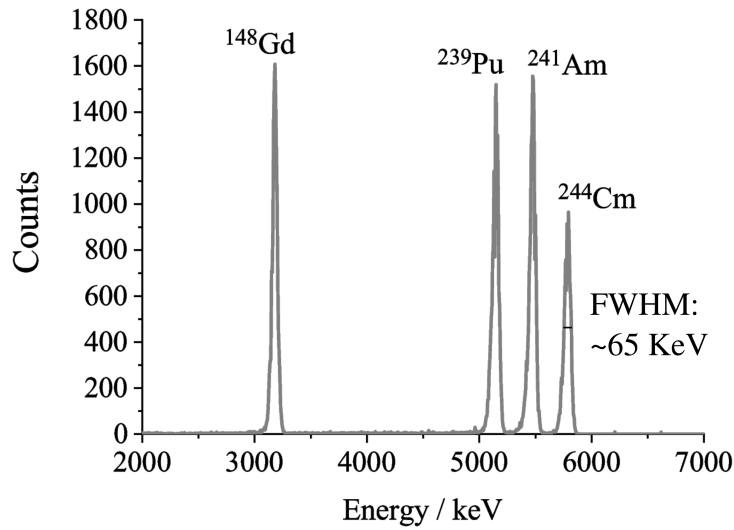


Figure 2.4: Typical α -decay energy sum spectrum of the Focal Plane Detector (FPD) during calibration.

Table 2.1: Decay properties of the nuclides used for the calibration of the FPD [96].

Nuclide	$T_{1/2}$ [a]	B_{α} [%]	I_{α} [%]	E_{α} [MeV]
^{241}Am	432	100	85.0 (10)	5.49
			13.0 (6)	5.44
^{239}Pu	24110	100	73.3 (8)	5.16
			15.1 (8)	5.14
			11.5 (8)	5.11
^{244}Cm	18	100	76.4 (2)	5.80
			23.6 (2)	5.76
^{148}Gd	75	100	100.0	3.27

2.3 Recoil Transfer Chamber and Gas- Transport System

To perform chemistry experiments at TASCA, the FPD is exchanged with the RTC [89]. After separation in TASCA, the EVRs pass through a window into the gas-filled RTC where they are thermalized and flushed with a carrier gas into the detection system COMPACT, (see Fig. 2.2). Accordingly, the stopping power of the chosen carrier gas has to be high enough to fully thermalize the EVRs. Generally, pure Ar gas (purity: 99.999%) or a mixture of He (purity: 99.9999%) and Ar gas was used.

The RTC window has to fulfill two conditions: i) it has to be strong enough to separate the low- pressure region in TASCA from the gas pressure (~ 1 bar) inside the RTC, and ii) the optimal thickness has to be chosen to provide maximum transmission of the EVRs through the window with a minimum remaining recoil range in the RTC [89]. The thickness is selected based on kinetic energy calculations for the EVRs

using the SRIM Code [97, 98]. These calculations indicate the optimum thickness to be in the range of a few micrometers. The window material is made out of polyethylene terephthalate foils and supported by a 1 mm thick stainless steel grid with a geometrical transparency of 80%.

Depending on the ion-optical settings of TASCA, different types of RTC can be used, see Fig. 2.5. They are constructed from different modules with adjustable depth and hence volume of the RTC, depending on the anticipated geometrical distribution of the EVRs. For studies on short-lived SHE small RTCs are preferred, since the flush-out time is reduced and the overall chemical yield is increased. More detailed information on flush-out times and overall chemical yields with different RTCs will be given in chapter 3. All RTCs are polytetrafluorethylen (PTFE) coated, so that the reaction products only interact with PTFE before reaching the detection setup. No strong interaction of SHE with PTFE surfaces have been predicted by theory so far [99, 100].

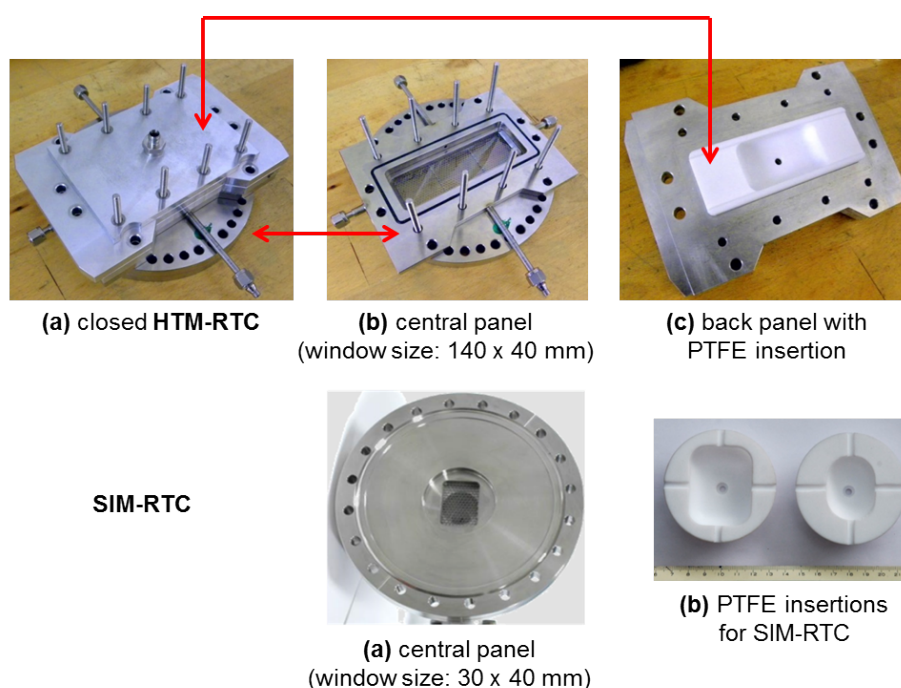


Figure 2.5: Comparison of HTM-RTC, and SIM-RTC. In the first row, Fig. (a) shows the closed HTM-RTC, together with the connecting flange to the detector box of TASCA. In the middle of the back panel the gas outlet is visible, as also on the left side of the picture one of the two gas inlets. The two visible connectors on the top and bottom can e.g., be used for gas pressure control. In Fig. (b) the central panel is shown in direction of the separator. The RTC-window foil as well as the supporting grid are visible. Fig. (c) shows the back panel viewed from the separator side together with its PTFE coated chamber. The small whole in the middle, is the gas outlet for thermalized atoms together with the carrier gas into the detection system. In the second row the SIM-RTC is shown in Fig. (a) and (b).

The RTC and the detection system COMPACT are installed in a gas purification system, in which the carrier gas is constantly circulated with the help of a small membrane pump. A schematic drawing of the system is shown in Fig. 2.6. The He/Ar carrier gas is transported through two purification cartridges of the company Spectromol (Oxysorb and Hydrosorb) operated in series to minimize the oxygen and water content in the carrier gas. The applied processes are based on chemisorption and physisorption. The reactive components and specifications of the cartridges are given in the appendix A.2.3. In this way, unwanted chemical reactions with the EVRs can be avoided, and the formation of ice can be reduced on

the COMPACT detector arrays operated as TC. The gas purity is constantly monitored with a dew point sensor of the company Michell Instruments (model: PURA OEM).

The gas pressure inside the loop, is permanently monitored by a pressure indication and registration device (PIR) and the main gas flow rate can be varied by a mass flow controller (MFC). The initial pressure of the main MFC is monitored at the pressure indication (PI) and is regulated by the pressure regulator (PC) in front of the main MFC. In addition, two more MFCs are used to fill the gas loop with the carrier gas. As mentioned earlier, the ratio of the gas mixture is determined by the nuclear reaction and remaining energy of the EVRs after passing through TASCA. The higher the remaining energy, the more Ar gas is added to the gas mixture to guarantee a full thermalization of the EVRs in the RTC volume, and to avoid losses due to implantation on the RTC wall. To improve the resolution of the α spectra in the COMPACT detectors, He gas instead of Ar is added. More information on the energy resolution of COMPACT detectors in different gases will be given in chapter 3.

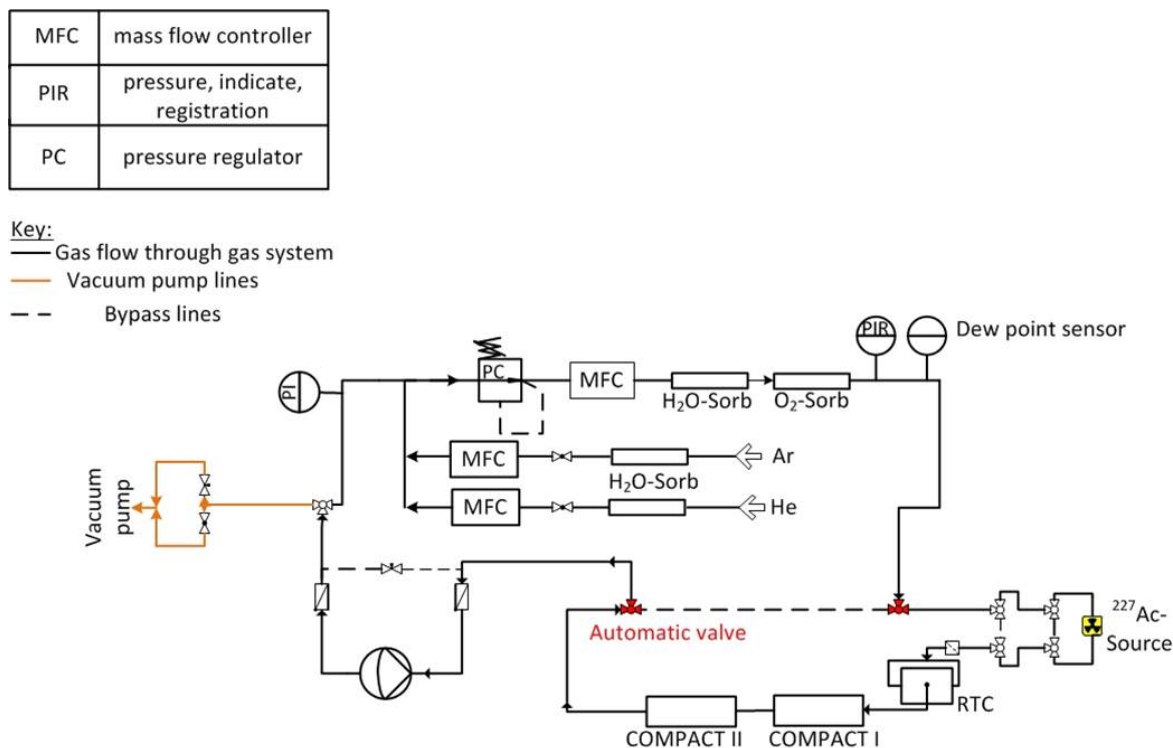


Figure 2.6: Schematic drawing of the gas loop purification system. With the help of a membrane pump the He/Ar gas mixture is transported in a loop over several gas purification cartridges. It flushes the RTC where it thermalizes the EVRs and transports them to the COMPACT detector arrays. For more details, see text.

The MFCs are controlled by a LabView program in which threshold values for pressure control are set. As soon as the gas pressure decreases below the threshold value, e.g., due to a break of the RTC window, two automatic valves are shut to isolate the RTC and COMPACT detectors arrays from the rest of the gas purification system. In normal operation, a threshold value is set for the gas pressure of the loop, and the MFC of the He/Ar gas inlet are opened automatically to refill gas to the system.

When a COMPACT detector array is used as a TC column, the temperature is monitored with four type K temperature sensors, and is read out in the LabView program. For this, four temperature sensors are

mounted at equal distances to each other on the metal panels of the COMPACT array.

With the exception of the connection between the RTC and COMPACT detector arrays, all connection tubes are made out of 6 mm stainless steel. The connection of RTC and COMPACT detector arrays are made out of PTFE as mentioned before.

In order to calibrate the COMPACT detectors, a ^{227}Ac source is inserted into the gas purification system. More information on the calibration of the COMPACT detectors is given in the following section.

2.4 Detection system: COMPACT

As described in section 1.4, the detection system COMPACT [47] is simultaneously used as a chromatography and a detection device. The basic design of such a detection system was developed by Kirbach *et al.* [101] and successfully applied for a transactinide element for the first time by Düllmann *et al.* [102] by observing the nuclide ^{269}Hs and its decay daughters after chemical isolation.

The COMPACT detector array consists of two metal panels made from INVARTM (Ni-Fe) alloy, which are attached together with indium-wire sealing forming a vacuum tight gas channel. INVARTM is chosen because of its extremely low thermal expansion. Each array consists of 32 pairs of (1x1) cm²-large positive-intrinsic-negative (PIN) epitaxial silicon photodiodes. They have an active area of (9.7x9.8) mm² and an effective thickness of 150 μm . A gap of 0.6 mm between the top and the bottom 32 PIN diode pairs forms a gas channel through each COMPACT detector array. The COMPACT detectors are suitable for the detection of α -particles and SF fragments. The calculated geometrical efficiencies for detecting a single α -particle and spontaneous fission from atoms present inside the detector array are about 76%, and 100%, respectively [58].

The surface of the PIN diodes can be covered with a thin layer of different materials (Au or SiO₂), depending on the chemical properties of the element or compound to be investigated. Depending on the interaction strength of the atoms with the surface, the decay of the atoms can be observed on either the Au or SiO₂ surface. The SiO₂ surface is created through oxidation of Si, while the Au is deposited by evaporation under vacuum at temperatures of around 100 to 130°C [103], on the silicon diodes. Both surfaces have a thickness in the range of 30 to 50 nm. A Au-covered COMPACT detector array is shown as an example in Fig. 2.7. COMPACT detector arrays with different surfaces can be used in series. In addition, a combination of both surfaces in one detector array is possible.

The COMPACT detector arrays can be operated as an isothermal chromatograph (IC), e.g., at room temperature (21°C), or as a thermo chromatograph (TC) in which a negative temperature gradient is applied along the detector down to temperatures around $\sim -160^\circ\text{C}$. One end of the detector array is cooled down with liquid nitrogen. The carrier gas transports volatile species from the warm end of the detector to the cold end. In order to avoid condensation of the air moisture and improve thermal isolation, the COMPACT detectors are installed inside an evacuated detector box.

The COMPACT detectors are calibrated with α -particles from the decay of ^{219}Rn and its daughters, emanating from a ^{227}Ac source.

gas as well as the gas pressure, the peak maximum can move to lower energies when the α -particle goes directly into the PIN without passing through the gas, due to energy loss in the gas. The detectors are calibrated under the same experimental conditions as used for SHE and their homologs. The peak maxima are calibrated using the α -decay energies shown in Tab. 2.2.

Table 2.2: Decay properties of the nuclides used for the calibration of COMPACT [96].

Nuclide	$T_{1/2}$ [s]	B_α [%]	I_α [%]	E_α [MeV]
^{219}Rn	3.96	100	79.40 (10)	6.82
			12.90 (6)	6.55
			7.50 (6)	6.43
^{215}Po	0.18	100	100	7.39
^{211}Bi	12840.00	100	83.80 (14)	6.62
			16.20 (14)	6.28

2.5 Data acquisition system

The signals from COMPACT's PIN diodes and the FPD strips are processed using a combination of analog and digital electronics. In Fig. 2.9, a simplified scheme of modules used in the data acquisition system is shown.

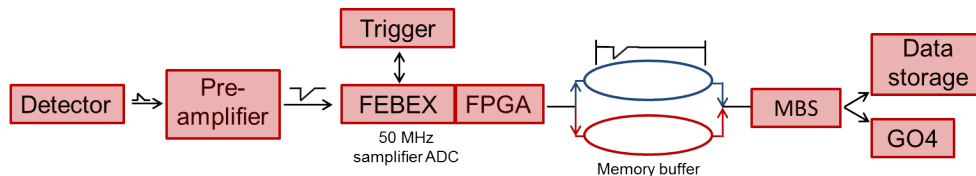


Figure 2.9: Simplified schematic of the full digital electronics used for the experiments.

The detector signals are sent to charge sensitive Pre-Amplifier (PA) modules for initial amplification. Following this, the differential signal outputs are transmitted to pipelining ADC (Analog Digital Converter) boards integrated in a Front End Board with optic link Extension (FEBEX) 3A (designed and developed in-house at GSI), cf. Fig. 2.10.

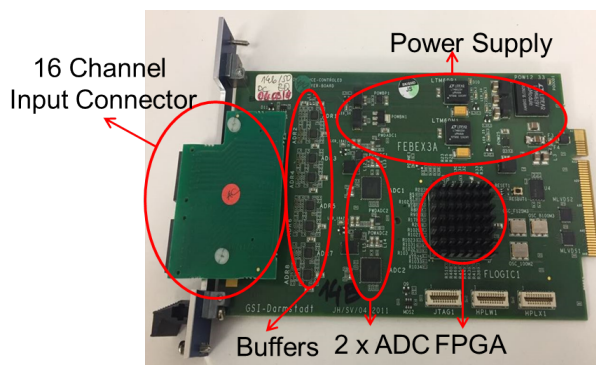


Figure 2.10: Front End Board with optic link Extension (FEBEX) 3A module.

The FEBEX 3A digitizers consist of two analog buffers coupled to ADCs, enabling an almost dead time-free system. Onboard, a Field Programmable Gate Array (FPGA) is used to perform a moving window deconvolution algorithm on the digitized traces, in order to extract energy information for a given signal. Each FEBEX board has a total of 16 channel inputs. For the work presented here, a total of 128 channel outputs were fed to 8 FEBEX boards, with one additional module used for logical signals such as macropulse structure, and chopper signals for start and stop of irradiations in the transport time measurements. An external trigger module was coupled to the system, containing the FEBEX boards for time synchronization of the modules. The energy, timing and trace information are sent from the FEBEX system to a Multi Branch System (MBS) via an optical link cable. The MBS enables storage of the data and provides an on-line analysis. The data is unpacked and sorted, calibrated and histogrammed using the ROOT-based analysis software Go4 and spectral event search analysis. From Go4 the data can be exported as ASCII data sets into programs such as Origin, and can be further analyzed there.

Chapter **3**

Technical optimizations of the experimental setup

Prior to new investigations on the chemical properties of Fl, and future chemical studies on e.g. Nh ($T_{1/2} \sim 1$ s) and heavier SHE, the chemical procedure had to be optimized. This included the improvement of the overall chemical yield, transportation time and chemical separation of elements with different volatilities and reactivities from each other.

All experiments were performed with short-lived isotopes of the lighter homologs Hg, Tl, and Pb since they could be produced with significantly higher rates in fusion reactions than the SHE. The experiments were performed under the same conditions as used for the SHE studies.

Initially the improvement of the chemical separation in the COMPACT detection system was conducted, in order to study and compare the chemical behavior of the SHE directly to their lighter homologs. The results + discussion on the chemical separation of the short-lived Hg, Tl, and Pb isotopes in the detection setup will be given in chapter 4.

To increase the detection rate of Fl events, the overall chemical yield and the transportation time had to be optimized. The overall chemical yield, which is defined as the ratio of produced EVRs present in the RTC and the portion of EVRs detected in the COMPACT detection system, had to be maximized. Hereby the detection efficiency to observe an α -decay had to be taken into consideration. Since the overall chemical yield is also dependent on the half-life of the produced EVRs, the transportation time for the EVRs being flushed from the RTC into the COMPACT detector system had to be minimized to prevent decay losses. The transport time of the EVRs through TASCA ($\approx 0.7 \mu\text{s}$) was neglected, due to its minimal influence.

In this chapter, a short overview will be given on the different optimizations of the experimental setup to increase the overall chemical yield, and decrease the transportation and flush-out time. Furthermore, the results of offline as well as online test experiments with the lighter homologs will be discussed and compared to former results given in Ref. [56].

3.1 Technical Optimizations

3.1.1 TASCAs

As already mentioned in section 2.1, TASCAs can be operated in different ion-optical modes. So far the High Transmission Mode (HTM) and the Small Image Mode (SIM) were mentioned. The main difference between SIM and HTM is the order of Q_v and Q_h . Whereas in SIM the species passing through the dipole magnet are first focused in vertical and then in horizontal direction, in HTM this is reverse. Both ion-optical modes have advantages and disadvantages [88].

The main advantage of the SIM is a small image size of about $3 \times 3 \text{ cm}^2$ in the focal plane of TASCAs. A small image size allows using a smaller RTC window, and therefore a smaller RTC volume. This is crucial for a fast flush-out and transport time of the short-lived nuclei to the COMPACT detectors. For this reason, the first chemistry experiment on FI at TASCAs was performed with the SIM [56]. For comparison, the full image size in HTM is about $12 \times 4 \text{ cm}^2$ [88]. The disadvantage of the SIM is a lower transmission (30-35%) for EVRs in comparison to the HTM, in which a transmission of 60% can be achieved for ^{48}Ca induced reactions [88]. This can be explained due to large defocusing in the x -direction in the first quadrupole magnet, when TASCAs is operated in SIM. It causes many losses in the walls from unwanted background products (e.g. transfer products, and primary beam), but in addition also from the desired EVRs.

Experiments in which TASCAs was mainly operated in HTM showed that a fraction of the transfer products which have a similar magnetic rigidity as the desired evaporation residues, as well as scattered primary beam could be transported to the FPD of TASCAs [104]. Ion-optical simulations were performed, and two additional slits were installed (one inside Q_1 , and the second after Q_2) to reduce the background from scattered primary beam ions, and from lighter transfer reactions products. Experiments showed a reduction of the background by factor 10 and only $\leq 10\%$ decrease of the transmission for the EVRs through TASCAs [105, 106].

Due to the installation of the slit in Q_1 , the transmission of the SIM was reduced even more, so that this ion optical setting became unattractive for SHE chemistry experiments. Instead, the combination of SHE chemistry studies with TASCAs operated in HTM was considered. In order to keep the transport time relatively short, a RTC window size of $6 \times 4 \text{ cm}^2$ was chosen. The ion-optical settings for HTM were simulated and optimized accordingly, to focus the beam spot in the focal plane of TASCAs to the RTC window size. Measurements with $^{48}\text{Ca} + ^{206-208}\text{Pb}$ were performed, which showed that in reality the EVR distribution was slightly larger ($8 \times 4 \text{ cm}^2$) [107]. This caused some losses due to implantations of the EVRs into the wall of the RTC window flange. Nevertheless a transmission of about 40% could be achieved. These new settings were successfully used in many different experiments performed at TASCAs [105, 106], including the optimized investigations on the chemical properties of FI (see chapter 6).

3.1.2 Recoil Transfer Chamber

The main contribution to the transportation time is the time which is needed to flush out the thermalized EVRs from the RTC to the COMPACT detectors. This is influenced by many parameters such as the RTC

depth, the gas flow rate of the carrier gas, as well as the transport tube lengths.

In order to keep the transport time reasonably low, the RTC window and the RTC itself were optimized. As already mentioned in the section before, the window size was chosen to be $6 \times 4 \text{ cm}^2$. In Fig. 3.1 the connecting detector box to TASCA together with the central panel and the RTC window foil with supporting grid are shown.

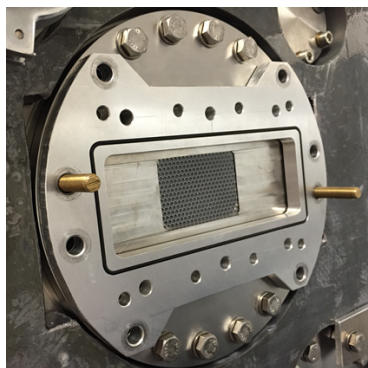


Figure 3.1: Connecting flange to the detector box of TASCA for the new HTM RTC. The RTC window ($6 \times 4 \text{ cm}^2$) with supporting grid, together with the central panel in direction of the separator are visible.

Two new Recoil Transfer Chambers were developed and tested online with short-lived Hg and Pb isotopes. Some offline tests were performed with an ^{227}Ac source. In order to minimize the chemical reactions of the EVRs with the walls, both RTCs as also transport tubes were PTFE coated as discussed in section 2.3.

Fig. 3.2 shows the HTM RTC developed in 2014. The advantage of this RTC was its mechanically adjustable depth, with a minimum of 1 cm (volume: 24 cm^3), and a maximum depth of 4 cm (volume: 96 cm^3). The disadvantage of this mechanism was a long connection capillary of 40-cm length, between the RTC outlet and the first COMPACT detector array. Detailed information on the test experiments will be given in the section 3.2.

Based on the results and discussion of the test experiments, see sections 3.4, and 3.5, a new optimized RTC was developed in 2015, compare Fig. 3.3. Three major changes were applied:

- In contrast to all the previous RTCs in which only the RTC volume was PTFE coated, the new RTC was fully PTFE coated to avoid any possible kind of losses due to chemical reactions of the EVRs with steel surfaces.
- The RTC had a fixed depth of 2 cm, resulting in a volume of 48 cm^3 . To thermalize EVRs within the 2 cm depth, the carrier gas mixture of He and Ar gas and the gas pressure had to be adjusted individually, to thermalize the EVRs when passing through the RTC window, to avoid losses of implantation into the RTC walls.
- The transport tubes between the RTC outlet and the first COMPACT detector array as also in between of the COMPACT detectors, were shortened to 5 cm (\varnothing_i 3 mm) and 20 cm (\varnothing_i 2 mm) respectively.

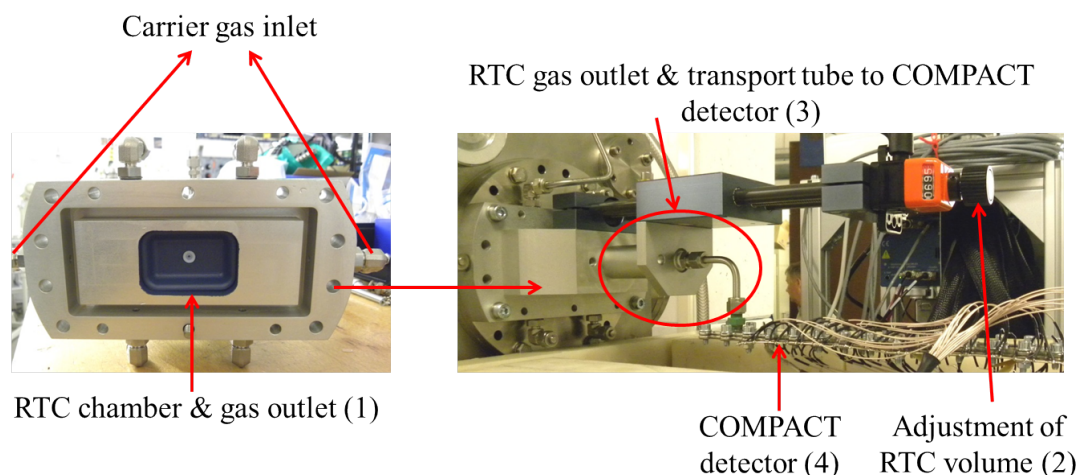


Figure 3.2: *HTM RTC developed in 2014 and used for test experiments with short-lived Hg and Pb isotopes. On the left hand side, the RTC in beam direction is shown (1). The PTFE coated RTC volume is mechanically adjustable, which can be seen in the right figure (2). Furthermore, the PTFE connection capillary between the RTC outlet (3) and the COMPACT detector array (4) is shown. The capillary is encapsulated by a steel tube (\varnothing_i 6 mm).*

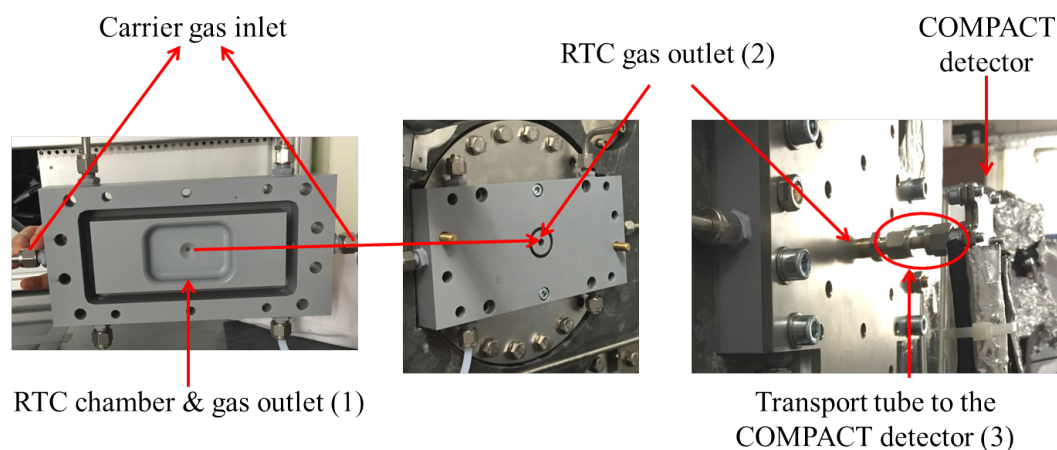


Figure 3.3: *Optimized HTM RTC developed in 2015 and used for test experiments with short-lived Hg and Pb isotopes. On the left hand side, the RTC in beam direction is shown (1). In comparison to the former RTC, this one is completely PTFE coated, and its volume is fixed to 48 cm^3 . In the middle pictures as also in the one on the right hand side, the gas outlet of the RTC (2) and short PTFE connection tube (3) to the COMPACT detector array is illustrated.*

3.1.3 Gas Chromatography and Detection System COMPACT

In order to broaden the range of experimentally accessible chemical reactivity of different elements, the surface of the COMPACT detectors was extended. Next to the Au surface which was used for example in Ref. [56], COMPACT detector arrays with a SiO_2 surface were produced. The elements of interest for comparison to Cn, Nh, and Fl were the non volatile metals Pb and Tl, the volatile metal Hg, as also the noble gas Rn. As illustrated in section 1.5.2, theoretical calculations showed that these elements had different interaction strengths with the two surfaces [71–73]. The deposition of the short-lived isotopes of Hg, Tl,

and Pb on the Au and SiO₂ surfaces was dependent on their volatility, their interaction with the surface, gas flow rate, pressure, gas composition of the carrier gas, as well as the temperature profile applied along the detector array. Depending on the gas ratio and pressure of the carrier gas, the distribution width of the species inside the COMPACT detector differed. The presence of He gas narrowed the distribution pattern of the EVRs inside the COMPACT detector array, which caused the EVR atoms to diffuse faster towards the walls of the detector, where they were immobilized and undergo decay. In pure Ar gas, the EVR atoms were transported further along the detector column, before colliding with the walls and undergoing decay. This deposition process inside the detector array which occurred for strongly interacting species, is referred to as diffusion-controlled deposition.

The distribution of the EVRs which underwent diffusion controlled deposition (i.e., Pb and Hg) in the detector column was measured to be at maximum 16 PIN diodes wide. The composition of the carrier gas did not only have an influence on the distribution pattern, but also on the α decay energy resolution of the spectra. The FWHM of the peaks measured by the Si-detectors when placed in vacuum and irradiated with α -particles incoming normal to the detector surface was ≈ 50 keV. When α -particles were emitted from species located inside the detector channel, the energy resolution was reduced and a low-energy tailing appeared. This was due to i) additional energy loss inside the gas in the channel and ii) some particles hitting the surface of the detector under a shallow angle. The first aspect depended on the pressure and composition of the carrier gas: the heavier the gas the larger the energy tailing. The second aspect led to an increased energy loss in the detector dead layer. For measurements using pure Ar gas at 1 bar pressure, the FWHM was about 200 keV. When pure He was used at 0.3 bar pressure, it was about 100 keV. The gas flow rate of the carrier gas had a substantial influence on the chemical separation of the EVRs in the detector column. It was observed that with increasing gas flow rate, the interaction time of the EVRs with the surfaces decreased and due to this the separation was negatively affected.

To reduce the transport time along the experimental setup, a new COMPACT detector array was developed, in which the SiO₂ covered, and Au-covered Pin diodes were combined, Fig. 3.4. Thus the first 16 PIN diodes of the detector were SiO₂ and the last 16 PIN diodes of the detector were Au-covered.

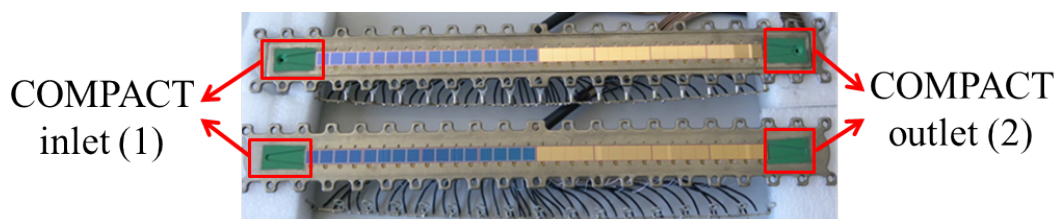


Figure 3.4: COMPACT detector array with combined SiO₂ and Au surfaces. The COMPACT inlet (1), as also the COMPACT outlet (2) are both PTFE coated.

By using the COMPACT detector arrays with Au and SiO₂ surfaces in series, and additionally varying the temperature along the detector arrays (IC or TC), it was possible to separate the elements of interest which differ significantly in their volatility and reactivity to the used hetero-surfaces. The experimental parameters will be discussed in chapter 4.

Additionally the DAQ system was upgraded to a digital readout system as discussed in section 2.5.

3.1.4 Gas- Transport System

As already described in section 2.3 and shown in Fig. 2.6, the He/Ar carrier gas mixture was constantly circulated with the help of a small membrane pump and forced to pass gas purification cartridges suitable to minimize the oxygen and water contents in the carrier gas. In this way, unwanted chemical reactions of the EVRs could be avoided, and the formation of ice could be reduced on the COMPACT detector arrays used as TC. The purity of the gas mixture was constantly measured with a dew point sensor. This gas transport system was used for the first FI experiment at TASCA [56]. The dew point measurements resulted in -60°C .

To improve the reduction of water and oxygen contents in the carrier gas, a new optimized gas transport system was designed and constructed. A schematic drawing of the optimized system is shown in Fig. 3.5. The basic elements, as a small membrane pump to circulate the He/Ar carrier gas through the system was kept the same. Furthermore, monitoring and regulation of the gas pressure inside the loop, as also of the MFCs were controlled with the LabView program mentioned in section 2.3. The main difference to the previous system was the amount of purification cartridges. Whereas before, the carrier gas was purified by one Hydrosorb and one Oxysorb cartridge, it was now purified by several Oxysorb and Hydrosorb cartridges of different sizes. The companies Spectromol and Agilent Technologies provided the cartridges. In addition, a hot moisture getter of the company SAES (model: Mono Torr PS4-MT3-R-2) was installed in series. Specifications of the cartridges and hot moisture getter are listed in the appendix A.2.3. The gas purity was constantly measured with the dew point sensor of the company Michell Instruments (model: PURA OEM), as well as with a quadrupole mass spectrometer (QMS) of the company MKS Instruments (model: RVC2). The optimized gas transport system was used for all experiments reported on in this thesis. Dew point measurements resulted in -79°C . This shows that the optimizations improved the reduction of the water and oxygen contents in the He/Ar carrier gas mixtures. Measurements of the gas purity with the QMS showed oxygen and water contents below 1 ppm, which supports the improvement.

3.2 Online and Offline Experiments

With the new HTM RTCs developed in 2014 and 2015, two online experiments were performed in which transport times and overall chemical yields were determined with short-lived Hg and Pb isotopes. In the following sections, the experiment in 2014 will be referred to with its experimental number T039, and for the experiment 2015 its experimental number T041 will be used. An overview on the experimental parameters are listed in Tab. 3.1.

A beam of $^{48}\text{Ca}^{10+}$ ions provided by the UNILAC was accelerated to an energy of 5.41 MeV/nucleon. Typical repetition rates for Pb were 45 Hz, and 5 Hz for Hg respectively. For the highest repetition rate, beam intensities up to 10^{13} particles/s could be delivered by the UNILAC at a pulse length of about 5 ms. The beam projectiles passed through a Ti backing foil of $2.3\ \mu\text{m}$ thickness before entering the $^{142}\text{NdO}_3$, or $^{144}\text{SmO}_3$ targets. The four segments of the target contained $\approx 260\ \mu\text{g}/\text{cm}^2$ target material. In complete fusion reactions, $^{190}\text{Hg}^*$ and $^{192}\text{Pb}^*$ compound nuclei were formed at an excitation energy of about 60 MeV. After de-excitation, by evaporation of several neutrons a fraction of the resulting isotopes of Hg, and Pb recoiled from the target into TASCA. It was operated in the optimized HTM, as discussed in section 3.1.1.

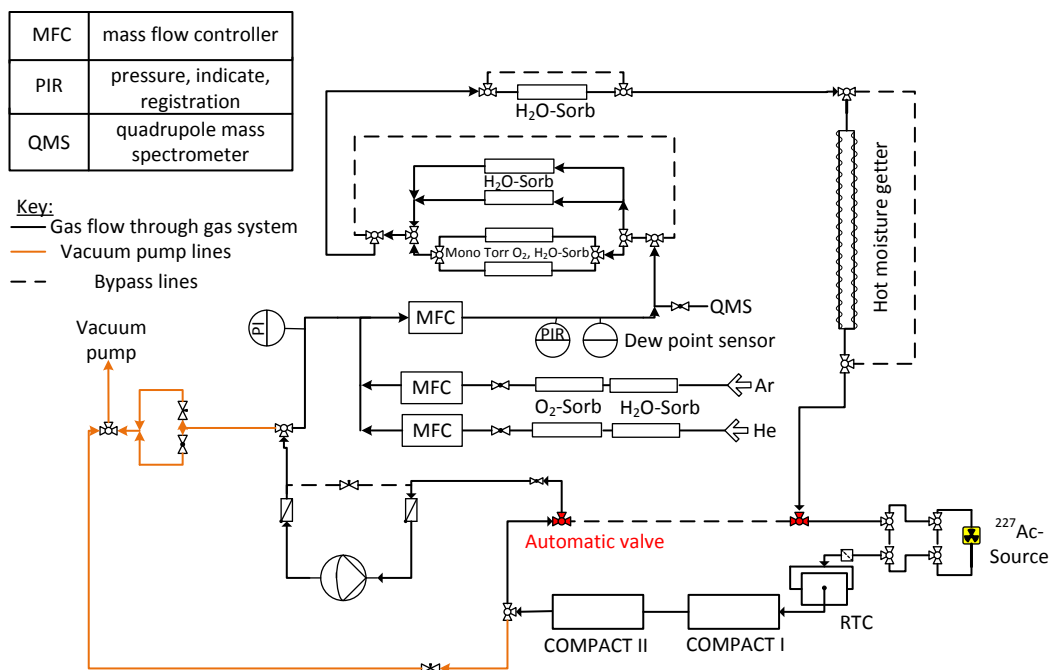


Figure 3.5: Schematic drawing of the improved gas loop purification system. With the help of a membrane pump the He/Ar gas mixture is transported in a loop over several gas purification cartridges. It flushes the RTC where it thermalizes the EVRs and transports them to the COMPACT detector arrays. For more details, see text.

Tab. 3.2, shows the projectile-target combinations used to produce isotopes of Hg and Pb. For the α -decaying isotopes of Hg and Pb, the most intense decay channels according to HIVAP calculations [68,108] are 6 to 8n, corresponding to $^{182-184}\text{Hg}$ and 5 to 7n, corresponding to $^{185-187}\text{Pb}$. The HIVAP plots are given in the Appendix Fig. A.1 and Fig. A.2. Additionally, in Tab. 3.2 decay modes of primary products, the relative α -decay probability (B_α) and most intense α lines (E_α) are shown.

The Hg and Pb ions were guided through TASCA into the focal plane of the separator. To determine the rate of Hg and Pb atoms entering the RTC, measurements with the Focal Plane Detector were performed. The FPD was installed in the position of the RTC vacuum window for experiment T039. For experiment T041, it was installed behind the RTC window of 6 μm thickness and supporting grid, in the RTC position.

To determine the rate of Hg and Pb atoms being transported to the COMPACT detector arrays, as well as for the transport time measurements, the new HTM RTCs as discussed in section 3.1.2 were installed in the focal plane of TASCA. The Hg and Pb isotopes were thermalized in He and Ar gas mixtures, and then flushed with a total gas flow rate of 1.5 or 2.0 L/min into the COMPACT detector arrays. The gas circulated in the optimized gas transport system shown in Fig. 3.5. For the experiment T039, the Hg and Pb isotopes were flushed from the RTC through a 40-cm long PTFE capillary (\varnothing ; 2 mm) into the first of

Table 3.1: Detailed information on the experimental parameters to determine the transport time and chemical efficiency with short-lived Hg and Pb isotopes. Hereby the optimized RTCs from 2014 and 2015 were used. Fluctuations in the pressure were about ± 20 mbar.

Experiment	T039		T041	
Beam				
Projectile	$^{48}\text{Ca}^{10+}$			
Beam energy by UNILAC [MeV]	260			
Repetition rate [Hz]	5	45	5	45
Target				
Composition	$^{142}\text{NdO}_3$	$^{144}\text{SmO}_3$	$^{142}\text{NdO}_3$	$^{144}\text{SmO}_3$
Thickness of metal [$\mu\text{g}/\text{cm}^2$]	278	268	278	268
Ti backing thickness [μm]	2.3			
TASCA				
Ion-Optical settings	Optimized HTM			
Magnetic rigidity $B\rho$ of central trajectory [Tm]	1.61			
RTC & Gas system				
RTC type	Optimized-RTCs			
RTC window thickness [μm]	8.5		6.0	
RTC depth [cm]	3.7		2.0	
Carrier gas	70% He / 30% Ar		30% He / 70% Ar	
Pressure in gas system measured at PIR [mbar]	1330	1346	1025	1000
Gas flow rate (norm. to 1 bar) [L/min]	1.5		2.0	

two COMPACT detector arrays. The connection length between the COMPACT detector arrays was about 30-cm (\varnothing_i 2 mm). In the improved experiment T041 the connection between RTC and COMPACT I, was exchanged by a 5-cm long PTFE tube (\varnothing_i 3 mm), and the connection between the detectors was exchanged to a 20-cm long PTFE tube (\varnothing_i 2 mm).

For both experiments, two COMPACT detector arrays were operated in series. The PIN diodes of COMPACT I were covered with a SiO_2 surface, whereas the PIN diodes of COMPACT II were covered with a Au surface. Both detector arrays were operated at room temperature (21°C).

For transportation time measurements, a constant ion beam is not suitable. Rather a pulsed injection is crucial to measure the time needed for the EVRs to cross the RTC into the COMPACT detection system. As a consequence, the ion beam was chopped in specific time intervals. For the measurements in T039, the target was irradiated for 1 s and then an irradiation pause of 49 s was set. Due to the half-lives of 10.8 s for ^{183}Hg and 8.8 s for ^{182}Hg , we could measure the transport time of the accumulated decay curve in the Au-covered COMPACT detector. For the experiment T041, the irradiation time of the target was only 0.1 s and the irradiation pause 5 s. With these settings, we measured the flush-out curve of Hg decaying in flight on the SiO_2 -covered COMPACT detector. For the overall chemical yield determination in experiment T041, the same irradiation cycle was used.

To obtain more information on the influence of parameter changes (e.g. gas flow rate, carrier gas mixture and RTC depth) to the transportation time, offline experiments were performed with the RTC developed

Table 3.2: ^{48}Ca induced reaction for Hg, and Pb isotopes production to determine the overall chemical efficiency and transport time. The beam energy in the center of the target considered in HIVAP calculations was 242-246 MeV, depending of the thickness of the individual targets. Calculated cross-sections and decay properties [96, 109] relevant for the data analysis are given.

Reaction	Evaporation channel	Primary products	σ [mb]	Decay mode	B_α [%]	E_α [MeV]	$T_{1/2}$ [s]	Decay products
$^{48}\text{Ca} + ^{142}\text{Nd}$	xn	^{182}Hg	0.001	α EC/ β^+	13.80 (2)	5.87	10.80	^{178}Pt ^{182}Au
		^{183}Hg	3		11.70 (20)	5.90	8.80	^{179}Pt ^{183}Au
		^{184}Hg	30		1.11 (6)	5.54	30.60	^{180}Pt ^{184}Au
$^{48}\text{Ca} + ^{144}\text{Sm}$	xn	^{185}Pb	0.001		≤ 100	6.41	4.10	^{181}Hg ^{185}Tl
		^{186}Pb	2		40.00 (8)	6.33	4.83	^{182}Hg ^{186}Tl
		^{187}Pb	4		9.50 (20)	6.07	18.30	^{183}Hg ^{187}Tl

in 2014. For this, a simplified form of the gas transport system discussed in section 2.3 was used. A mixture of He and Ar gas was flushed through purification cartridges to reduce the H_2O and O_2 content. Then the mixture was flushed into the RTC and Au-covered COMPACT detector array. The COMPACT detector was operated at room temperature. If not mentioned differently, the ratio of the carrier gas was 30% He and 70% Ar. The gas flow rate was varied in the range of 1.0 to 3.0 L/min. A branch in the He gas line was connected to the ^{227}Ac -source from which ^{219}Rn emanated and was transported along with the He gas. With a short pulse of 0.1 s every 5 to 10 s, ^{219}Rn was sprayed with an injection valve from the company BOSCH (model: HDEV 5.1, maximum operation pressure: 150 bar) into the RTC volume. The injection valve was installed in a back panel opposite to the RTC outlet. In Fig. 3.6b), a schematic drawing of the experimental setup used in the offline studies is shown in comparison to the setup used in online experiments (Fig. 3.6a)). Detailed information on this figure will be given in section 3.5.

Three installation positions could be chosen from varying the spraying angle into the RTC from central to lateral. The valve was operated at over pressures of around 1 to 2 bar. According to the specifications, its overall spray angle was about 110° . A 30-cm long PTFE capillary (\varnothing_i 2 mm), connected the RTC with the COMPACT detector array. Throughout the experiments, several parameters were varied and their influence on the average transport time (t_{50}) were investigated:

- The spraying angle into the RTC from central to lateral positions.
- The carrier gas composition (70% He / 30% Ar vs. 100% Ar) at fixed RTC depths of 20 and 30 mm and fixed gas flow rate of 3.0 L/min.
- The RTC depth between 10 and 30 mm, at a fixed carrier gas composition (30% He / 70% Ar), at varying gas flow rates between 1.0 to 2.0 L/min.

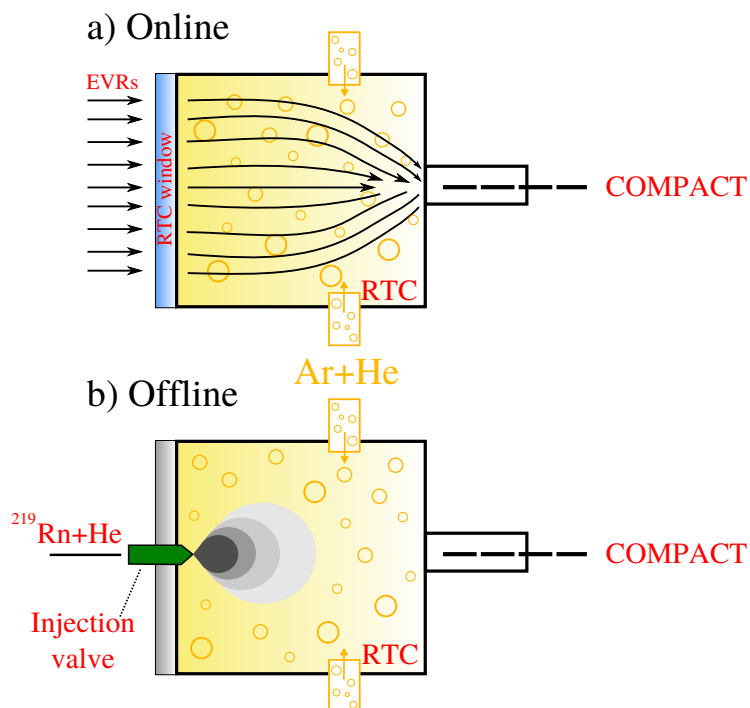


Figure 3.6: Comparison of the spatial distribution of the atoms in the RTC volume in the online (a) and offline (b) experiments. The RTC volume in both cases is flushed with a He and Ar carrier gas mixture. Fig. a) shows homogeneous distribution of the EVRs entering the RTC volume through the RTC window. In Fig. b), the injection of ^{219}Rn atoms into one spot of the RTC volume is illustrated. From this an atom "cloud" is formed which diffuses into the gas mixture.

3.3 Analysis

3.3.1 Transportation time

As already described in the section before, two methods were used to determine the transport time of $^{182-184}\text{Hg}$ in the experimental setup. In this subsection, the principle which was used to determine the transport time from the measured flush-out curve of Hg, decaying in flight on the SiO_2 -covered COMPACT detector array will be described.

Fig. 3.7 shows a typical measured flush-out curve, in which the number of detected decays per 0.0245 s against the time is plotted. Typically long measurement times of 10 to 14 hours were chosen.

Depending on the set parameters (gas flow rate and carrier gas mixture), the flush-out curve showed a peak at ~ 0.2 s after the beam pulse started. The atoms were flushed-out of the RTC and the curve converged to a minimum value, which was the background level. The average background level shown as the red line in Fig. 3.7 was determined, and subtracted in the entire time period of the sum of the decays. At a constant gas flow rate, the measured rate in an energy range (4 to 6.2 MeV) was connected to the number of flushed atoms per time unit. Depending on the parameters of the experiment, the form of the flush-out curve changed. Because of this, the maximum of the curve was not sufficient to compare transport times of different experiments with each other. A more reliable variable was the time in which 50% of the flushed-out atoms were detected, named the 50%-transportation time (t_{50}). This value was obtained by

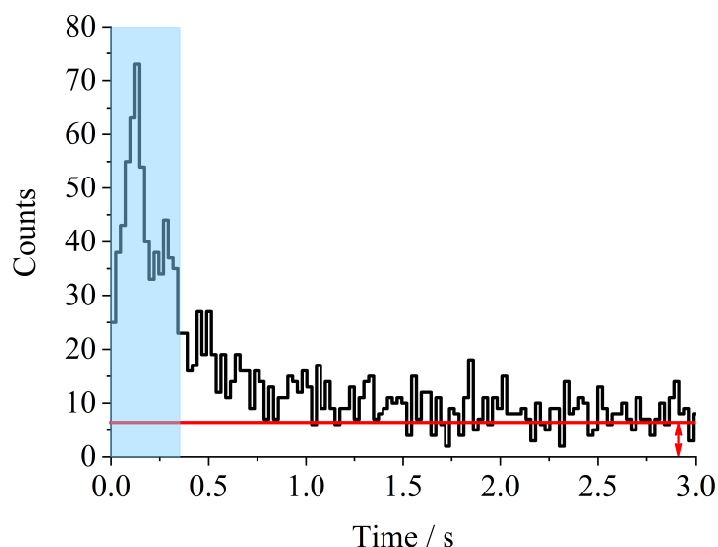


Figure 3.7: Flush-out curve of $^{182-184}\text{Hg}$ decaying in flight on the SiO_2 surface of the first COMPACT detector in the energy range of 4-6.2 MeV. The red line illustrates the average background level. The blue colored area shows the average transport time in which 50% of the $^{182-184}\text{Hg}$ atoms were flushed into the COMPACT detector array.

determining 50% of the fully integrated rate under the curve. For the results and discussions of the offline as well as online experiments, the t_{50} values were compared.

3.3.2 Overall chemical efficiency

In order to determine the chemical efficiency, the rate of Hg and Pb isotopes coming into the RTC were initially determined. This rate (referred to as 100%) was measured with the FPD. In the experiment T039, the FPD was installed without RTC window and supporting grid. Due to increase of uncertainty in the calculation of the chemical efficiency by assuming the loss of counts due to the RTC window and supporting grid, the 100% measurement in T041 was performed behind window and grid. To determine the rate of Hg and Pb isotopes being flushed into the COMPACT detector array and detected there, the RTC and COMPACT detector arrays were installed instead of the FPD.

For the analysis only data collected during beam pause periods were evaluated, due to the interference of signals from implanted recoils with the ones from α -particles into the FPD. The rate of events originating from the decay of Hg and Pb isotopes, both in the FPD as also in the COMPACT detector arrays, was integrated in certain energy ranges. The energy ranges, as well as the number of counts and projectile doses for both experiments are given in Tab. 3.3. Additionally, the total number of counts were divided by the projectile dose resulting in the normalized counts, which are also given in Tab. 3.3. The normalized counts for the COMPACT detector and FPD were corrected by their efficiencies to detect α -particles, 76% and 55%, respectively. The overall chemical efficiency was obtained by the ratio of the corrected COMPACT rate, to the corrected FPD rate. The calculated overall chemical yields will be given in the results section 3.4.

Table 3.3: Important parameters for the chemical yield determination of short-lived isotopes of Hg and Pb for the experiments T039, and T041. The uncertainty for the projectile doses was calculated with 10% [65]. The total amount of counts were determined in specific energy ranges given in the table.

	T039 (2014)		T041 (2015)	
	Hg	Pb	Hg	Pb
Energy range [MeV]	3.0-6.1	6.3-6.5	4.8-6.12	5.5-6.5
FPD				
Projectile dose	$3.9 (4) \cdot 10^{13}$	$9.6 (9) \cdot 10^{13}$	$2.6 (3) \cdot 10^{14}$	$7.1 (7) \cdot 10^{14}$
Counts	43391 (208)	2996 (55)	48744 (221)	22937 (151)
Normalized counts (Counts / Projectile dose)	$1.1 (1) \cdot 10^{-9}$	$3.1 (3) \cdot 10^{-11}$	$1.9 (2) \cdot 10^{-10}$	$3.2 (3) \cdot 10^{-11}$
COMPACT	Au surface	SiO₂ surface	Au surface	SiO₂ surface
Projectile dose	$2.2 (2) \cdot 10^{14}$	$2.2 (2) \cdot 10^{14}$	$2.5 (3) \cdot 10^{14}$	$5.7 (6) \cdot 10^{14}$
Counts	26451 (163)	641 (25)	41403 (203)	6768 (82)
Normalized counts (Counts / Projectile dose)	$1.2 (1) \cdot 10^{-10}$	$2.9 (1) \cdot 10^{-12}$	$1.7 (2) \cdot 10^{-10}$	$1.2 (1) \cdot 10^{-11}$

3.4 Results

As already mentioned in the experimental section for the offline experiments, ^{219}Rn was sprayed into the RTC by an injection valve installed in a back panel on the opposite side of the RTC outlet. Different spraying angles, central and lateral were tested, but since no substantial difference in the average transport time could be determined, the results shown in this section are solely from the central injection position.

In order to show the influence of the composition of the carrier gas mixture on the transport time, offline tests with RTC depths of 20 and 30 mm were performed. Measurements with 100% Ar gas and a gas mixture of 70% He and 30% Ar gas were conducted. The gas pressure as well as the gas flow rate were kept constant at around 1.3 bar and 3.0 L/min respectively. The results of the measurements are shown in Fig. 3.8.

It can be clearly seen that with the usage of He gas in the carrier gas mixture, the values for t_{50} decreased independently from the RTC depth. Furthermore, the measurements indicated a connection between the RTC depth and the average transport time independent of the carrier gas mixture. The larger the RTC depth, the larger the t_{50} value. This indicated dependency was confirmed, in further offline experiments shown in Fig. 3.9. Here, the t_{50} values were determined for different RTC depths at gas flow rates varying between 1.0, 1.5, and 2.0 L/min. A 30% He and 70% Ar gas mixture was used, at a gas pressure of about 1 bar. Aside from the dependence on the RTC depth and average transport time, the measurements showed that with increasing gas flow rate the transport time decreased.

The average transport times determined in the online experiments T039 and T041 are also shown in Fig. 3.9. The measurement of T039 was performed with an RTC depth of 37 mm, a carrier gas mixture of 70% He and 30% Ar, gas flow rate of 1.5 L/min and a gas pressure of about 1.3 bar. As described in

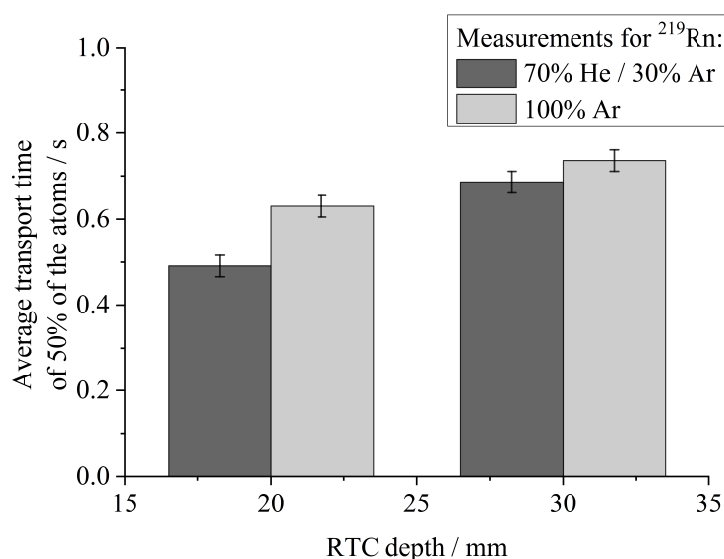


Figure 3.8: Offline transport time measurements, showing the influence of different carrier gas mixtures on the average transport time in which 50% of the atoms are transported from RTC to the COMPACT detector array. The measurements were performed with pure Ar gas (light grey bars), and a mixture of 70% He and 30% Ar (dark grey bars), with RTC depths of 20 and 30 mm, and a gas flow rate of 3.0 L/min as well as a gas pressure of 1.3 bar.

section 3.2, the transport capillaries between the RTC outlet and COMPACT detector arrays were similar to the capillary lengths in the offline measurements with 30 to 40 cm (\varnothing_i 2 mm). A t_{50} value for $^{182-184}\text{Hg}$ of 1.3 ± 0.05 s was determined. As described in section 3.2 the measurement in T041, was performed with an optimized experimental setup in which the RTC shown in Fig. 3.3 was used, at a depth of 2 cm. Furthermore, the transport capillaries were shortened to 5 cm (\varnothing_i 3 mm), and the gas flow rate was increased to 2.0 L/min. The gas pressure was about 1 bar and the carrier gas mixture was 30% He and 70% Ar. The optimizations resulted in a decrease of the t_{50} value for $^{182-184}\text{Hg}$ to 0.3 ± 0.03 s.

The overall chemical efficiencies were determined with the short-lived isotopes of Hg and Pb in the online experiments T039 and T041, with the same experimental conditions as used for the transport time measurements. The results are tabulated in Tab. 3.4. For comparison reasons, the transport time and chemical yield determined in the first FI experiment at TASCA (T021) are given as well in the table. The values for T021 are taken from Ref. [56].

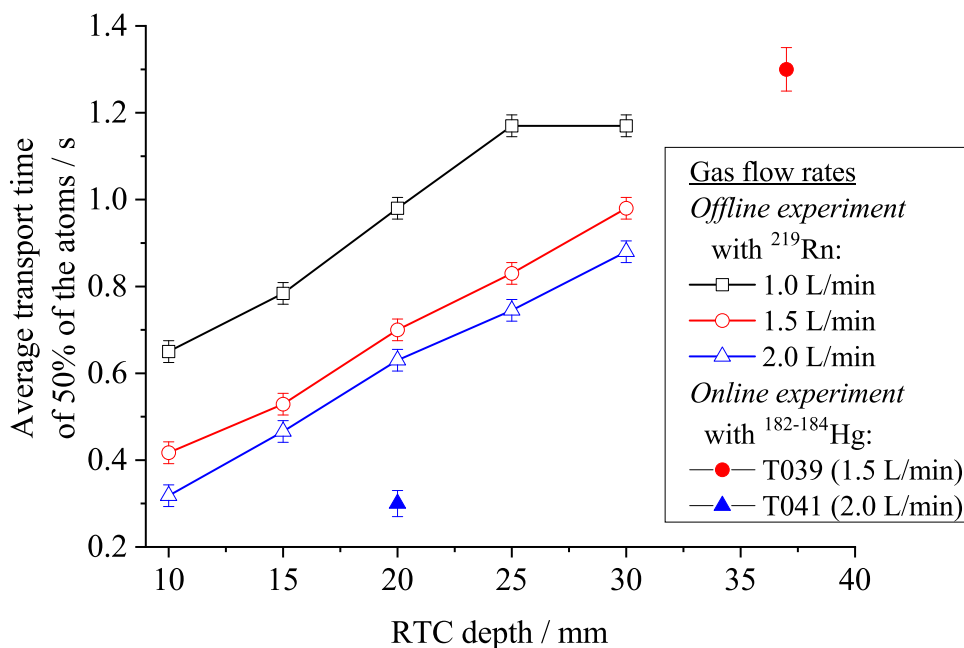


Figure 3.9: Offline as well as online transport time measurements, showing the influence of RTC depth with different gas flow rates on the average transport time (t_{50}). The data points, connected with lines and empty symbols show the results of the offline experiments, which were measured in gas pressure of about 1 bar. The two data points illustrated with filled symbols are the average transport times, determined from the online experiments T039 (2014) and T041 (2015).

Table 3.4: Comparison of the average transportation time (t_{50}), as also the overall chemical efficiencies determined in the online experiments T039, T041, as also from the first FI chemistry experiment at TASCA (T021). The values for T021 are taken from Ref. [56].

Experiment	Transport time (t_{50}) [s]	Overall chemical efficiency [%]	
		$^{182-184}\text{Hg}$	$^{185,186}\text{Pb}$
T021 (2009)	0.81 ± 0.06	27	20
T039 (2014)	1.30 ± 0.05	16 ± 3	7 ± 22
T041 (2015)	0.30 ± 0.03	62 ± 0.5	25 ± 1

3.5 Discussion

In Fig. 3.8, the results of the average transport time of ^{219}Rn in 100% Ar gas at 20 mm and 30 mm RTC depth were compared to measurements with 70% He and 30% Ar carrier gas mixture. It could be seen that in the measurements with an RTC depth of 30 mm, the t_{50} value for the measurements with the He/Ar carrier gas mixture was slightly shorter ($\Delta t_{50} = 0.05 \pm 0.05$ s), then in pure Ar gas. This difference can be explained by the diffusion process of the ^{219}Rn atoms in the carrier gas. The diffusion reflects the process

of particles / atoms moving from an area of higher concentration to an area of lower concentration. The rate of the movement is a function of the temperature, carrier gas pressure, density of the particles / atoms and carrier gas, and their molecular masses. This is quantified by the diffusion coefficient $D_{1,2}$ [55], which was given in subsection 1.4.2, equation 1.10.

The diffusion coefficients were calculated for ^{219}Rn diffusing into He/Ar, as well as in pure Ar at a temperature of 21°C and at a carrier gas pressure of 1.3 bar. This resulted in $D_{1,2}(\text{He/Ar})=3.3\cdot 10^{-3} \text{ cm}^2/\text{s}$ and $D_{1,2}(\text{Ar})=2.9\cdot 10^{-3} \text{ cm}^2/\text{s}$, respectively. These results supported the statement already made in subsection 3.1.3 that the diffusion in He/Ar carrier gas mixture was faster than in pure Ar gas, and it resulted in a shorter t_{50} value. Due to the smaller RTC depth in the measurements with 20 mm, the t_{50} value for both carrier gases was shorter in comparison to the measurements with 30 mm RTC depth. The smaller RTC depth in combination with the faster diffusion in He/Ar and a gas flow rate of 3.0 L/min, caused an increase in the difference between the measurement of 70% He / 30% Ar and 100% Ar to $\Delta t_{50}=0.14\pm 0.05 \text{ s}$ (as shown in Fig. 3.8).

A linear correlation between the RTC depth and the average transport time was seen in the offline measurements shown in Fig. 3.9. Comparing the measurements with different gas flow rates with each other, it was seen that with increasing gas flow rate the average transport time decreased. Remarkably is the difference in t_{50} value between the measurements of 1.0 and 1.5 L/min which was somewhat higher ($\Delta t_{50}=0.26\pm 0.05 \text{ s}$), than for the measurements between 1.5 and 2.0 L/min ($\Delta t_{50}=0.08\pm 0.05 \text{ s}$). This can be explained by the exponential dependence of the transport time on the gas flow rate. The dependency of the gas flow rate on the t_{50} value at constant RTC depths is shown in Fig. 3.10. The results obtained here confirm the larger difference for the measurements with increasing flow from 1.0 to 1.5 L/min and from 1.5 to 2.0 L/min.

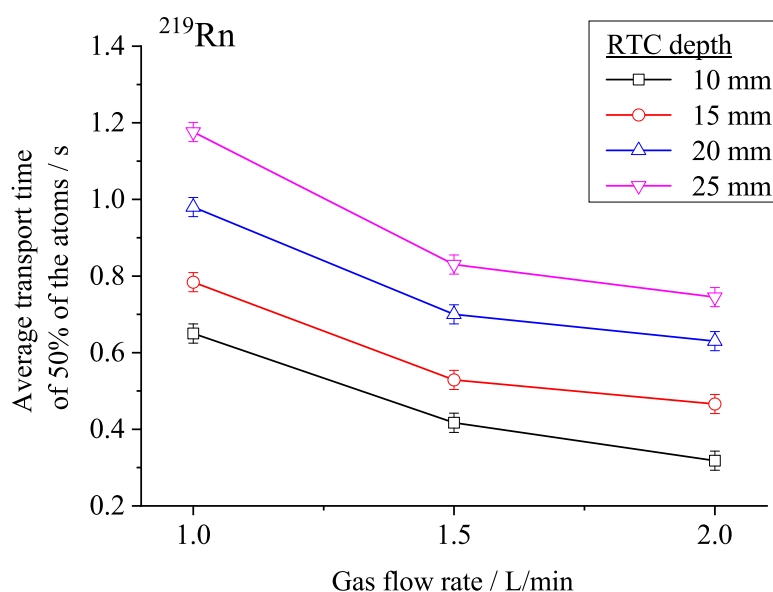


Figure 3.10: Offline transport time measurements, showing the dependency of the average transport time on the gas flow rate of the carrier gas flushing the atoms from the RTC to the COMPACT detector array at constant RTC depths. The measurements were done at a gas pressure of about 1 bar.

To conclude, the offline measurements confirmed the below itemized expected behavior:

- The diffusion in a carrier gas mixture with He content was faster than in 100% Ar gas, and resulted in shorter t_{50} values.
- The smaller the RTC depth was chosen, the shorter the t_{50} values.
- With increasing the gas flow rate of the carrier gas, the t_{50} values decreased.

With the help of the offline experiments, a guideline was set to optimize the experimental setup and parameters to reduce the average transport time also for the online experiments. Nevertheless, the optimal conditions of the offline experiments to the online experiments could not be fully transferred due to several reasons. As already explained in section 3.2, and illustrated in Fig. 3.6, the experimental conditions of the atoms entering the RTC were not the same for offline and online experiments. In the offline experiments, the ^{219}Rn atoms were sprayed into the RTC Volume in one spot, so that the diffusion speed of the atoms in the carrier gas was a crucial factor for the transport time. For the online experiments this was not the case, since the atoms entering the RTC were distributed more homogeneously and were not injected into the RTC in one spot. For the online experiments, the collisions of the EVRs with the carrier gas molecules leading to thermalization of the EVRs was more of importance. To avoid losses due to implantations into the walls of the RTC and at the same time have a short t_{50} value, the ratio of He and Ar carrier gas had to be chosen i) to fully thermalize the EVRs ii) keep the α -decay energy resolution in the spectra high, and iii) to use a minimal RTC depth. The offline results showed that the higher the gas flow rate, the shorter the average transport time. For the online experiments we were limited in the gas flow rate, since the velocity of the gas in the transport capillaries would become too high, and the diffusion towards the walls of the transport capillaries would be too fast. This would negatively effect the transportation of the EVRs. Furthermore, the chemical separation in the detector column would be negatively affected with increasing gas flow rate. The gas pressure in the RTC would have to be increased severely, resulting in a higher probability of the RTC window to break.

Applying this to SHE experiments, the optimal RTC depth was fixed to 20 mm, and with the help of SRIM calculations the He/Ar ratios were determined individually depending on the energies of the EVRs in order to avoid losses. The optimal gas flow rate was chosen to be 2 L/min, and gas pressure around 1 bar was set.

Two online transport time measurements were performed (T039, T041) and the results were shown in Fig. 3.9 as filled symbols. As mentioned in the results section, the experiment T039 was not performed with the above mentioned optimal settings. The mechanically adjustable RTC was erroneously set to 37 mm instead of 20 mm depth. The t_{50} value obtained for this measurement was 1.3 ± 0.05 s. Extrapolating the fit of the offline measured data points with the same gas flow rate of 1.5 L/min and same capillary lengths, showed an agreement with the online measured data point.

For the experiment T041 (2015) the RTC developed in 2015 was used, having a fixed depth of 20 mm. Furthermore, in comparison to the T039 and the offline measurements, the connections were shortened to 5 cm and the gas flow rate was kept fixed at 2.0 L/min. By using these parameters, the t_{50} -transport time for $^{182-184}\text{Hg}$ in comparison to T021 could be decreased by more than half, to 0.3 ± 0.03 s. The same

can be seen, when comparing to the offline measured t_{50} value for the same gas flow rate and RTC depth, cf. Fig. 3.9. This can be explained on the one hand by the longer PTFE connection tubes in the offline experiments between RTC outlet and COMPACT detector arrays. On the other hand the difference in spacial distribution of the atoms in the RTC in the online and offline experiments, as shown in Fig. 3.6, played an important role. Due to the homogeneous distribution of the atoms in the online experiments, they were flushed out of the RTC more quickly together with the carrier gas.

As mentioned earlier, the transport time is closely connected to the overall chemical efficiency. In Tab. 3.4 an overview on the obtained overall chemical efficiencies and t_{50} values for the experiments T039 and T041 were given, in comparison to T021. Comparing the values of T021 and T041 with each other, we could clearly see that the overall chemical efficiency for Hg was increased more than twice. This can be explained by the technical optimizations which were performed, which also reduced the average transport time substantially. In addition, the measurement technique with the FPD to perform the 100% measurements was optimized in comparison to former experiments. By measuring with the FPD behind the RTC window, the comparison between the measurements of the FPD and RTC / Chemistry detector arrays became more accurate. With these new optimizations, the chemical yield of the less volatile metal Pb could also be increased slightly. The lower yield can be explained by the adsorption losses on the walls of the RTC and transport tubes, due to Pb's high reactivity.

To summarize, all technical optimizations led to a successful decrease of the transport time from 0.8 ± 0.06 s (T021, [56]) to 0.3 ± 0.03 s (T041) and to an increase of the total chemical efficiency from 27% (T021) to $62 \pm 0.5\%$ for volatile elements. The optimized setup was later successfully used for chemical investigations on FI, which will be described in chapter 6.

Chapter 4

Chemical adsorption studies of Hg, Tl, and Pb on SiO₂ and Au surfaces

As discussed in chapter 3, the COMPACT detection system was optimized to chemically separate elements with different volatilities and reactivities from each other. For better chemical understanding of Cn, Fl and future studies on Nh, it was essential to study and compare the chemical behavior of their lighter homologs Hg, Tl, and Pb in the exact same experimental setup and under the same experimental conditions.

The results of theoretical calculations which were shown in Fig. 1.12, predicted distinct interaction strengths of Hg, Tl, and Pb with SiO₂ and Au surfaces. By using SiO₂ and Au-covered COMPACT detector arrays in series, a chemical separation of the volatile metal (Hg) from the non volatile metals (Pb, Tl) was anticipated. Short-lived Tl isotopes were studied for the first time in online gas-phase chemistry experiments.

4.1 Previous experimental results of studies on Hg, Tl, and Pb

Prior to the online investigations of Hg, Pb, and Tl in the COMPACT detector arrays, several offline adsorption studies with isotopes of Tl and Pb on SiO₂ and Au surfaces were performed by groups at PSI and FLNR [110–112]. The same groups also performed offline and online experiments on Hg adsorption on the two surfaces [84, 113].

The results of the experiments showed that Hg was adsorbed only weakly on SiO₂ but interacted strongly with the Au surface at room temperature (21°C). On the contrary, Tl and Pb interacted strongly with both surfaces, and were adsorbed on both of them at room temperature. These results were in accordance to the theoretical predictions shown in section 1.5.2. In the Tl studies, it was observed that the chemical form of Tl was extremely sensitive to trace amounts of oxygen and water. Even the hydroxyl groups located on the SiO₂ surface were observed to oxidize Tl to TlOH [111]. On the Au surface two Tl species were observed and were interpreted to be atomic Tl and TlOH. The first successful online isothermal vacuum chromatography experiment on the interaction of Tl with SiO₂ was reported in Ref. [114] and was in modest agreement with results from the offline experiments. The adsorption enthalpy values ($-\Delta H_{ads}$) determined in the offline and online experimental investigations are shown in Tab. 4.1, and will be used as comparison to the results obtained in this work.

Table 4.1: Experimentally determined adsorption enthalpies ($-\Delta H_{ads}$) of Hg, Tl, TlOH and Pb on SiO₂ and Au surfaces, taken from Refs. [84, 110, 111, 113, 114].

	Hg	Tl	TlOH	Pb
$-\Delta H_{ads}^{Au}$	98±3 kJ/mol [110]	270±10 kJ/mol [111]	146±3 kJ/mol [111]	234 kJ/mol [84, 113]
$-\Delta H_{ads}^{SiO_2}$	42±2 kJ/mol [110]	112±5 kJ/mol [114]	134±5 kJ/mol [111]	165±4 kJ/mol [110]

4.2 Experiments and Methods

4.2.1 Experimental setup

In Tab. 4.2 a detailed overview on the experimental parameters is listed. A beam of accelerated $^{50}\text{Ti}^{8+}$ ions was provided by the UNILAC in the energy range of 5 to 6 MeV/nucleon. Typical repetition rates were 43 to 45 Hz for Pb and Tl, respectively, and 5 Hz for Hg. In total, a projectile dose of 1.8 (0.2) $\cdot 10^{14}$ particles was collected for Hg studies, 4.4 (0.4) $\cdot 10^{15}$ for Tl, and 4.9 (0.5) $\cdot 10^{15}$ for studies with Pb. The projectiles passed through a 2.2 μm Ti backing foil before impinging a $^{140}\text{CeF}_3$ target. For the $^{141}\text{PrF}_3$ and $^{142}\text{NdF}_3$ targets, the projectiles first passed through a thin C backing foil and a 2.2 μm Ti degrader foil, before impinging the targets. All three targets were enriched to 99.98%. The target segments contained $\approx 400 \mu\text{g}/\text{cm}^2$ target material. In complete fusion reactions, $^{190}\text{Hg}^*$, $^{191}\text{Tl}^*$, and $^{192}\text{Pb}^*$ compound nuclei were formed at excitation energies of several tens of MeV. After de-excitation by evaporation of neutrons, the resulting isotopes of Hg, Pb, and Tl recoiled from the target into TASCA, which was operated in HTM.

Tab. 4.3, shows the projectile-target combinations to produce short-lived isotopes of Hg, Tl, and Pb. For each projectile-target combination the most intense production channels according to HIVAP calculations [68] are listed. The corresponding HIVAP graphs are shown in the Appendix A.3-A.8. In addition, decay modes of primary products and the relative α -decay probabilities (B_α) and most intense α lines (E_α) are included. The information presented in Tab. 4.3 is of importance for the analysis of the measured α spectra and distribution patterns, which are required for the interpretation of the chemical behavior of Hg, Tl, and Pb on the SiO₂ and Au surfaces.

The Hg, Tl, and Pb ions were guided through TASCA to the focal plane of the separator. They then penetrated a Mylar vacuum window (140x40 mm² width for Hg and 40x30 mm² width for Tl and Pb) of 6 μm thickness and entered the RTC. Inside the RTC, Hg, Tl, and Pb isotopes were thermalized in pure Ar gas, and flushed with a flow rate of 1.7 to 2.2 L/min into the COMPACT detector arrays. The gas circulated in a gas loop as shown in section 2.3.

For the investigations on Hg isotopes, a HTM-RTC (56 cm³) was used. At first, Hg isotopes were flushed from the RTC through a 20-cm long PTFE tube (\varnothing_i 1 mm) into the first of two COMPACT detector arrays. As the experiment progressed the connection between RTC and COMPACT I was exchanged by a 4 to 5 cm-long PTFE tube (\varnothing_i 4 mm). For Tl and Pb a SIM-RTC (29 cm³) was used, which allowed a shorter connection tube between the RTC and the COMPACT detector arrays (2 to 3 cm-long \varnothing_i 4 mm).

Two COMPACT detector arrays were operated in series. The PIN diodes of COMPACT I were covered

Table 4.2: Detailed overview on the experimental parameters. Fluctuations in the pressure were about ± 20 mbar. The range of ions through the different materials was calculated with SRIM-2013 [97, 98]. The projectile dose was determined based on the data measured with a beam current transformer. The uncertainty on the projectile dose was taken to be 10% according to Ref. [65].

Beam			
Projectile	⁵⁰ Ti ⁸⁺		
Beam energy by UNILAC [MeV]	300.8		
Projectile dose	1.8(2)·10 ¹⁴	4.4(4)·10 ¹⁵	4.9(5)·10 ¹⁵
Repetition rate [Hz]	5	45	45
Target			
Composition	¹⁴⁰ CeF ₃	¹⁴¹ PrF ₃	¹⁴² NdF ₃
Thickness of metal [μg/cm ²]	411	371	384
Backing thickness [μg/cm ²]	2.2 μm (Ti)	41 (C) + 2.2 μm (Ti)	41 (C) + 2.2 μm (Ti)
Beam energy in target center [MeV]	281.2	281.5	281.4
Excitation energy of compound nuclei [MeV]	75		
TASCA			
Magnetic current Dipole [A]	414	415	415
Magnetic current Quadrupoles 1&2 [A]	370		
Magnetic rigidity Bρ of central trajectory [Tm]	1.58		
RTC & Gas system			
RTC type	HTM-RTC	SIM-RTC	SIM-RTC
RTC window thickness [μm]	6		
Carrier gas	Ar (purity: 99.999%)		
Pressure in gas system measured at PIR [mbar]	1010	1088	1084
Gas flow rate (norm. to 1 bar) [L/min]	1.7	2.2	2.2

with a SiO₂ surface, whereas the PIN diodes of COMPACT II were covered with a Au surface. Both detector arrays were operated at room temperature.

Table 4.3: ^{50}Ti induced reactions for Hg, Tl, and Pb isotopes production. The beam energy in the center of the targets was 277-284 MeV. For each projectile-target combination only the most intense decay channels according to HIVAP calculations are listed. Furthermore decay properties [96, 109] relevant for the data analysis are given.

Reaction	Evaporation channel	Primary products	σ [mb]	Decay mode	B_α [%]	E_α [MeV]	$T_{1/2}$ [s]	Decay products
$^{50}\text{Ti} + ^{140}\text{Ce}$	xn	^{182}Hg	2.50	α EC/ β^+	13.80 (2)	5.87	10.80	^{178}Pt ^{182}Au
		^{183}Hg	9.90		11.70 (20)	5.90	8.80	^{179}Pt ^{183}Au
		^{184}Hg	2.70		1.11 (6)	5.54	30.60	^{180}Pt ^{184}Au
$^{50}\text{Ti} + ^{142}\text{Nd}$	xn	^{185}Pb	0.31		≤ 100	6.41	4.10	^{181}Hg ^{185}Tl
		^{186}Pb	0.76		40.00 (8)	6.33	4.83	^{182}Hg ^{186}Tl
		^{187}Pb	0.08		9.50 (20)	6.07	18.30	^{183}Hg ^{187}Tl
$^{50}\text{Ti} + ^{142}\text{Nd}$	pxn	^{185}Tl	4.50		≤ 4.00	5.99	1.83	^{181}Au ^{185}Hg
		^{186}Tl	4.10		~ 0.006	5.76	2.90	^{182}Au ^{186}Hg
$^{50}\text{Ti} + ^{142}\text{Nd}$	α xn	^{181}Hg	0.01		36.00 (4)	6.00	3.60	^{177}Pt ^{181}Au
		^{182}Hg	0.50		13.80 (2)	5.87	10.80	^{178}Pt ^{182}Au
		^{183}Hg	2.00	11.70 (20)	5.90	8.80	^{179}Pt ^{183}Au	
		^{184}Hg	0.80	1.11 (6)	5.54	30.60	^{180}Pt ^{184}Au	
		^{185}Hg	3.60	6.00 (1)	5.65	49.10	^{181}Pt ^{185}Au	
$^{50}\text{Ti} + ^{141}\text{Pr}$	xn	^{183}Tl	0.30	≤ 0.01	6.34	6.90	^{179}Au ^{183}Hg	
		^{184}Tl	2.80	2.10 (7)	6.16	11.00	^{180}Au ^{184}Hg	
		^{185}Tl	1.60	≤ 4.0	5.99	19.50	^{181}Au ^{185}Hg	
$^{50}\text{Ti} + ^{141}\text{Pr}$	pxn	^{183}Hg	2.30	11.70 (2)	5.90	8.80	^{179}Pt ^{183}Au	
		^{184}Hg	11.30	1.11 (6)	5.54	30.60	^{180}Pt ^{184}Au	
		^{185}Hg	3.70	6.00 (1)	5.65	49.10	^{181}Pt ^{185}Au	

4.2.2 Monte Carlo Simulation parameters

In order to interpret the adsorption behavior of the Hg, Tl, and Pb isotopes on the different surfaces, their deposition distribution in the gas chromatography channel was determined. The experimentally observed distribution patterns were compared with the distribution patterns obtained by the Monte Carlo Simulation (MCS), explained in subsection 1.4.2, for the given species under the experimental conditions. The best agreement between the experimental and simulated distribution gave the most probable value for the adsorption enthalpy $-\Delta H_{ads}$. The parameter values used for the coefficients f_0 , f_1 , and f_2 were dependent on the width to height ratios of the chromatography column. For the COMPACT detector system the

width to height ratio was calculated to be 16 and the values $f_0=7.3$, $f_1=31.05$, $f_2=47.94$ were used, which corresponds to the mean value between two and four detection walls given by Poppe [54]. They were determined to fit the experimental data best. The source code for the MCS is given in appendix A.2.1.

4.2.3 Background reduction

In Fig. 4.1, the α -decay energy spectrum of the background measurement in COMPACT I and COMPACT II, together with its distribution in each detector pair is shown. The energy spectrum was permanently monitored with a minor ²¹⁹Rn activity and its daughters emanating from a ²²⁷Ac source. In addition, a small contamination of the non-volatile ²²⁷Ac daughters, ²²³Ra and ²¹¹Bi was detected. This caused a higher background in the third and following PIN diodes of COMPACT I, as shown in Fig. 4.1b). Due to this, a background subtraction was applied to the spectra collected during irradiation periods in all detector pairs. This was of particular importance for the measurement of ^{185,186}Pb due to the overlap of their α -decay energies with those of ²¹¹Bi.

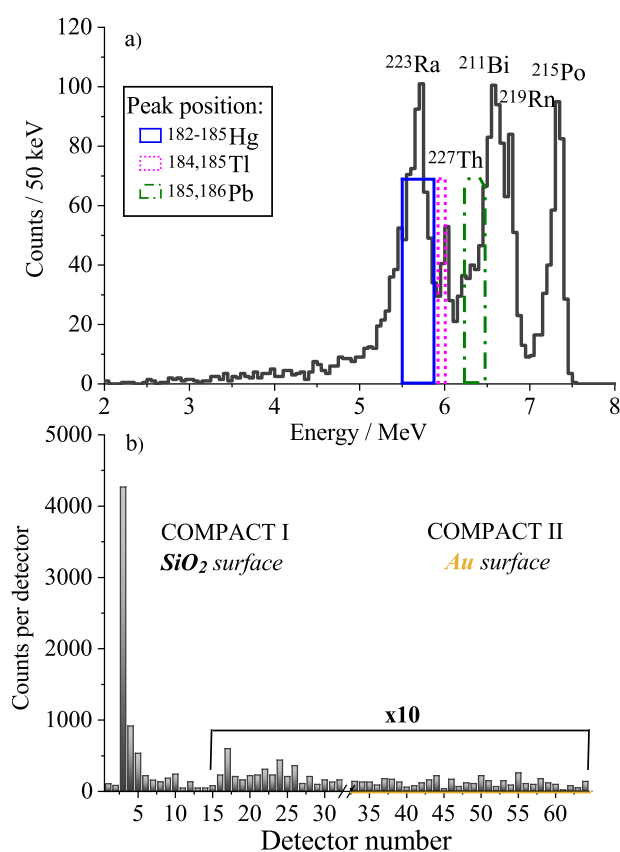


Figure 4.1: The background α -decay energy spectrum of the contamination of the ²²⁷Ac daughters in the COMPACT I-and II detector array is shown in panel a). The peak positions of Hg, Tl, and Pb isotopes are indicated. In panel b), the background distribution along the COMPACT detector array in each PIN diode pair in the energy range of 2.0 to 7.5 MeV is shown. The measurements were done in 27 minutes of irradiation time in Ar gas at a flow rate of 2.2 L/min. The figure is adapted from Ref. [115].

4.3 Adsorption of Hg on SiO₂ and Au surfaces

4.3.1 Results

In Fig. 4.2a), the experimental energy sum spectrum of Hg isotopes is shown, which were produced using a ⁵⁰Ti beam on a ¹⁴⁰Ce target, and measured with the COMPACT I (SiO₂-covered) and COMPACT II (Au-covered) detector arrays. A broad single peak at 5.8 to 5.9 MeV is visible in the spectrum, originating from ^{182–184}Hg, (see Tab. 4.3).

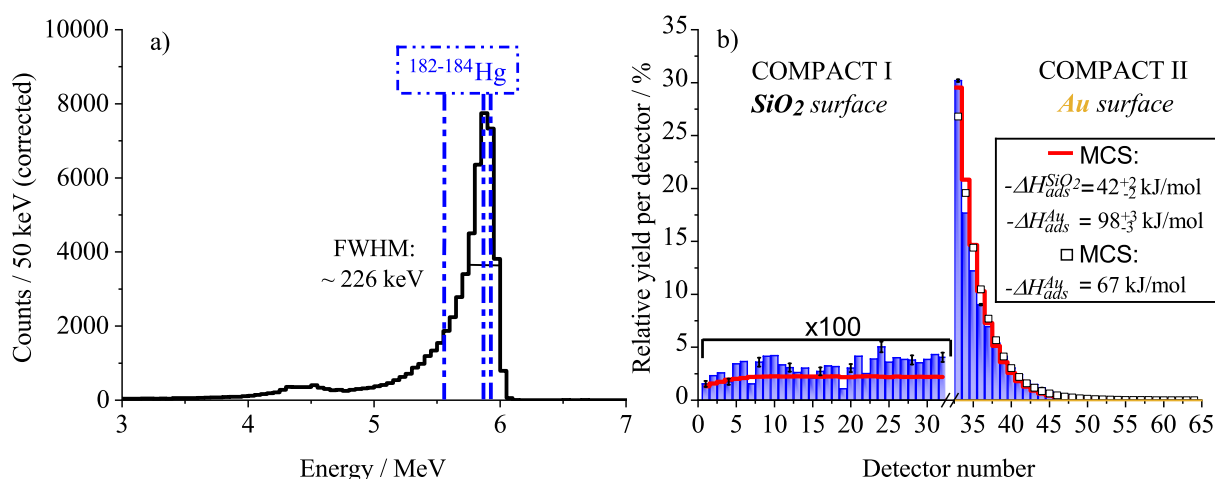


Figure 4.2: a) Sum spectrum of ^{182–184}Hg in COMPACT I+II measured in pure Ar gas during 37 minutes of irradiation time. b) Comparison of the measured ^{182–184}Hg distribution in the energy range of 5.0 to 6.4 MeV (blue bars) on SiO₂ (COMPACT I) and Au (COMPACT II) surfaces. The experimental data of COMPACT I are multiplied by factor 100 to visualize them in the graphics. Red lines show results of MCS using $-\Delta H_{ads}$ values from Ref. [110, 113]. White squares show the adsorption enthalpy limit for diffusion-controlled deposition. Statistical fluctuations of the experimental data are illustrated by error bars on every 4th detector pair. Figure is adapted from Ref. [115].

In Fig. 4.2b) the distribution pattern of Hg along the COMPACT I and II detector arrays is shown. To obtain the distribution pattern, the number of counts in the energy range of 5.0 to 6.4 MeV was integrated for each individual PIN diode pair. A small fraction of Hg isotopes was detected on the SiO₂-covered COMPACT I detector array, equally distributed along the 32 PIN diodes, whereas a much higher and exponentially-decreasing number of counts along the Au-covered COMPACT II detector array was observed.

4.3.2 Discussion

The HIVAP calculations for the ⁵⁰Ti+¹⁴⁰Ce reaction predicted the most intense decay channels to be 8, 7, 6n, corresponding to ^{182–184}Hg, (Tab. 4.3).

As already stated in subsection 4.3.1, a broad peak consisting of ^{182,183}Hg decays was clearly visible at 5.8 to 5.9 MeV in Fig. 4.2a), but no clear peak from ¹⁸⁴Hg was observed. This can be explained due to the small α -decay branch of ¹⁸⁴Hg (Tab. 4.3), as well as by the energy resolution in the COMPACT detectors

in Ar gas. Due to the FWHM of ≈ 226 keV and a long tail at the low-energy side of the peak, the α lines of $^{182-184}\text{Hg}$ were not resolved. Nevertheless, a small contribution of ^{184}Hg could not be excluded in the distribution over the entire energy area.

The distribution pattern of $^{182-184}\text{Hg}$ along the COMPACT I and II detector array, shown in Fig. 4.2b), reflected the deposition of the atoms in the detector array. This was related to the adsorption strength, half-lives of the isotopes, and the ratio between the temperature- and pressure- dependent diffusion speeds of the species and carrier gas velocities. Only a small fraction of about 1% of $^{182-184}\text{Hg}$ was detected on the SiO₂-covered COMPACT I detector (see Fig. 4.2b)). The small fraction and uniform distribution along the detector array suggested that these events were caused by Hg decaying in-flight while migrating along the COMPACT I array. The MCS described in subsection 1.4.2 was used with $-\Delta H_{ads}$ values in the range of 42 to 45 kJ/mol, to determine the $-\Delta H_{ads}$ for Hg on SiO₂. Fig. 4.3 shows the $^{182-184}\text{Hg}$ distribution pattern along the detector array in comparison to the simulated distribution patterns. Statistical fluctuations of the experimental data are illustrated by the error bars on every 4th detector pair. Since the statistics of the MCS (10^7 atoms) were much higher than for the experimental data (≈ 2000 atoms), a constant distribution as a function of detector number was visible after detector pair five. The distribution pattern of the simulation showed a small increase in relative yield from detector pair 0 to 5. This can be explained by the mean jump length, which is around 3 cm in our MCS. Accordingly, fewer surface interactions occurred in the first few centimeters of the detector array. The adsorption enthalpy value for Hg on SiO₂ fitting the experimental data best, was determined as $-\Delta H_{ads}^{\text{SiO}_2}(\text{Hg})=43\pm 1$ kJ/mol (95% c.i.) and was in agreement with the data $-\Delta H_{ads}^{\text{SiO}_2}(\text{Hg})=42\pm 2$ kJ/mol taken from Ref. [110]. The simulated distribution for the literature value is also shown in Fig. 4.2b).

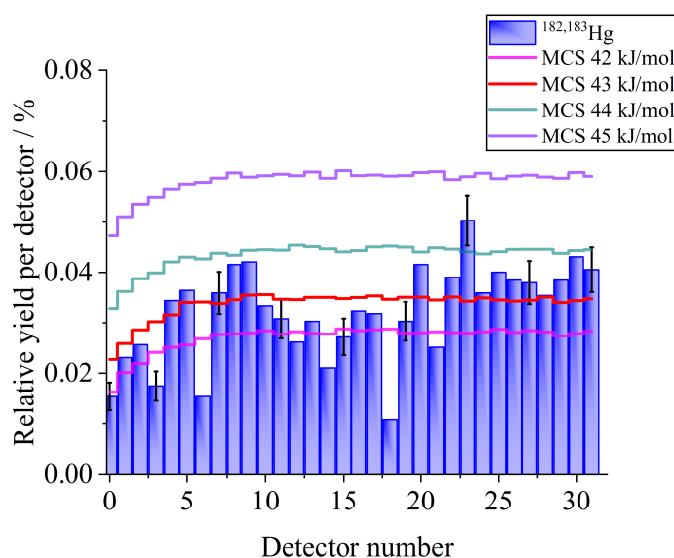


Figure 4.3: Measured $^{182-184}\text{Hg}$ distribution along the SiO₂-covered COMPACT array, in comparison to calculated distributions by MCS with different $-\Delta H_{ads}$.

In contrast, a much higher and exponentially decreasing rate along the Au-covered COMPACT II detector array was observed. The observed distribution of $^{182-184}\text{Hg}$ in COMPACT II on the Au surface pointed to the formation of metallic bonds with Au. The Hg atoms diffused towards the walls of the detector, where they were immobilized and underwent decay. As already explained in subsection 3.1.3, this deposition process inside the COMPACT detector column, occurring for strongly-interacting species, was

termed diffusion-controlled deposition. Due to this, no detailed information on the strength of the surface interaction for $-\Delta H_{ads}$ values higher than the limit for diffusion-controlled deposition could be obtained. To determine the limit for Hg on Au, the relative yield per detector, which was decreasing along the chromatography channel approaching a plateau, was fitted with a linear regression. A 95% prediction band was determined from the linear regression as shown in Fig. 4.4. The prediction band was the area which covered 95% of all our experimental data points. We simulated the distribution pattern in the detector channel with the MCS approach for different values of the adsorption enthalpy (60-98 kJ/mol) and compared these patterns to the 95% prediction band. The lowest adsorption enthalpy value corresponding to the distribution pattern lying fully inside the prediction band was determined to be the lower limit of the adsorption enthalpy for the diffusion-controlled deposition. All the simulations with $-\Delta H_{ads} \geq 67$ kJ/mol resulted in distributions that were fully contained inside the 95% prediction band, hence our result is $-\Delta H_{ads}^{Au}(\text{Hg}) \geq 67$ kJ/mol (95% c.i.).

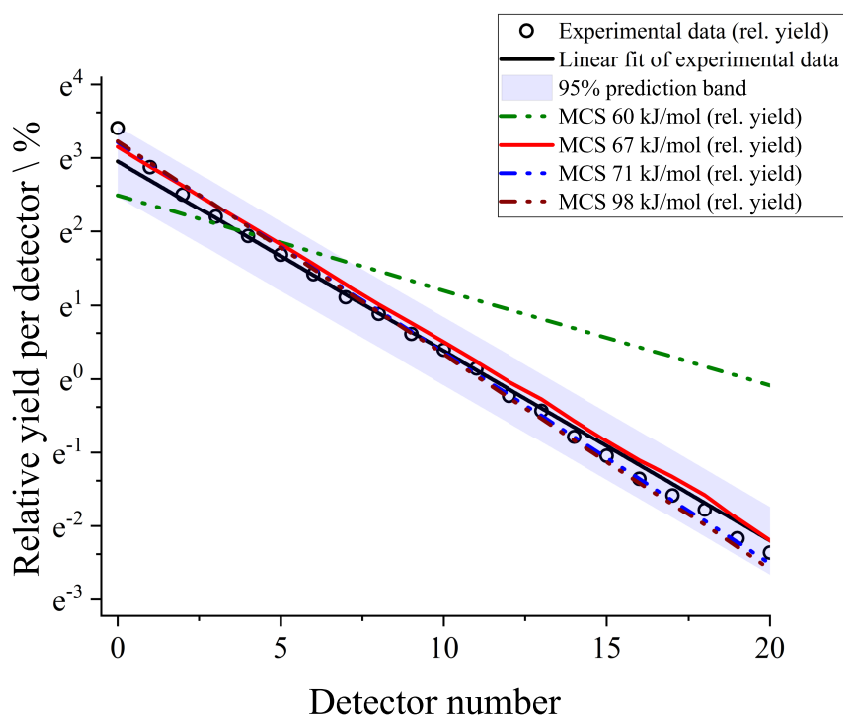


Figure 4.4: Linear regression of the experimental data for $^{182-184}\text{Hg}$ (black dots). A prediction band of 95% was determined (blue band), and compared to simulated distribution patterns for a variety of $-\Delta H_{ads}$ values.

The simulations of $-\Delta H_{ads} \geq 67$ kJ/mol exhibited similar relative yield values per detector as for 67 kJ/mol, as they were above the diffusion-controlled deposition limit. Due to this, the observed adsorption properties of Hg, as also later for Tl and Pb, were compared to $-\Delta H_{ads}$ values obtained in former experiments (see Tab. 4.1). The distribution of Hg on Au obtained via the MCS using $-\Delta H_{ads}^{Au}(\text{Hg}) = 98 \pm 3$ kJ/mol from Ref. [113] is shown in Fig. 4.2b). The simulation described our experimental observation well, and was in line with the determined limit for $-\Delta H_{ads}^{Au}(\text{Hg}) \geq 67$ kJ/mol (95% c.i.).

4.4 Adsorption of Pb on SiO₂ and Au surfaces

4.4.1 Results

Due to factor ten smaller production rates of Pb compared to Hg (see Tab. 4.3) the experiment was performed at a high beam intensity, i.e. with a high beam pulse repetition rate of 45 Hz of the ⁵⁰Ti⁸⁺ beam on the ¹⁴²Nd target.

In Fig. 4.5, the energy spectra measured in COMPACT I and COMPACT II are shown. In the COMPACT I spectrum, a peak at 6.3 to 6.4 MeV can be seen, which can clearly be attributed to ^{185,186}Pb. This peak does not appear in the COMPACT II spectrum, which points to a strong adsorption of Pb on the SiO₂ surface.

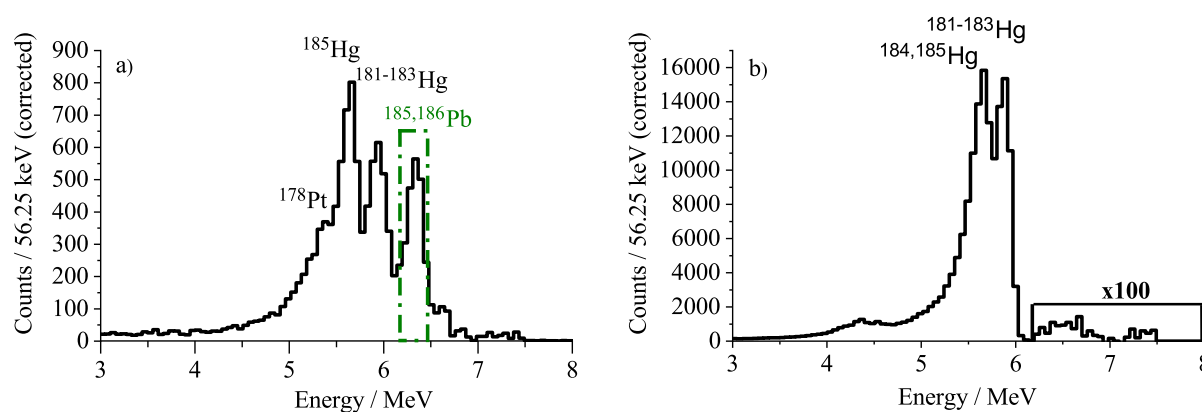


Figure 4.5: Energy sum spectra of Pb and Hg isotopes in COMPACT I (panel a) and COMPACT II (panel b), measured in Ar gas during 106 minutes of irradiation time. Figure is taken and adapted from Ref. [115].

At lower α -particle energies in the COMPACT I spectrum, two additional peaks are visible. The peak at about 5.6 MeV can be attributed to ¹⁸⁵Hg, whereas the peaks at 5.8 to 5.9 MeV can be assigned to ¹⁸¹⁻¹⁸³Hg. In the sum spectrum of the Au-covered COMPACT detector (see Fig. 4.5b)) two prominent peaks can be observed, which can both be attributed to isotopes of Hg. At an energy of 5.5 to 5.6 MeV a peak from the decay of ^{184,185}Hg can be seen. The peak at the highest energy originates from ¹⁸¹⁻¹⁸³Hg (see Tab. 4.3).

In Fig. 4.6a), the distribution pattern of ^{185,186}Pb is shown, which is exponentially decreasing along the COMPACT I detector array. The distribution of ¹⁸¹⁻¹⁸⁵Hg along the Au-covered COMPACT II detector array is shown in Fig. 4.6c), and is also exponentially decreasing.

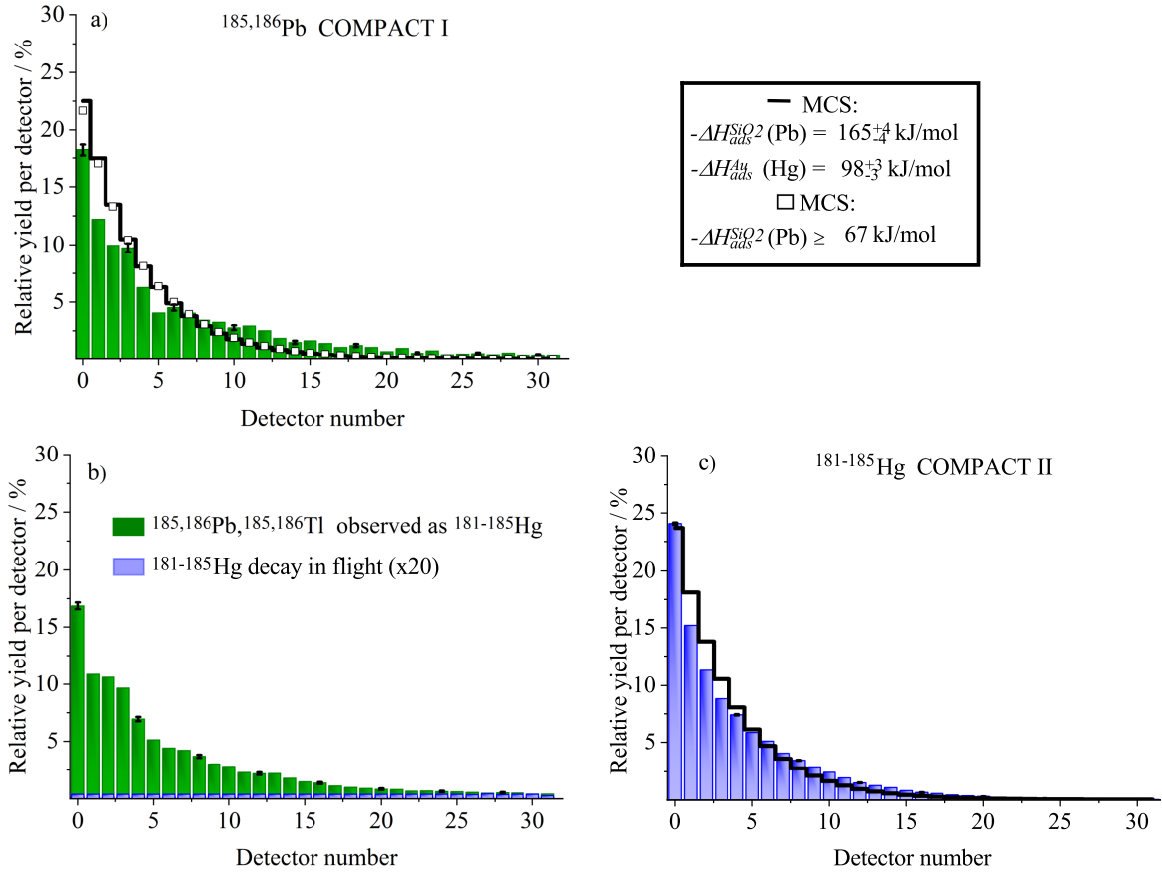


Figure 4.6: Distributions of Hg and Pb along the COMPACT detector arrays. Statistical fluctuations are indicated by error bars at every 4th detector. Panel a) shows the measured Pb distribution (6.3-6.4 MeV) and the results of the MCS using the $-\Delta H_{ads}$ value from Ref. [110], as well as the adsorption enthalpy limit of 67 kJ/mol in COMPACT I (SiO₂-covered). Panel b) (5.4-6.1 MeV) and c) (3.0-6.5 MeV), show the Hg distributions along COMPACT I (SiO₂-covered) and COMPACT II (Au-covered), respectively. Figure is adapted from Ref. [115].

4.4.2 Discussion

A variety of Pb isotopes was produced in the reaction $^{142}\text{Nd}(^{50}\text{Ti}, xn)^{192-x}\text{Pb}$. For this fusion-evaporation reaction, HIVAP calculations (see Fig. A.4) predicted large production rates for ^{185,186}Pb and a low rate for ¹⁸⁷Pb. As seen in the sum spectrum of COMPACT I (Fig. 4.5a), a clear peak of ^{185,186}Pb can be seen, but no clear peak of ¹⁸⁷Pb is visible due to its small yield in ⁵⁰Ti induced reactions. Next to the α energies of ^{185,186}Pb, additional peaks of ¹⁸¹⁻¹⁸⁵Hg are visible in COMPACT I + II in Fig. 4.5a);b). As summarized in Tab. 4.3, the reaction ⁵⁰Ti+¹⁴²Nd allowed the production of Hg isotopes in different reaction paths, i.e., either as daughters of Pb isotopes after one α -decay or after two consecutive EC/ β^+ -decays. Furthermore, Hg isotopes could be produced abundantly in charged-particle evaporation channels: either directly in αxn , or indirectly in pxn channels as EC/ β^+ -decay products of Tl isotopes.

Theoretical calculations (section 1.5.2), predicted a strong interaction of Pb atoms with the SiO₂ surface, which was also observed in an earlier experiment described in Ref. [110]. MCS using the adsorption

enthalpy of $-\Delta H_{ads}^{SiO_2}(Pb)=165\pm 4$ kJ/mol, which was given in Ref. [110], were in good agreement with the distribution pattern for ^{185,186}Pb (see Fig. 4.6a)). The exponentially decreasing distribution for Pb (like for Hg on Au) could be explained by the diffusion-controlled deposition process. The lower limit for the adsorption enthalpy determined for the deposition of Hg on Au of 67 kJ/mol (95% c.i.) could be used to model the distribution of Pb on SiO₂. As shown in Fig. 4.6a) it described the experimental data well. A wider experimental distribution of Pb on SiO₂ in comparison to Hg on Au was notable, due to the presence of unwanted background originating from the contamination described in section 4.2.3. It was not possible to remove all the background from the α spectrum, since the α lines of ²¹¹Bi and ^{185,186}Pb partially overlap. The small contribution of background appeared most pronouncedly as a tail towards high detector numbers in the Pb distribution (see Fig. 4.6a).

The adsorption behavior of directly-produced Hg isotopes on SiO₂ and Au surfaces was already discussed in section 4.3. Hg interacted only weakly with SiO₂ surfaces, and was transported to the Au-covered COMPACT II detector with a high efficiency, as shown in Fig. 4.6c). Hg isotopes, produced after the decay of Pb and Tl isotopes, could be immobilized on the SiO₂ surface, and thus exhibited a similar exponential distribution as Pb or Tl (cf. Fig. 4.6b)). If Hg atoms following β^+ or α -decay recoiled into the open gas channel, they could be transported further to the Au-covered COMPACT II detector and adsorbed there. The rate of Hg in COMPACT II was much higher than in COMPACT I (cf. Fig 4.5). This indicated that the majority of Hg adsorbed in COMPACT II (cf. Fig. 4.6b)) was probably produced directly in the αxn channel, or after α , or β^+ /EC-decays of Tl and Pb inside the RTC. The Hg distribution along COMPACT I showed a combination of both reaction paths. The exponential distribution along the first detectors of COMPACT I looked similar to the distribution of Pb (see Fig. 4.5a)), pointing to most of Hg isotopes detected on the the SiO₂ surface originating from Hg immobilized after the decay of Pb or Tl. The Hg yield did not approach zero even in the last detectors of COMPACT I. This was due to decay in flight mainly of directly produced Hg isotopes, which were transported to COMPACT II and adsorbed there.

4.5 Adsorption of Tl on SiO₂ and Au surfaces

4.5.1 Results

In Fig. 4.7a) and b) the spectra from the ¹⁴¹(⁵⁰Ti, xn) reaction used to produce Tl and measured in COMPACT I and II are shown, respectively. The spectra in COMPACT I and II show two main broad α peaks. The first peak around 5.5 MeV can be attributed to the decay of ^{184,185}Hg and the second at 5.9 MeV to ¹⁸³Hg.

In both COMPACT I and COMPACT II, two exponentially decreasing distribution patterns along the detector array in direction of the gas flow can be observed in Fig. 4.7c), and d), respectively.

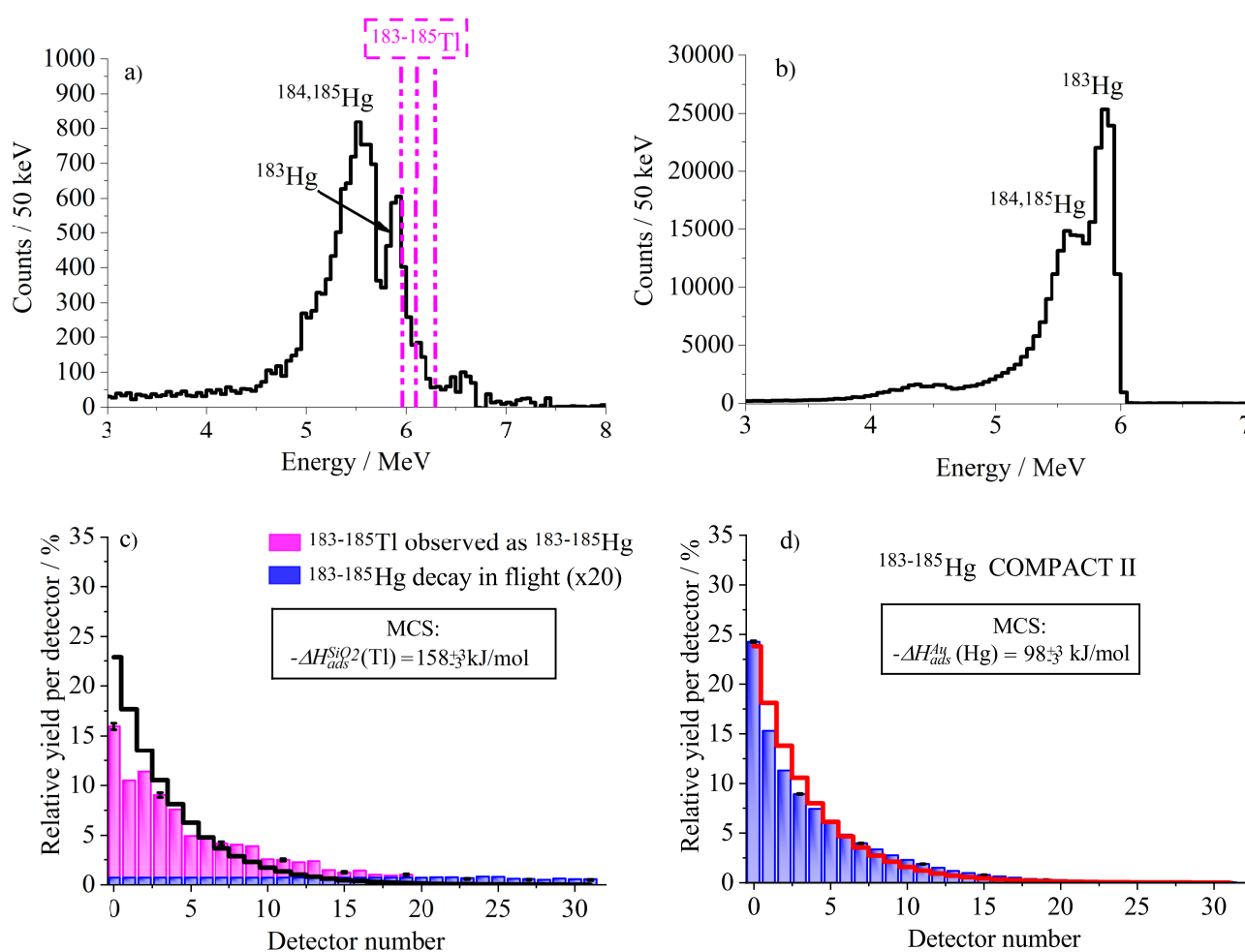


Figure 4.7: Panels a) and b) show the energy sum spectra in COMPACT I and II measured in Ar gas during 35 minutes of irradiation time. In panels c) and d) the distributions in the COMPACT detector arrays determined in the energy range 3.5 to 6.5 MeV are shown. In addition, the result of the MCS using the $-\Delta H_{ads}$ for Tl from Ref. [114] is shown. The blue bars shown in panel c), show the observed Hg decay in flight, which was determined from the total sum of Hg with the deposition of Tl subtracted. Figure is taken and adapted from Ref. [115].

4.5.2 Discussion

Short-lived Tl isotopes were produced in the reaction $^{141}\text{Pr}(^{50}\text{Ti}, xn)^{191-x}\text{Tl}$. According to results of HIVAP calculations shown in Fig. A.7, the highest production cross-sections were expected for $^{183-185}\text{Tl}$. Due to the small α -decay branches of $^{183-185}\text{Tl}$ (cf. Tab. 4.3) which rendered the detection of these isotopes via α -decay challenging, the experiment was performed with a high beam pulse repetition rate of 45 Hz. It is notable, that no peaks of the α lines of $^{183-185}\text{Tl}$ were visible in the spectra of COMPACT I and II. Solely peaks of Hg isotopes were observed (see Fig. 4.7a), and b)). In the $^{50}\text{Ti}+^{141}\text{Pr}$ reaction, Hg isotopes can be produced in two different reaction paths. They can either be produced as daughters of Tl isotopes after EC/ β^+ -decay, or directly in pxn reactions. The produced Hg isotopes have much larger α -decay branches than the Tl isotopes as shown in Tab. 4.3.

The larger rate of Hg decays in COMPACT II in comparison with COMPACT I, pointed to a substantial

production of Hg in the direct $p\alpha n$ reaction, as well as Hg produced via decay of Tl inside the RTC. Although the detected α lines in COMPACT I were clearly attributed to isotopes of Hg, the observed exponentially-decreasing distribution pattern in COMPACT I up to detector number 15 (cf. Fig. 4.7c) pointed to a much stronger interaction with the SiO₂ surface than was determined for directly-produced Hg (cf. section 4.3). This observation can only be explained with immobilized volatile Hg atoms on the SiO₂ surface after the EC/ β^+ -decay of Tl. Decay in flight of Hg was clearly visible beyond detector number 15, and Hg was transported towards the COMPACT II detector.

The observed distribution pattern in the COMPACT I array suggested that Tl adsorbed strongly on a SiO₂ surface, which was in accordance with theoretical predictions (section 1.5.2). Furthermore, it was in agreement with results from the literature, where values of $-\Delta H_{ads}^{SiO_2}(Tl)=112\pm 5$ kJ/mol [112], 158 ± 3 kJ/mol [114] and $-\Delta H_{ads}^{SiO_2}(TlOH)=134\pm 5$ kJ/mol [111] were obtained. The authors of Ref. [111] observed that Tl atoms were very sensitive to O₂ and H₂O impurities in the gas and on surfaces. The presence of these impurities led to reactions forming TlOH. Using SiO₂ as a solid phase for the interaction with Tl atoms adsorbing from the gas phase, the formation of TlOH on the surface was inferred [111]. Presumably, this was similar in the earlier work reported in [112]. Theoretical studies agreed that reactions of Tl with the SiO₂ surface were likely [73]. Our experimental results did not give a clear indication of which chemical species of Tl was observed. Based on the above discussion, MCS were performed assuming that TlOH formed on the SiO₂ surface (cf. Fig. 4.7c). Comparing these simulations with experimental results, we observed a good agreement in the COMPACT I, while the distribution pattern of Hg in COMPACT II (cf. Fig. 4.7d) showed the typical chemical behavior of diffusion-controlled deposition of Hg on Au.

Chapter 5

Adsorption on a real gold surface- Analysis of the COMPACT gold layer

To understand in detail the adsorption behavior of the SHE and their homologs on the Au surface of the COMPACT detector arrays, an extensive surface study was performed. Several techniques such as Scanning Electron Microscopy and Energy Dispersive X-ray Spectroscopy (SEM-EDX), X-ray Photoelectron Spectroscopy (XPS), X-ray Diffraction Spectroscopy (XRD), and Atomic Force Microscopy (AFM) were performed by the Target Laboratory and Material Research divisions at GSI in Darmstadt, and by the Institute of Nuclear Chemistry and Institute of Physics at the Johannes Gutenberg University in Mainz. Two Au-covered PIN diode samples were investigated, and will be referred to as TUM2015 and TUM2016. As described in section 2.4, the 30 to 50 nm Au layer was deposited by thermal evaporation on silicon diodes. For the detector TUM2015, a 10 to 15 nm chromium (Cr) layer was deposited between the Si and Au for a better adhesion of the Au. The experiments discussed in this thesis were conducted with COMPACT detector arrays having PIN diodes of the type TUM2016. The experiment described in Ref. [56], which is included in the discussion of chapter 6, was performed with COMPACT detector arrays having PIN diodes of the type TUM2015. With the help of these measurements, it was possible to chemically characterize the Au surface.

In the following section, a short overview will be given on the working principle of the different analytical methods. For comparison, the results of previous analytical studies on Au surfaces will be presented in section 5.2 and the results of the Au layer measurements of the COMPACT detector samples will be presented in section 5.3.

5.1 Analytical Methods

5.1.1 Scanning Electron Microscopy and Energy Dispersive X-ray spectroscopy (SEM-EDX)

The Scanning Electron Microscopy and Energy Dispersive X-ray spectroscopy (SEM-EDX) is a combined analytical method used for qualitative and quantitative analysis. With the help of this method, it is possible to determine the type of elements and their concentrations in the sample [116].

An electron beam is focused into the sample and transfers a part of its energy to the electrons of the atoms in the sample. With this energy, the electrons can either be excited to a higher laying energy shell, or they can be ejected from the atom. If such a transition occurs, it leaves a hole behind which can be filled by an electron from a higher shell. The energy difference from the electron transition from a higher to a lower shell, can be released in the form of characteristic X-rays. The energy of the photons of the X-rays are detected with Si(Li) detectors, which are placed at an angle very close to the sample. Each X-ray has an energy which is characteristic for an element. Like this, the X-rays are a fingerprint of each element and can be used to identify the type of elements that exist in the sample [116]. The measurement depth is mainly determined by two components: i) the initial energy of the electron beam, and ii) the density of the absorber material [117].

5.1.2 X-ray photoelectron spectroscopy (XPS)

X-ray photoelectron spectroscopy (XPS) is closely related to the SEM-EDX method. It is a surface characterization technique, with which elements that are present at the surface of the sample and their chemical form can be determined. It can analyze a sample to a depth of about 2 to 5 nm and is performed under ultrahigh vacuum (UHV) conditions around 10^{-9} mbar.

The sample surface is irradiated with X-rays. When a photon hits the surface, it transfers its energy to a core-level electron which is emitted from its initial energy state and ejected from the surface. This happens with a certain kinetic energy, dependent on the incident X-ray and the binding energy of the atomic orbital from which the electron originated. The photo-ejected electrons transit from the surface into the vacuum, and are collected by an electron analyzer which measures their kinetic energy. The electron energy analyzer produces then an energy spectrum of intensity (number of photo-ejected electrons versus time) versus the electron binding energy (the energy that keeps the electrons bound in the atom). Each prominent energy peak in the spectrum corresponds to a specific element and its percentage on the surface [118].

5.1.3 X-ray diffraction spectroscopy (XRD)

X-ray diffraction (XRD) is a non-destructive analytical technique to determine the precise positions and arrangements of atoms in a crystal, resulting in the information on the orientation of the crystals in the sample [119].

A crystal structure is built of layers, which are also named planes. A set of three parallel planes form the crystal lattice is used to determine the shape and structure of the unit cell and crystal lattice. The planes act as a semi-transparent mirror. A crystalline sample is placed in the path of an X-ray beam. X-rays with a wavelength similar to the distances between the planes are partially reflected such that the angle of reflection is equal to the angle of incidence. Outgoing waves reflected at different planes undergo interferences. Positive interference occurs at angels that satisfy Bragg´s Law:

$$2d\sin\theta = n\lambda \quad (5.1)$$

where d is the spacing between diffracting planes, θ is the incident angle, n is a positive integer, and λ is the wavelength of the beam.

The beam and detector are rotated through a range of angles. The positions of the reflections give information about the inter-layer spacing of atoms in the crystal structure. The interpretation of the diffraction also gives information on the orientation of a single crystal and can measure the size, shape and internal stress of small crystalline regions.

5.1.4 Atomic force microscopy (AFM)

The Atomic force microscopy (AFM) is a high resolution type of scanning probe microscopy, with demonstrated resolutions in the order of fractions of nanometers. It provides a 3D profile of the surface, from which information on the grain sizes of a sample, as well as the homogeneity and defects can be taken [120].

The 3D profile of the surface is obtained, by measuring forces between the tip of a sharp probe installed on the end of a flexible cantilever, and the surface at a very short distance (0.2-10 nm). The probe is typically made from Si_3N_4 or Si (<10 nm). The amount of force between the probe and sample is dependent on the stiffness of the cantilever and the distance between the probe and the sample surface. This force can be described by using Hooke's Law:

$$F = -k \cdot x, \quad (5.2)$$

in which F is the force, k the spring constant of the cantilever and x the cantilever deflection. Depending on the surface structure the cantilever bends and the deflection is monitored.

The motion of the probe across the surface is controlled by a feedback loop and piezoelectric scanners. The deflection of the probe is typically measured by a beam bounce method. This means, a semiconductor diode laser is bounced off the back of the cantilever onto a position sensitive photodiode detector. This detector measures the bending of the cantilever during the time, the tip is scanned over the sample, and a surface topography map is generated. The AFM can be operated in different kind of modes. For the Au sample analysis, the tapping mode was chosen, which means that the cantilever is oscillated at its resonant frequency, and the probe lightly taps on the sample surface. This principle allows a high resolution imaging of samples that are easily damaged and or loosely held to a surface [120].

5.2 Previous experimental results on studies of a Au layer

Many studies investigating Au films growing on a substrate surface by thermal evaporation showed that usually polycrystalline Au films were formed [121–123]. A small amount of well oriented crystallines (epitaxial) were observed, which were seen as smooth and continuous plateaus. If the substrate temperature during deposition was above the so called epitaxy temperature, ($\sim 450^\circ$), the amount of epitaxial plateaus increased. The grain sizes depended on the deposition rate and the film thickness [121, 124]. Smaller

deposition rates caused bigger grain sizes since the diffusion distance on the surface increased and atoms could nucleate and bind to adjacent islands forming larger grains. For larger deposition rates, the process was inverse. Typical grain sizes ranged from 20 to 80 nm. X-ray diffraction studies showed that the Au (111) crystal orientation dominated, followed by Au (222) [125]. It was established that the intensity of the peaks were directly linked to the deposition rate.

5.3 Results of the COMPACT Au layer measurements

5.3.1 Scanning Electron Microscopy and Energy dispersive X-ray spectroscopy (SEM-EDX)

The measurements were performed on the TUM2016 Pin diode, with an initial electron beam energy of about 15 keV, corresponding to a penetration depth of approximately 100 nm. Fig. 5.1 shows the measured EDX spectrum. Hereby the energy of the X-rays against the number of counts were plotted. Every element had its characteristic peaks of unique energy. The peak height allowed quantifying each element's concentration in the sample. For every peak the element name to which it was assigned is given together with the letter (K, L, or M) indicating the shell containing the inner vacancy.

The EDX spectra of the probed Au sample clearly showed that two different elements were present in the sample namely silicon (Si) and gold (Au), representing the silicon photodiode and the 50 nm Au layer covering it.

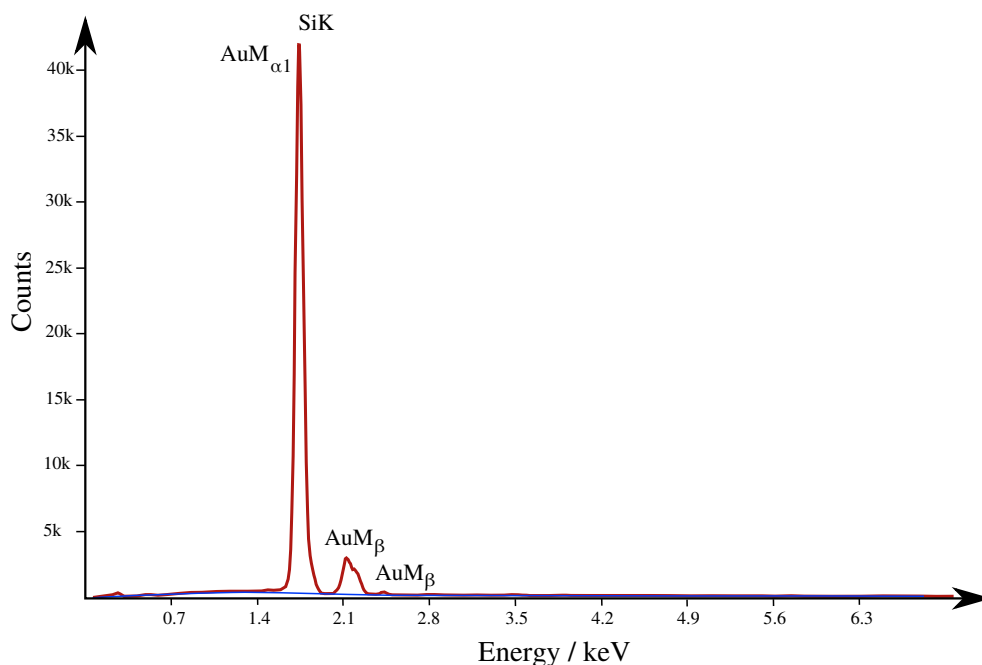


Figure 5.1: SEM-EDX spectrum of the TUM2016 Au sample. The x-axis shows the energy of the X-rays, whereas the y-axis depicts the number of counts. The description of the X-ray lines are a combination of the element symbol and a capital roman letter indicating the shell containing the inner vacancy (K, L, or M) and the electron transition (α_1 , β).

With this analytical method the sample composition could be determined, but not its purity in the first 2

to 5 nm surface layer. This is why X-ray photoelectron spectroscopy was performed. The obtained results will be discussed in the next paragraph.

5.3.2 X-ray photoelectron spectroscopy (XPS)

The XPS measurements were performed with the TUM2015 sample. The measurement depth was about 5 nm in a circular section of about 6 to 8 mm of diameter.

Fig. 5.2 shows the measured Au sample spectrum. Hereby the binding energy is plotted against the intensity of the peaks which gives information on the concentration of the elements in the first 5 nm of the surface layer.

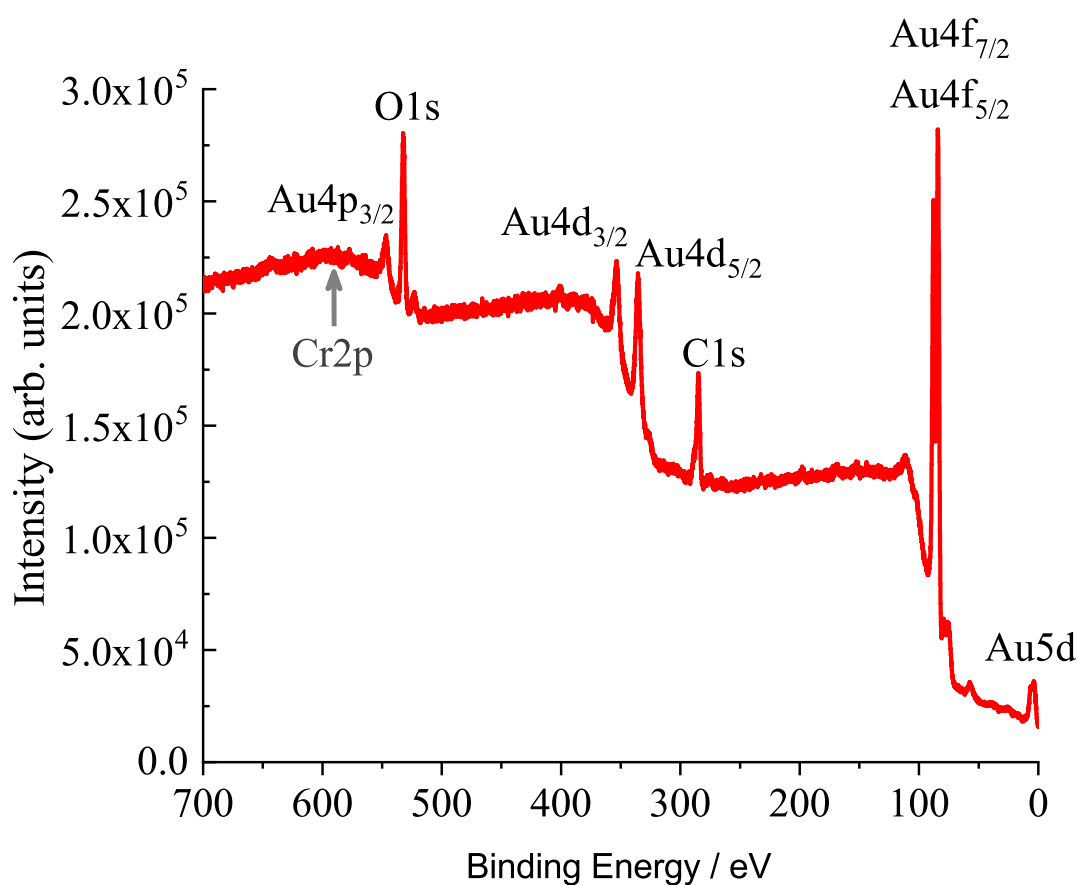


Figure 5.2: XPS spectrum of the Au sample TUM2015. The x-axis shows the binding energy in eV, whereas the y-axis depicts the intensity of the peaks. The description of the X-ray lines are a combination of the element symbol and the electronic configuration from which the electron is emitted.

It was seen, that the highest peak and most pronounced element on the surface layer was Au. Small peaks of carbon (C) and oxygen (O) were visible, indicating the presence of an organic layer. This can be explained, due to the exposition of the COMPACT detector arrays to ambient air. Furthermore some organic contamination can occur from the epoxy glue, which was used to glue the PIN diodes into the metal panel. No peak of Chromium (Cr) at a binding energy of about 580 eV was visible in the spectra, resulting in the conclusion that the first 5nm of the surface were solely Au with an organic contamination.

Additional measurements were performed after removing the surface layer by argon sputtering. After ten minutes, it was seen that the peaks of C and O disappeared and the intensity of the Au peaks increased. The organic layer was removed. After twenty minutes of sputtering, a new peak appeared at 580 eV resulting to be from Cr. The measurements confirmed, that the surface layer of the PIN diode was purely Au, and only in case of extreme experimental conditions in which the surface layer was reduced drastically, Cr was visible. Since these extreme experimental conditions were not present in the experiments presented in this thesis, it can be stated that the atoms entering the COMPACT detector arrays only interacted with the Au on the surface and no other metals.

5.3.3 X-ray diffraction spectroscopy(XRD)

The orientations of the Au crystals in the sample were measured with X-ray diffraction spectroscopy (XRD). The measured XRD spectrum of the Au sample (TUM2015) is shown by the black distribution in Fig. 5.3. The intensity is plotted as a function of the diffraction angle 2θ . The numbers above the peaks, also called miller indices, represent the corresponding lattice planes. Furthermore, a simulated XRD spectrum for polycrystalline Au is shown in red in Fig. 5.3.

In the spectrum several peaks of different crystal orientations were observed, from which the peak of the Au (111) crystal orientation dominated clearly. This observation was in accordance to the measurements reported in Ref. [125]. Comparing the simulated spectrum with the measured one, it was obvious that the measured Au(111) peak was higher and wider. This could be explained by the fact that the 50 nm Au film consisted of two components, namely polycrystalline and epitaxial Au. The enlargement of the Au(111) peak in Fig. 5.3, showed the overlapping of the two Au(111) lines. The combination of epitaxial (Epi Au(111)) and polycrystalline (Poly Au(111)) crystallites was also observed in the splitting of the line from Au (222).

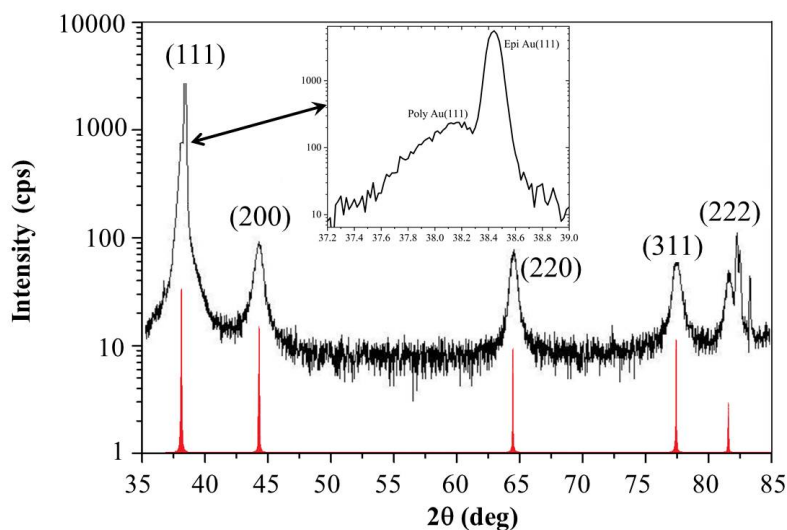


Figure 5.3: Measured XRD spectrum of the Au layer on the surface of the COMPACT detector (black) and the simulated one for polycrystalline Au (red). The numbers above the peaks represent the corresponding lattice planes. Furthermore an enlargement of the Au(111) peak is shown which shows the combination of polycrystalline and epitaxial Au(111).

The measurements of the Au sample with XRD showed the different orientations of the Au crystallites in the total sample. In order to determine the grain sizes and surface orientations, atomic force microscopy measurements were performed.

5.3.4 Atomic force microscopy (AFM)

Fig. 5.4 shows representative tapping mode Atomic force microscopy images of the Au surface of the TUM2015 sample at two different magnifications, 1000 and 200 nm respectively. Both images showed that the Au surface consisted of differently sized Au grains. The grain sizes were determined, and found to be around 50 to 100 nm for the biggest portion of the grains, which was in accordance to the measurements reported in Ref. [121, 124]. Their height was determined to be about 4 to 5 nm (5.4b). In addition some larger Au grains of about 200 nm were dispersed on the surface. In the phase contrast image in Fig. 5.4a), the different gray nuances showed a high difference of the Au grains. The Au grains of 200 nm diameter were estimated to be 20 nm taller than the smaller grain sizes. It was concluded that the large Au grains were originating from epitaxial Au crystallites, which could grow higher due to their well oriented structure.

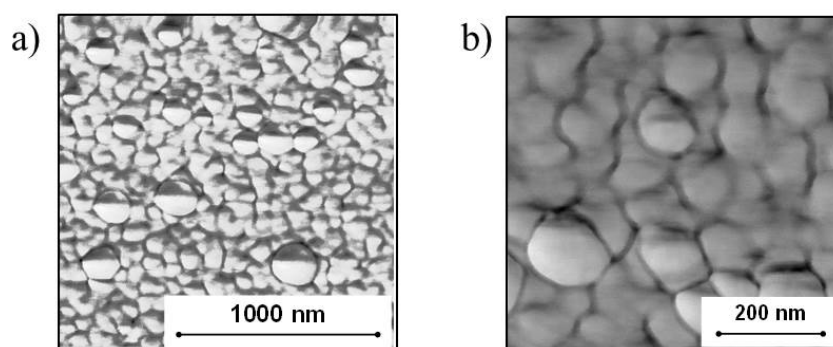


Figure 5.4: Representative tapping mode AFM images of the Au sample TUM2015. The images show two different magnifications. For more information see text.

Chapter 6

Chemical adsorption studies of Fl on SiO₂ and Au surfaces

To answer the puzzling question of whether Fl behaves more like a noble gas or like a noble metal (subsection 1.5.3), two new Fl experiments were performed at TASCA. A short 12-days campaign in 2014 (T039), and a longer 30-days run in 2015 (T041) were conducted.

Both experiments were performed after an optimization of the COMPACT detection system, in which we successfully separated the non-volatile metal Pb from the rather volatile metal Hg, by using SiO₂ and Au-covered COMPACT detector arrays. In this way it was possible to directly compare the chemical behavior of the detected Fl atoms with elements of different volatilities.

The Fl experiment T039 was performed after the first technical optimization studies which are described in chapter 3, under the same experimental name T039. The Fl experiment T041 was performed with the current optimal experimental settings which resulted in the highest overall chemical yield, and lowest transportation times, cf. chapter 3 experiment T041.

In this chapter, the new optimized Fl experiments will be described, the analysis method will be outlined, and the results discussed.

6.1 Experimental setup

An overview on the most important experimental settings used for both experiments T039 (2014) and T041 (2015) are listed in Tab. 6.1.

As described in subsection 1.5.1 the two Fl isotopes of interest, ^{288,289}Fl, were produced in the nuclear fusion evaporation reaction ⁴⁸Ca+²⁴⁴Pu. The pulsed ⁴⁸Ca¹⁰⁺ beam was accelerated by the UNILAC to an energy of 5.42 MeV/u. The ⁴⁸Ca beam was set to a 25% duty cycle, resulting in a target irradiation time of 5 ms, and a beam pause period of 15 ms. The advantage of this procedure will be explained in subsection 6.2.2. The projectiles first passed through a 2.25 μm-thick Ti backing foil, before entering the ²⁴⁴PuO₂ target. The target wheel consisted of four segments with an average thickness of 811 μg/cm² target material. Three target segments had the isotopic composition: 98.69% ²⁴⁴Pu; 0.99% ²⁴²Pu; 0.32% ²⁴⁰Pu; and 0.0013% ²³⁸Pu. The isotopic composition of the fourth segment was: 97.9% ²⁴⁴Pu; 1.3% ²⁴²Pu; and 0.7% ²⁴⁰Pu. In total a beam dose of 3.09(3)·10¹⁸ for T039, and 6.16(6)·10¹⁸ for T041 was

Table 6.1: Detailed information on the experimental parameters to determine the chemical properties of Fl at TASCA in the experiment T039 performed in 2014, and T041 performed in 2015.

Experiment	T039	T041
Beam		
Projectile	$^{48}\text{Ca}^{10+}$	
Beam energy by UNILAC [MeV]	260	
Repetition rate [Hz]	5 / 45	
Target		
Composition	$^{244}\text{PuO}_2$	
Thickness of ^{244}Pu [$\mu\text{g}/\text{cm}^2$]	811	
Ti backing thickness [μm]	2.25	
TASCA		
Ion-Optical settings	Optimized HTM	
Magnetic current Dipole [A]	687	
Magnetic current Quadrupole 1&2 [A]	619 & 570	
Magnetic rigidity $B\rho$ of central trajectory [Tm]	2.27	
RTC & Gas system		
RTC type	HTM RTC (2014) & Old HTM RTC	HTM RTC (2015)
RTC window thickness [μm]	3.3	
RTC depth [cm]	2.0	
Carrier gas	70% He / 30% Ar	50% He / 50% Ar
Pressure in gas system measured at PIR [mbar]	~ 1000	
Gas flow rate (norm. to 1 bar) [L/min]	1.5	2.0

accumulated and measured in front of the target with a transformer. In complete nuclear fusion reactions, $^{292}\text{Fl}^*$ compound nuclei were formed in an excitation energy range of 40 to 45 MeV. After de-excitation, by evaporation of three or four neutrons, the resulting $^{288,289}\text{Fl}$ nuclei recoiled from the target into TASCA. TASCA was operated for both experiments in the new optimized High Transmission Mode settings at a magnetic rigidity $B \cdot \rho = 2.27$ Tm. The $^{288,289}\text{Fl}$ ions were guided through TASCA into the focal plane of the separator. At the focal plane of TASCA, they penetrated a Mylar vacuum window (40x60 mm² area) of about 3.3 μm thickness mounted on a supporting grid, and entered the RTC. Inside the RTC, the Fl isotopes were thermalized in a He and Ar carrier gas mixture (70% He / 30% Ar in T039, and 50% He and 50% Ar in T041), and flushed with a total gas flow rate of 1.5 and 2.0 L/min respectively into the COMPACT detector arrays. The gas circulated in the optimized gas purification system described in subsection 3.1.4. A comparison of the experimental setup of the COMPACT detector arrays together with the RTC and transport tubes, is given in Fig. 6.1.

For the first part of the Fl experiment T039, the new HTM RTC developed in 2014, cf. Fig. 3.2 was used. The $^{288,289}\text{Fl}$ atoms were flushed from the RTC through a 40-cm long PTFE (\varnothing_i 2 mm) capillary into the first of three COMPACT detector arrays. The PIN diodes of COMPACT 0 were SiO₂-covered, whereas the PIN diodes of COMPACT I and II were Au-covered. The COMPACT detector arrays were operated in series. COMPACT 0 and I were operated at room temperature (21°C), whereas a negative temperature gradient down to -165°C was applied along the third COMPACT detector array. The COMPACT detectors were connected with a 30-cm long PTFE capillary (\varnothing_i 2 mm). In progress of the experiment the RTC was

exchanged by the HTM RTC shown in Fig. 2.5. This was done to reduce the PTFE transport tube length from the RTC outlet to the COMPACT detector arrays to a 5-cm long (\varnothing_i 4 mm) PTFE transport capillary.

For the experiment T041 the improved HTM RTC developed in 2015 (Fig. 3.3) was used. The ^{288,289}Fl atoms were flushed from the RTC through a 5-cm long PTFE transport tube (\varnothing_i 3 mm) into a series of two COMPACT detector arrays. The PIN diodes of both COMPACT detectors were Au-covered. The first detector was operated at room temperature, and along the second a negative temperature gradient down to -171°C was applied. Both COMPACT detectors were operated in series, and were connected with a 20-cm long PTFE capillary (\varnothing_i 2 mm).

Despite that the He/Ar gas carrier mixtures were constantly pumped through the closed gas purification loop, a thin ice layer was deposited on the Au-covered detectors below the dew point of -79°C, in both experiments.

In the results and discussion sections the SiO₂-covered COMPACT detector will be referred to as COMPACT 0, and the two Au-covered detector arrays as COMPACT I (IC) and COMPACT II (TC).

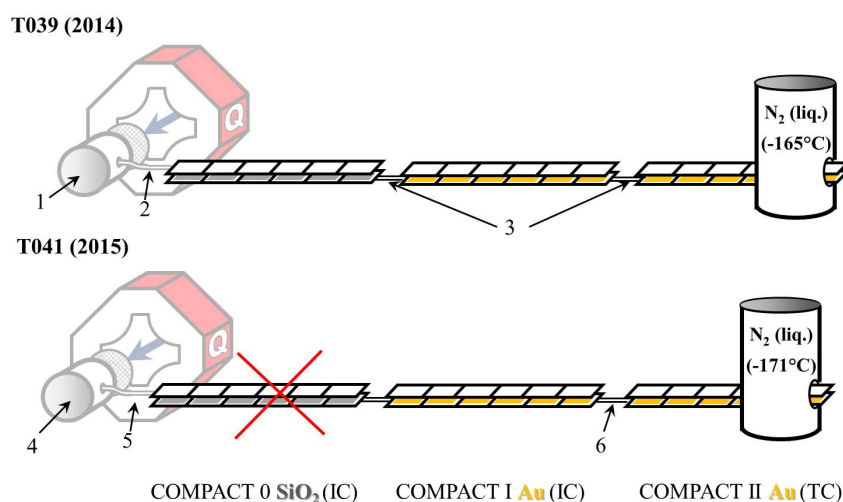


Figure 6.1: Comparison of the chemistry interface installed behind TASCA for the experimental studies on the FI isotopes in 2014 (T039) and 2015 (T041). For both experiments, TASCA was operated in optimized HTM. In the experiment T039, two HTM RTCs were used (1). See text for more details. A series of three COMPACT detector arrays was used, COMPACT 0 was SiO₂-covered and COMPACT I+II were Au-covered. COMPACT 0 and I were operated at room temperature (21°C), whereas COMPACT II was operated as TC, with a negative temperature gradient down to -165°C. The connection between the RTC and COMPACT 0 was a 40-cm long PTFE (\varnothing_i 2 mm) capillary, and later exchanged to a 5-cm long PTFE (\varnothing_i 4 mm) capillary (2). The connection between COMPACT I and II was a 30-cm long PTFE capillary (\varnothing_i 2 mm). For the FI experiment T041, the optimized HTM RTC shown in Fig. 3.3, was used (4). Only the Au-covered COMPACT detector arrays I and II were used, from which COMPACT I was operated as IC and along COMPACT II, a negative temperature gradient down to -171°C was applied. The connection between the RTC and COMPACT I detector array was a 5-cm long PTFE capillary (\varnothing_i 3 mm) (5). The PTFE connection tube between the two COMPACT detector arrays was of 20-cm length (\varnothing_i 2 mm) (6).

6.2 Results: Analysis of the experimental data

A cascade of subsequent α - and SF-decays were expected to be observed in the COMPACT detector arrays, thus special methods and parameters were used to identify the decay chains. Fig. 6.2 shows the energy spectrum in the range 5 to 12 MeV, measured in the Au-covered COMPACT I detector, obtained during the FI experiment T041 (larger statistics when compared to T039). The data shown, was taken from the sum file over all measured FI data sets in the time period of 720 hours (30 days). The spectrum in black shows all detected events collected during irradiation time or beam-on period, whereas the spectrum in red shows the detected events during the beam pause period.

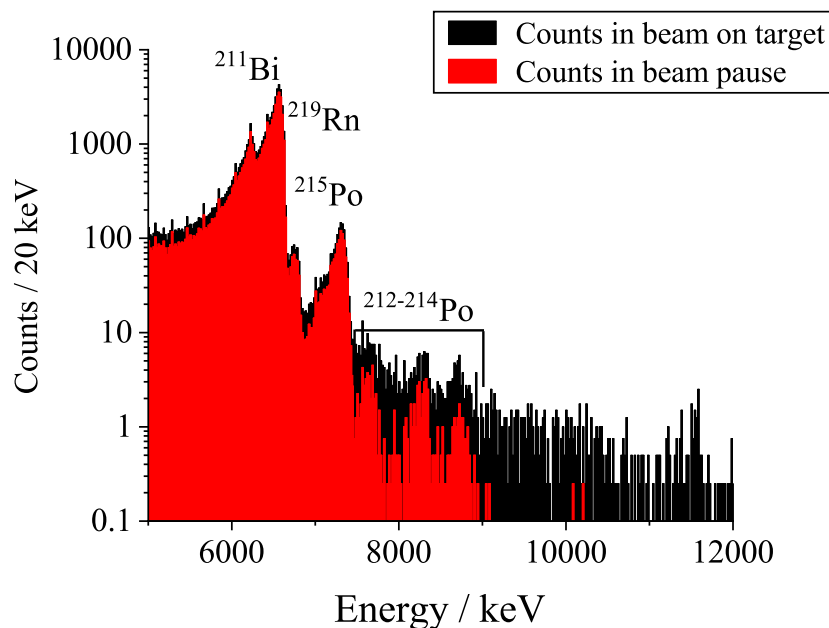


Figure 6.2: Energy sum spectrum of collected events on the Au-covered COMPACT I detector array over all measured FI data sets of T041, in the time period of 720 hours, and a beam dose of $6.16(6) \cdot 10^{18}$. The spectrum in black shows all detected events during irradiation periods of the ^{244}Pu target, whereas the red spectrum shows all events detected during the beam pause period.

The peaks visible in these spectra arose from α -decays from the chain of $^{219}\text{Rn} \rightarrow ^{215}\text{Po} \rightarrow ^{211}\text{Bi}$. Small amounts of ^{219}Rn were added to the carrier gas to allow for an online monitoring of the detection system and to provide energy calibration data. In the energy range above 7 MeV some smaller peaks were visible, which can be attributed to $^{212-214}\text{Po}$. In the energy range above 8.6 MeV, the region in which $^{288,289}\text{Fl}$ and its daughter nuclei were expected, no clear identification was possible. Due to this, a search for correlated decay chains starting from $^{288,289}\text{Fl}$ was performed on the obtained experimental data. For this, the energy, position and the time difference between detected α and SF events was used. After the detection of the first potential member of the decay chain, a time window of a defined length was opened and correlated events within this window were searched for. This correlation search procedure, called single time window, was used previously in Refs. [56, 102]. More detailed information on the used parameters are given in subsection 6.2.1. The possibility that random background of events could simulate a correlated decay sequence had to be considered carefully and will be discussed in subsections 6.2.2 and 6.2.3.

6.2.1 ^{288,289}Fl decay chain correlation search

A search for correlated decay chains starting from ^{288,289}Fl was performed. For the chain starting from ²⁸⁹Fl, an $\alpha \rightarrow \alpha \rightarrow$ SF correlation was searched for in a time window of 200 s. The α -decay of ²⁸⁹Fl was searched for in the energy range 9.6 to 10.1 MeV, whilst for the daughter ²⁸⁵Cn an energy search condition 8.8 to 9.3 MeV was applied. Finally the spontaneous fission fragments of ²⁸¹Ds were looked for in energies >20 MeV.

For the chain starting from ²⁸⁸Fl, a $\alpha \rightarrow$ SF correlation was searched for in the time frame of 1 s. Here the mother nuclei ²⁸⁸Fl were searched in the energy range of 9.6 to 10.1 MeV, and the spontaneous fission fragments of ²⁸⁴Cn in energies >20 MeV.

In the results section, it will be shown that a fully correlated decay chain was not always observed. There are two possible explanations for this. The first possible reason for incomplete decay chains was the detection efficiency of 76% for α -decays, resulting in a possibility to miss a decay. Due to the 100% efficiency for SF in COMPACT, it was highly unlikely to not detect at least one correlated SF fragment. The second reason is dependent on the transport time. If the transport time in the experimental setup was longer than the lifetimes of the Fl isotopes, they decayed on their way to the detection system. Then the highly volatile daughter nuclei Cn could be transported further along the system into the COMPACT detectors with the carrier gas, where their decay was subsequently observed.

In Fig. 6.3, an example of different possible decay positions in a Au-covered COMPACT detector array is shown for the decay chain members of ²⁸⁹Fl. The ²⁸⁹Fl atom (blue dot) was flushed together with a carrier gas mixture into the Au-covered COMPACT detector array (step 1). It interacted with the surface and its decay was observed at a certain detector pair (X) in the column (step 2). For the daughter nucleus ²⁸⁵Cn (green dot) there were two possibilities: i) it could decay in either the same or an adjacent detector pair (X-1 to X+1) (step 2.1), or ii) due to its high volatility, it could desorb back into the carrier gas and was transported by the gas flow along the detector channel (step 2.2). This means that its decay would be observed in another detector pair along the detector channel. Which of the two possibilities occurred, was dependent on the α -particle of Fl, if it was emitted into the gas phase or into the PIN diode. The SF fragments of ²⁸¹Ds were always observed in the same or adjacent detector pairs to where the decay of ²⁸⁵Cn was observed. Due to the volatility of Cn, the correlation search for the second and third fragment of the ²⁸⁹Fl decay chain was extended from detector X onwards to all detector pairs along the column. The same procedure was performed for the decay chains starting from ²⁸⁸Fl, both respectively in the time windows given above.

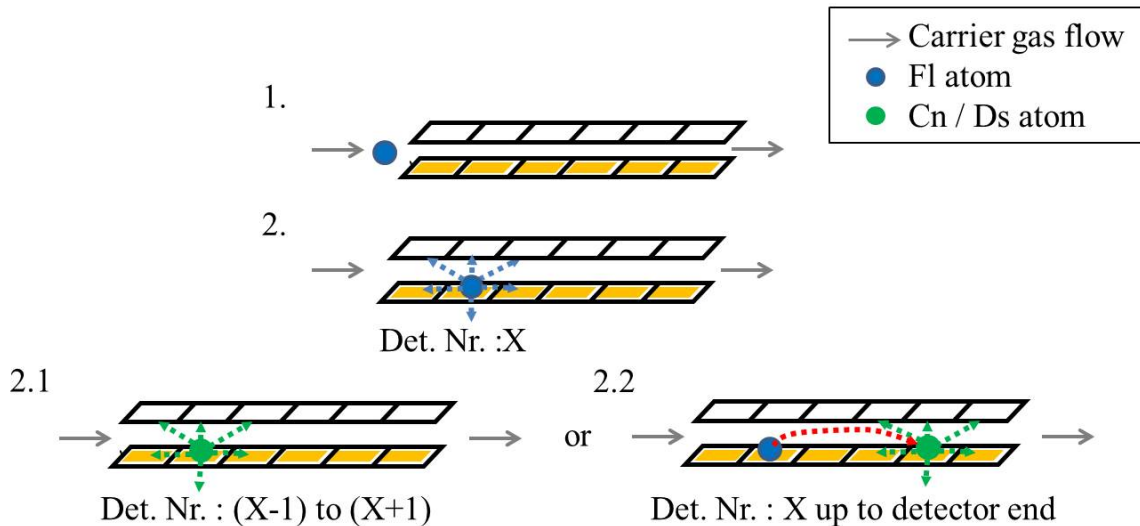


Figure 6.3: Example of a schematic overview on decay positions in a COMPACT detector array for ^{289}Fl decay chain. In step 1, the Fl atom (blue dot) enters together with the carrier gas mixture the Au-covered COMPACT detector. It will interact with the surface and its decay will be observed at a certain position in the detector pair (X) (step 2). For the observation of the daughter nucleus Cn, there are two possibilities: i) Cn and Ds are both observed in the same or adjacent detector pairs as where Fl was observed (detectors :X-1 to X+1) (step 2.1). ii) Due to the volatility of Cn, it can desorb back into the gas phase and is transported with the carrier gas further along the COMPACT detector array, where its decay will be observed (step 2.2).

6.2.2 Background conditions

The search for rare decay chains originating from SHE, can be affected by background contamination caused by the decay of Rn isotopes and their daughters, produced in multi-nucleon transfer reactions. They are produced with production rates in the order of mbarn and can be transported to the detection system by a gas flow. As suggested in section 1.4 and confirmed by experiments, this background can be suppressed by several orders of magnitude by using a kinematic recoil separator like TASCA prior to the chemical separation [82,94].

The background conditions during irradiation times and beam pause periods were analyzed for both optimized Fl experiments T039, and T041. This was important for the determination of the random probability rates of the observed $^{288,289}\text{Fl}$ decay chains in the COMPACT detector setup. Due to the obtained higher statistics in the Fl experiment T041 compared to T039, the obtained energy spectra of events in COMPACT I (see Fig. 6.2) and the distribution of the detected events along COMPACT I and COMPACT II (see Fig. 6.4), obtained during T041 are presented here. As explained earlier, the peaks in energy range of 5 to 8.6 MeV shown in Fig. 6.2 corresponded to α -decays of ^{219}Rn and its daughter nuclei, as also from $^{212-214}\text{Po}$. The background level in the energy range above 8.6 MeV, the region in which the correlation search for $^{288,289}\text{Fl}$ was expected, was very low. In the beam pause periods, the background was lower than in beam-on periods, meaning that the random probability rate for the Fl decay chains detected in the beam pause period was very low. For the chains detected during irradiation time, the random probability rate increased, but was still very small due to the pre-separation from the recoil separator TASCA. The random probability rate was not only influenced by the beam on and pause periods,

but also by the detector position in the COMPACT detector array in which the members of the decay chain were observed. Fig. 6.4 shows the distribution of the detected events per detector in the Au-covered COMPACT I and II detector arrays in the energy range of 8.6 to 10.1 MeV. The black distribution shows the background during beam on target period, whereas the red distribution shows the background during beam pause.

It can be clearly seen that most of the events were detected in the in the first 8 to 10 detectors of COMPACT I, in beam on target as well as in beam pause periods. The background in beam pause periods can be explained by the production of the non-volatile isotopes of Bi and Pb, which have rather long half-lives and slowly migrate into the COMPACT I detector, where their α -decay into the Po isotopes (as seen in Fig. 6.2) was observed. The much higher background during beam on periods was beam related and most likely caused by additional reactions in the detector or by influence of the electro-magnetic impulse from the beam pulse. The background was also relined by isotopes of Rn undergoing decay in flight. The observed background in COMPACT II is very low, and almost negligible in beam pause periods. It is presumably caused from α -decay events of $^{219}\text{Rn} \rightarrow ^{215}\text{Po}$.

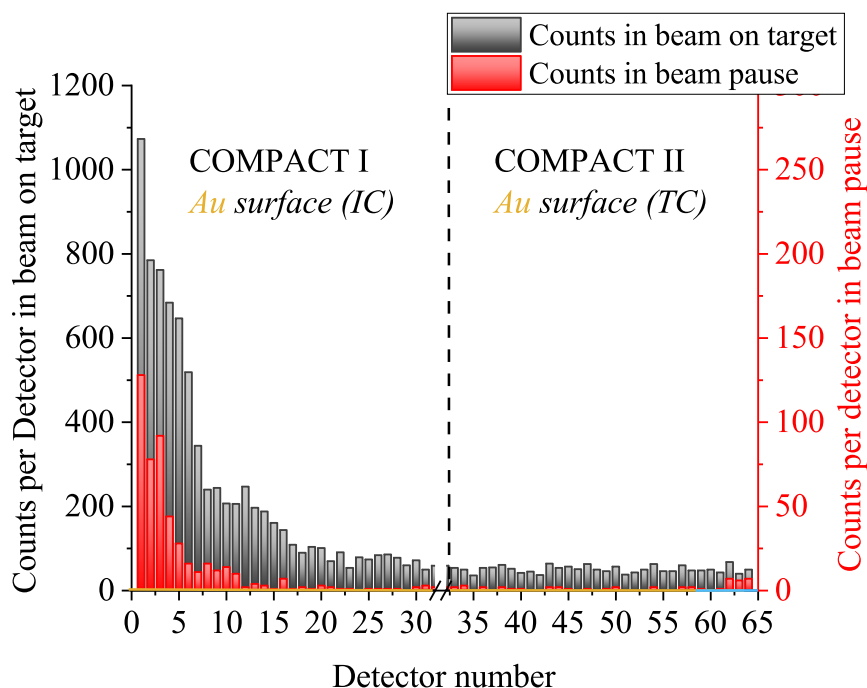


Figure 6.4: The background distribution along COMPACT I and II detector arrays in each Pin diode pair is shown in the energy range of 8.6-10.1 MeV. The black distribution shows the background extracted from the beam on target periods, whereas the red distribution illustrates the background in beam pause. The data was taken from the sum over all Fl measurements in T041 (30 days).

6.2.3 Random rate determination

For each observed correlated decay chain, a value for the probability (N_R) for its random origin was calculated.

The random rate for every observed decay chain originating from ^{289}Fl was calculated by

$$N_R = \lambda(\alpha_1) \cdot \lambda(\alpha_2) \cdot \lambda(SF) \cdot t_{exp} \cdot t_c, \quad (6.1)$$

and for decay chains originating from ^{288}Fl by

$$N_R = \lambda(\alpha_1) \cdot \lambda(SF) \cdot t_{exp} \cdot t_c \quad (6.2)$$

in which $\lambda(\alpha_1)$ corresponded to the rate of events observed in the energy range 9.4 to 10.1 MeV for the detector pair and adjacent detector pairs in which the α_1 decay was observed. The number of events was divided by the experimental time (t_{exp}). $\lambda(\alpha_2)$ was the rate in the energy range of 8.6 to 10.1 MeV. In case the α_2 -decay was observed further downstream along the detector column (Fig. 6.3 (2.2)), the sum of all events starting from adjacent detector pairs of the mother nuclei all along the detector channel to the adjacent detector pairs of the daughter nuclei were taken to determine $\lambda(\alpha_2)$. $\lambda(SF)$ corresponded to the total rate of coincident or single SF fragments. The $\lambda(SF)$ was chosen accordingly, depending on the observation of a single or double SF fragment in the decay chain. Furthermore it was distinguished of whether the α -decay or SF fragment was observed during beam on or beam pause period. As shown in subsection 6.2.2, the sum of events in the above given energy ranges were different for beam on and beam pause periods. This means, that every observed α -decay of the correlated chain in beam pause reduced the random probability rate severely.

In the equations to determine N_R , the experimental time (t_{exp}), and the correlation time windows of 200 s or 1 s (T_c) were taken into account as well. The calculated N_R values for the observed $^{288,289}\text{Fl}$ decay chains are presented in the results section 6.3 of this chapter.

6.3 Results: Observed correlated decay chains

Prior to the Fl experiments, calculations with the new optimized overall chemical efficiencies for T039, and T041 were performed to predict how many decay chains attributed to $^{288,289}\text{Fl}$ should be observed in the COMPACT detector arrays. Therefore the Fl yield was determined using

$$\gamma = \sigma \cdot (N_p \cdot N_T \cdot \eta), \quad (6.3)$$

in which σ was the production cross section, γ the yield, N_p the estimated projectile dose in the experimental period, N_T the number of target atoms, and η the total efficiency of the experimental setup. The total efficiency was comprised out of the efficiency of TASCAs (40%), transmission through the RTC window (80%), the losses in the RTC (50%), the detection efficiency for a single α -decay (76%) or two consecutive α -decays (58%), and the loss of experimental time due to heating of the COMPACT II detector to eliminate the ice layer. This had to be done twice per week, resulting in a reduction of experimental time to about 80%. The expected total efficiency (η) for ^{288}Fl was around 10.0%, and for ^{289}Fl about 7.5%. Taking all of this into account, the expected yield for the experiment T039 was the observation of four decay chains, and for the experiment T041 nine decay chains.

The decay chain correlation search was performed for both experiments, and in total six complete decay chains attributed to ^{288,289}Fl were observed, three incomplete chains starting from ²⁸⁵Cn were detected, and seven pairs of coincidentally detected SF fragments without any α -particle precursor were observed.

In this section an overview on the observed complete and incomplete ^{288,289}Fl decay chains detected in the COMPACT detector setup for both experiments T039, and T041 will be given. The information in which beam period (beam-on target or beam pause) the decays occurred are included, as well as the positions and temperatures in the detector array where they were observed. Detectors in each COMPACT detector array were numbered from 1 to 32. The decays registered during the beam pause periods are marked with black triangles. For the decay chains attributed to ^{288,289}Fl, the calculated N_R values are also given. The observed Fl decay chains given in Ref. [56], will be referred to as chains 1 and 2.

6.3.1 Observed events in experiment T039 (2014)

The search for correlated decay chains revealed one correlated decay chain starting from ²⁸⁹Fl and one decay chain starting from ²⁸⁵Cn, which are shown in Fig. 6.5. The boxes on the right hand side of the decay chains show the α -decay energy and lifetime of the nucleus. The detector number in which the decay was measured and the respective temperature are given on the left hand side. The fission fragment energies are given without corrections for the pulse height defect. The calculated values for the probability (N_R) for the random origin are given for both decay chains.

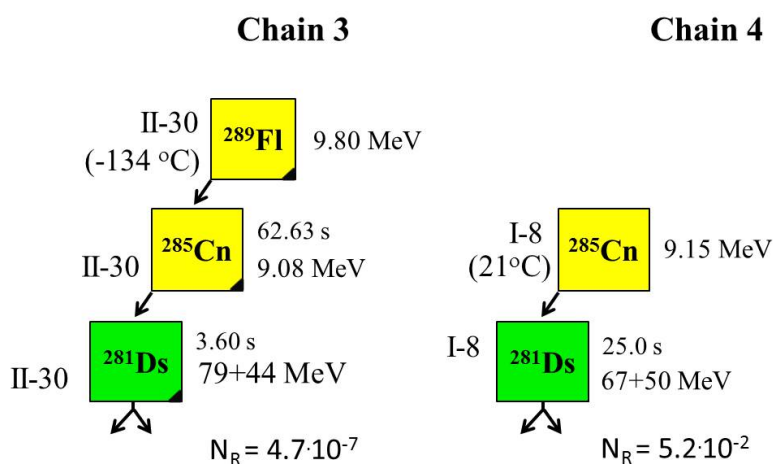


Figure 6.5: Correlated decay chains observed in the Fl experiment T039. Chain 3 was assigned to ²⁸⁹Fl, whereas chain 4 only starts from ²⁸⁵Cn. The α -decay energies, lifetime of the nucleus, detector position and respective temperatures are given. The radioactive decays registered during the beam pause periods are marked with black triangles. The calculated values for the probability (N_R) for the random origin are given for both decay chains.

All three members of chain 3 were observed in detector pair 30 in the Au-covered COMPACT II, which was kept at -134°C. All events were observed in the beam pause period. The members of chain 2 were found in detector pair 8 of the Au-covered COMPACT I, which was kept at 21°C. Here, the events were observed during irradiation time.

Based on the good agreement of the nuclear properties reported from the ²⁸⁹Fl synthesis experiments,

described in section 1.5.1 Fig. 1.9, chain 3 was assigned to the decay of $^{289}\text{Fl} \rightarrow ^{285}\text{Cn} \rightarrow ^{281}\text{Ds}$. Chain 4 was assigned to an incomplete decay chain starting with $^{285}\text{Cn} \rightarrow ^{281}\text{Ds}$. No precursor decay of ^{289}Fl was observed.

Since the members of the decay chain 3 were all observed in beam pause in COMPACT II, the event background was very low. Due to this, the probability of this chain being random was $N_R=4.7 \cdot 10^{-7}$. For the decay chain 4, the random probability rate was calculated to be $5.2 \cdot 10^{-2}$, due to observation of the decays during irradiation time, and the decay position in the COMPACT I detector array (cf. Fig. 6.4).

In addition to the above observed correlated decay chains, four coincident SF events without precursor were found, all in beam pause, cf. Fig. 6.6. Three coincident SF events, were detected at a temperature of 21°C in the SiO_2 -covered COMPACT 0 (detector pair 7, 15/16, and 14). The fourth SF event was observed in detector pair 13 of COMPACT II at -5°C . No single fission fragments with $E_{frag} > 20 \text{ MeV}$ were detected. Furthermore no complete chains originating from ^{288}Fl were observed.

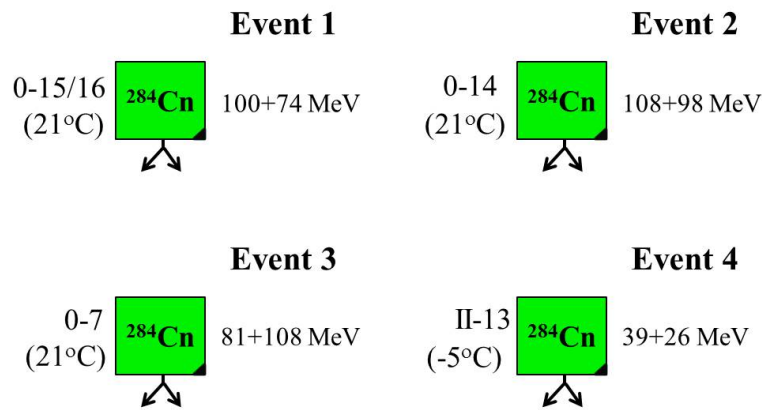


Figure 6.6: Observed coincident fission fragments in the Fl experiment T039, for which no α -decay precursor was found. A possible but only tentative assignment to these spontaneous fission events is ^{284}Cn .

6.3.2 Observed events in experiment T041 (2015)

As mentioned before, the Fl experiment T041 was performed with the current optimal experimental settings determined in chapter 3.

The correlated decay chain search revealed a total of seven observed correlated decay chains, see Fig. 6.7. Based on the good agreement of the nuclear properties compared to the $^{288,289}\text{Fl}$ decay chains shown in Fig. 1.9, two decay chains were assigned to $^{289}\text{Fl} \rightarrow ^{285}\text{Cn} \rightarrow ^{281}\text{Ds}$ and three decay chains were assigned to $^{288}\text{Fl} \rightarrow ^{284}\text{Cn}$, cf. Fig. 6.7. Furthermore, two incomplete decay chains starting from ^{285}Cn were detected. As already described for the observed events in experiment T039, the boxes on the right hand side of the decay chains show the α -decay energy and lifetime of the nucleus. The detector number in which the decay was observed and the respective temperature are given on the left hand side. The fission fragment energies are given without corrections for the pulse height defects. Furthermore the N_R values are given for all decay chains.

The positions of the observed decay chains in the COMPACT detector arrays were distributed into two

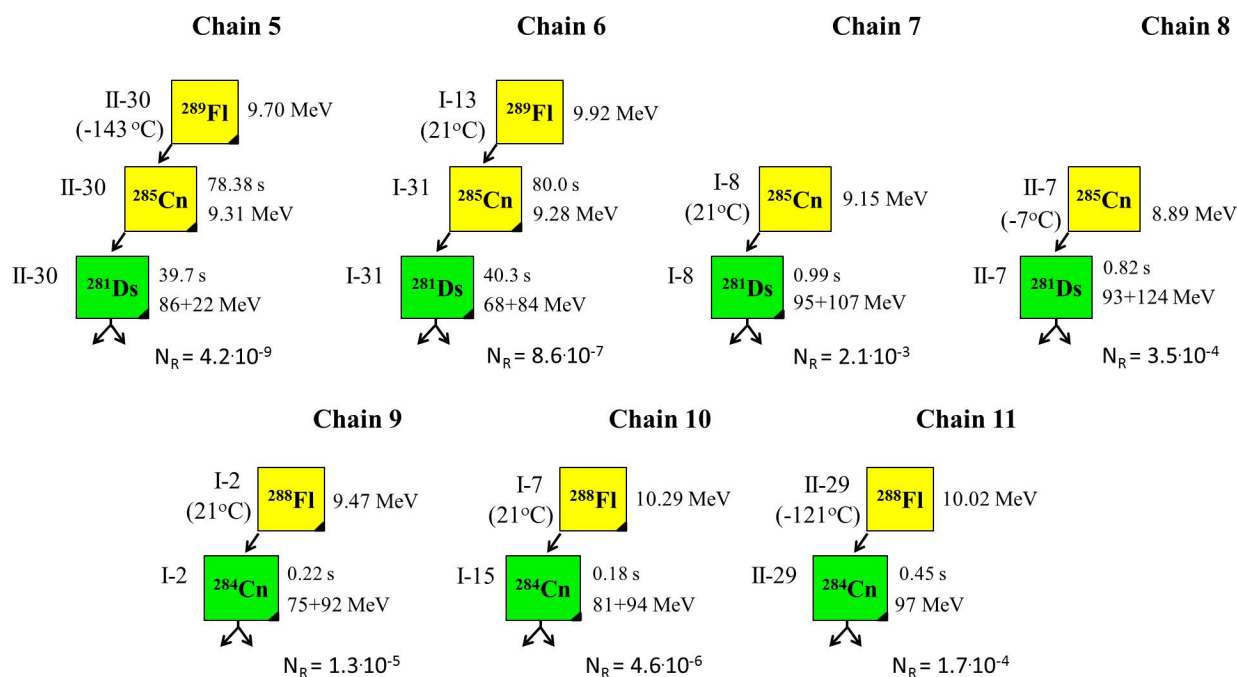


Figure 6.7: Correlated decay chains observed in the Fl experiment T041. In total seven decay chains were detected. From these, four were assigned to ²⁸⁹Fl. Three detected decay chains were assigned ²⁸⁸Fl. The α -decay energy, lifetime of the nucleus, and the detector number in which the signal was measured and the respective temperature are given. The radioactive decays registered during the beam pause periods are marked with black triangles. The calculated values for the probability (N_R) for the random origin are given for both decay chains.

zones in COMPACT I and COMPACT II. Four decay chains (6, 7, 9, 10) were detected in COMPACT I at room temperature (21 °C) around detector pairs 7 to 13. The other 3 decay chains (5, 8, 11) were observed in COMPACT II at temperatures below 0 °C. The incomplete chain starting with ²⁸⁵Cn was observed in detector pair 7, whereas the two decay chains of ^{288,289}Fl were both observed on the thin ice layer of the COMPACT detector array at detector pairs 29 and 30, respectively.

In addition to the above observed correlated decay chains, three coincident SF events without precursor were found, Fig. 6.8. One coincident SF event, was detected on the Au-covered COMPACT I detector at 21 °C (detector pair 11). The two other events were observed in the Au-covered COMPACT II detector in detector pair 11 (-8 °C), and 31 (-165 °C) respectively. No single fission fragments with $E_{frag} > 20$ MeV were detected.

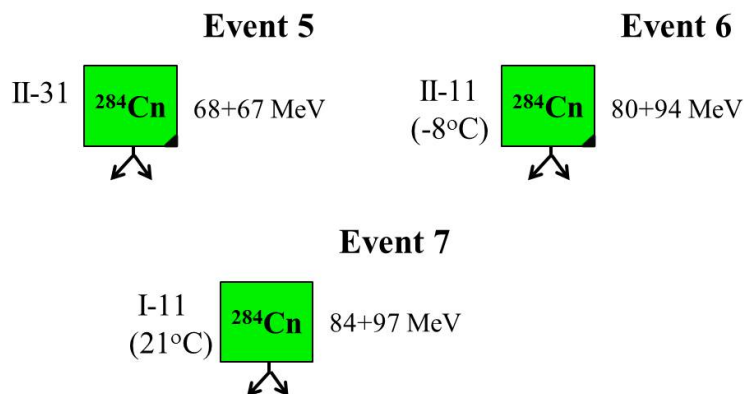


Figure 6.8: Observed coincident fission fragments in the experiment T041, for which no α -decay precursor was found. A possible but only tentative assignment to these spontaneous fission events is ^{284}Cn .

6.3.3 Distribution of the observed events

The distribution of the $^{288,289}\text{Fl}$ decay chains on the SiO_2 and Au-covered COMPACT detector array series observed in the experiments T039, and on the series of Au-covered COMPACT detectors arrays in T041, are shown in Fig. 6.9 panel c). Three Fl decay chains were observed on Au at room temperature (21°C), whereas the other three decay chains were observed on ice in the COMPACT II detector. No Fl decay chains were observed on the SiO_2 -covered COMPACT 0 detector. The Fl decay chains number 6 and 10 are listed once more in panel e), since their daughter nuclei were observed in detector pairs along the COMPACT detector arrays.

The distribution of the incomplete chains, starting with ^{285}Cn are shown in Fig. 6.9 panel d). Two of three chains were detected in the Au-covered COMPACT I detector array. The third decay chain, was observed in COMPACT II, at temperatures below 0°C . The distribution of the SF events for both experiments are shown in Fig. 6.9 panel f). The SF events were observed scattered on all three COMPACT detector arrays.

In order to conclude, whether Fl behave like a noble metal or a noble gas, the deposition patterns of the non-volatile metal Pb, the volatile metal Hg, as also the noble gas Rn are also shown in Fig. 6.9 panel b).

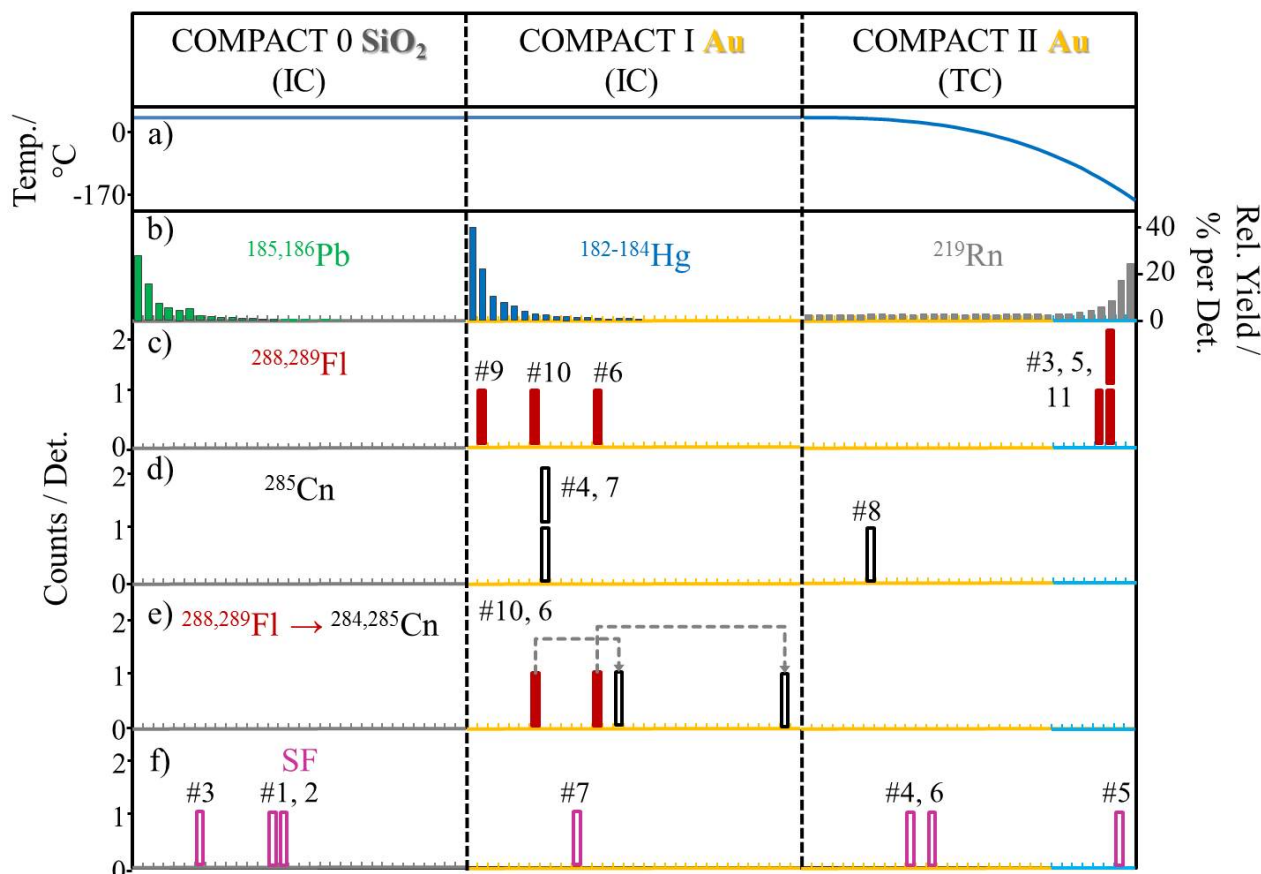


Figure 6.9: The distribution of the $^{288,289}\text{Fl}$ events observed in the experiments T039, and T041 in the SiO₂ and Au-covered COMPACT detector arrays is shown (panel c)). The assignment of the chain numbers was done accordingly to the numeration in the subsections. An illustration of the temperature applied along the detector arrays is given in panel a). The detector pairs 25 to 32 of COMPACT II had temperatures below the dew point (-79°C), so they were covered with a thin ice layer (shown in light blue). For comparison reasons, the distribution pattern of the short-lived $^{182-184}\text{Hg}$ (blue) and $^{185,186}\text{Pb}$ (green) isotopes, as well as for ^{219}Rn (light grey) is shown. The position of observed decay chains starting from $^{285}\text{Cn} \rightarrow ^{281}\text{Ds}$ are shown in panel d) with black open bars. The distribution of the two FI decay chains in which the daughter nuclei were observed in detector pairs along the column, are shown in panel e). The distribution of the observed SF events are shown in panel f) with open pink bars.

6.4 Discussion

6.4.1 Production and Efficiency

The effect of the technical optimizations, described in chapter 3, was reflected in the observed number of decay chains attributed to $^{288,289}\text{Fl}$ in the two experiments. In the FI experiment T039, one full decay chain of ^{289}Fl and one starting from ^{285}Cn was observed. Furthermore, four coincident SF fragments were observed as well. Most likely, they originate from daughters of FI isotopes, however no α -particle from e.g., the short-lived ^{288}Fl precursor could be detected. This can be well explained by the transport time being longer than lifetime. On the contrary, three full decay chains attributed to ^{288}Fl were observed in the FI experiment T041 which was operated with the optimal technical settings, in which high overall

chemical yields and a transport time of 0.3 ± 0.03 s, which is shorter than the half-life of ^{288}Fl was achieved. Furthermore, two full decay chains attributed to ^{289}Fl , two chains starting from ^{285}Cn , and only three coincident SF fragments without α -decay precursor were observed. The higher number of observed Fl decay chains in T041 was larger as a result of the technical optimizations, and due to the length of the experimental time.

As mentioned in the results section 6.3, no single fission fragments with $E_{frag} > 20$ MeV were detected, which means that there was no background in this energy area. This points to the fact that all of the observed coincident events originated from fission fragments. It should be noted that no definite nuclidic assignment could be done for the SF events. The most probable candidate would be ^{284}Cn , the daughter of ^{288}Fl . For the interpretation of the chemical behavior of Fl, the SF fragments as well as the decay chains starting from ^{285}Cn were not taken into consideration. Additionally no unambiguous chemical assignment could be done for ^{285}Cn . Due to the detection efficiency of COMPACT for a single α -particle of 76%, the first α -particle from $^{288,289}\text{Fl}$ could be missing. As mentioned before it could also be that $^{284,285}\text{Cn}$ was formed after the decay of $^{288,289}\text{Fl}$ inside the RTC or transport line, and was transported due to its volatility into the COMPACT detector arrays, where its decay was observed. In the first case the position of the incomplete chain had to be attributed to ^{289}Fl deposition, and could be taken for the analysis of the Fl-Au interaction strength. In the second case, the incomplete chain from ^{285}Cn would contribute to the interaction of Cn with Au. Since none of the above options could be excluded for the incomplete decay chains, both were not taken into account for the chemical discussion of Fl. However, two out of three incomplete chains were detected in COMPACT I at 21°C , where the majority of the Fl events were observed. In the case of two detected Fl decay chains (6 and 10), the high volatility of $^{284,285}\text{Cn}$ was observed (cf. Fig. 6.9 panel e)). Hereby the decay of $^{284,285}\text{Cn}$ was detected further along the detector column as the decay of its mother nuclei $^{288,289}\text{Fl}$. This means, the two observed $^{284,285}\text{Cn}$ events would contribute to the interaction of Cn with Au.

6.4.2 Chemical interpretation

For the discussion of the chemical properties of Fl, the additional events detected in the Fl chemistry experiment at TASCA (T021) reported in Ref. [56] were included. As described in subsection 1.5.3, two correlated decay chains were observed, one attributed to ^{288}Fl , and the other to ^{289}Fl . Both Fl decays were observed at room temperature (21°C) in the Au-covered COMPACT I detector (detector pair 9). Fig. 6.10c) shows the updated Fl distribution along the Au-covered COMPACT detector arrays I and II. The Fl events obtained in T021, are illustrated with empty red bars. Furthermore, for comparison reasons, the deposition of the volatile metal $^{182-184}\text{Hg}$, and noble gas ^{219}Rn are shown in Fig. 6.10b).

The distribution of the Fl events in the chromatography channel shows two deposition zones. Five Fl atoms were deposited in COMPACT I, on the Au surface at room temperature (21°C), and three were observed in COMPACT II at temperatures below -79°C on ice. No decay chain attributed to $^{288,289}\text{Fl}$ was detected on the SiO_2 -covered COMPACT 0 detector array, however this was installed only in the experiment leading to the observation of chains 3 and 4 (cf. Fig. 6.5). This is in accordance to the theoretical calculations, cf. section 1.5.2, in which no interaction of Fl with a SiO_2 surface was predicted [72].

To reproduce the Fl adsorption behavior in the COMPACT setup, the Monte Carlo Simulation (MCS) based

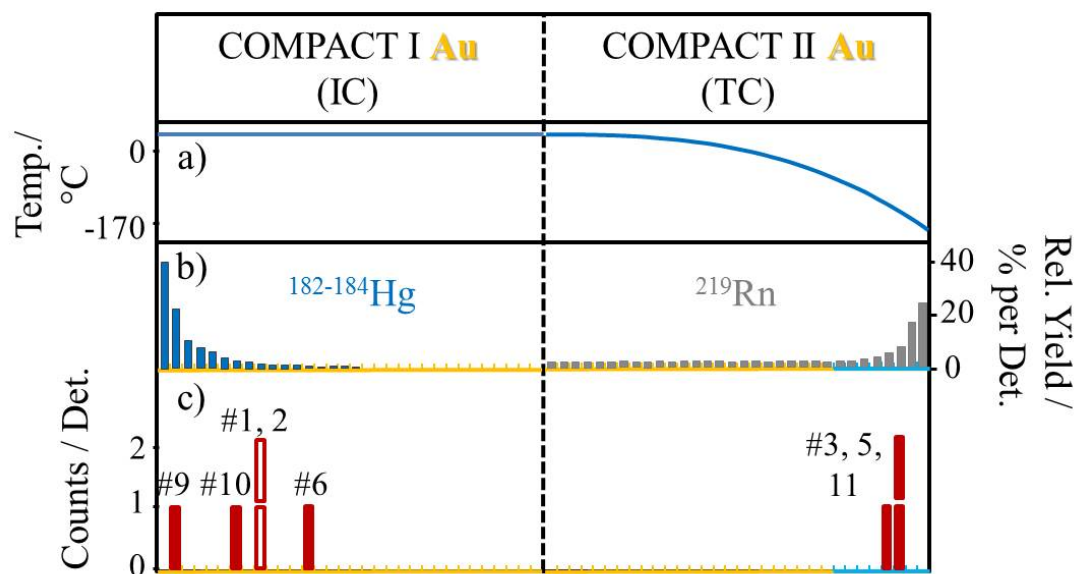


Figure 6.10: Distribution of the observed ^{288,289}Fl events in the Au-covered COMPACT detector arrays in the experiments T039/T041 (red solid bars) (panel c)). Additionally the observed events at TASCA in the experiment T021 are added (red empty bars) [56]. Panel a), shows the temperature gradient applied along the COMPACT detector arrays. For comparison reasons, the distributions of the volatile metal ¹⁸²⁻¹⁸⁴Hg and the noble gas ²¹⁹Rn are shown (panel b).

on the simple adsorption-desorption mechanism, (see subsection 1.4.2), was applied. The $-\Delta H_{ads}$ values which were determined in the previous Fl experiments performed by the PSI-FLNR-LLNL collaboration [81] and by the TASCA collaboration [56] were used, cf. subsection 1.5.3. The results of the MCS are shown in Fig. 6.11.

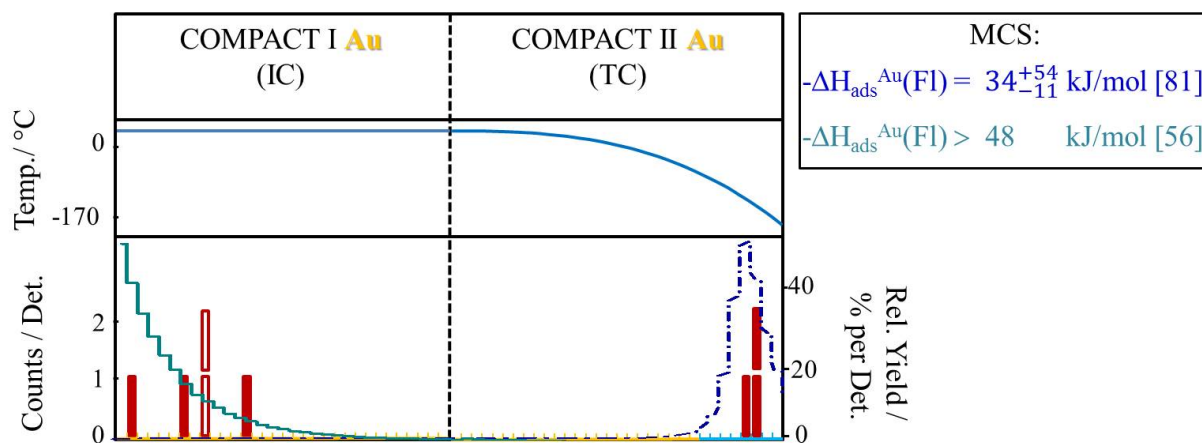


Figure 6.11: Simulation of the the Fl distribution in the COMPACT detector setup using the MC code based on a simple adsorption and desorption mechanism. The blue dashed line shows the MCS using the $-\Delta H_{ads}$ determined in Ref. [81]. The green line shows the MCS using the lower limit of $-\Delta H_{ads}$ determined in Ref. [56].

The experimentally observed two-zone deposition pattern of Fl could not be reproduced by either of the simulated distributions. In case of the $-\Delta H_{ads}^{Au}(Fl)$, from Ref. [81] of 34_{-11}^{+54} kJ/mol (95% c.i.) from which a very volatile and noble gas like behavior for Fl was inferred, the deposition on ice was reproduced (blue

dashed line in Fig. 6.11). The FI events observed on Au at room temperature however, could not be explained. By using the $-\Delta H_{ads}^{Au}(\text{FI}) > 48$ kJ/mol (95% c.i.) taken from Ref. [56], which resulted in the interpretation of FI having a rather metal like behavior, the FI decay chains detected in the COMPACT I detector array could be explained. However the FI events observed on ice could not (green line Fig. 6.11). The deposition of FI in the Au chromatography column does seem to be more complex, so that it cannot be explained by a single-step adsorption-desorption process (so-called mobile adsorption [126]) as used in the common MCS.

One possible explanation for the observation of two deposition zones could be the formation of two FI species. Theoretical calculations predicted FI oxides or hydrides to be thermodynamically unstable compounds which spontaneously decomposed at room temperature into the constituent elements. More stable should be fluorides, however FIF_4 is predicted to be unstable, decomposing into FIF_2 and fluorine [127]. This means that the only thermodynamically stable compound for FI would be FIF_2 . For the present studies on FI, we in general exclude the formation of any chemical FI compounds and more specifically also of FIF_2 due to the following:

- Previous experiments showed a high inertness for FI, although the temperature conditions present were extremely high [81]. In addition, the high primary beam intensity caused plasma formation inside the RTC. These features were not present in our experiment, leading to the conclusion that the observed FI events were not chemical compounds.
- It was not possible to form FIF_2 in the RTC or COMPACT detector arrays, since the carrier gas in the gas transport system consisted of purified He and Ar, with impurities mainly from oxygen and water (kept to a level below 1 ppm). Furthermore, FI atoms could only interact with the Au surfaces of the COMPACT detector, on which no contamination of fluorine was observed (cf. section 5.3).

A more likely explanation for the observed FI deposition in the chromatography columns would be the interaction with a non-ideal Au surface e.g., with irregularities on the Au surfaces in the COMPACT detectors. As described in chapter 5, an extensive surface study was performed on the 50 nm Au layer. The analysis showed that the Au layer covering the silicon PIN diodes consisted mainly of polycrystalline Au grains with different sizes, heights, and different crystallite orientations (mainly (111)). The mean grain size was determined to be around 70 nm, which was close to the average Au layer thickness. To some small extent, well-ordered epitaxial Au (111) crystals were present which had a grain size of about 200 nm, and were determined to be 20 nm taller than the grains originating from polycrystalline Au. Thus, the FI atoms had different adsorption positions on the surface (top, hollow, bridge and also vacancies), which had different adsorption energies according to theoretical predictions (section 1.5.2). The strongest adsorption was predicted for the adatom interaction with the vacancies, see Fig. 1.12.

The adsorption energies and interactions on various adsorption sites on inhomogeneous Au surfaces was not only studied extensively by theory, but also in experiments performed prior to this work. They focused on investigating the strong interaction of Hg atoms on Au surfaces for various applications, e.g. Hg sensors in gas and aqueous phases [128–134]. The experimental investigations showed that the Hg adsorption process on Au (111) could follow various paths [131, 132]. A schematic view of the adsorption process is shown in Fig. 6.12. When a Hg atom was adsorbed in top or bridge position on the Au crystal surface,

its adsorption interaction was weak, and the Hg atom was held solely onto the surface with van der Waals interactions (Fig. 6.12 a)). It was observed that the Hg atom would diffuse to an energetically more favorable position in/on the Au surface crystal to form strong chemical bonds.

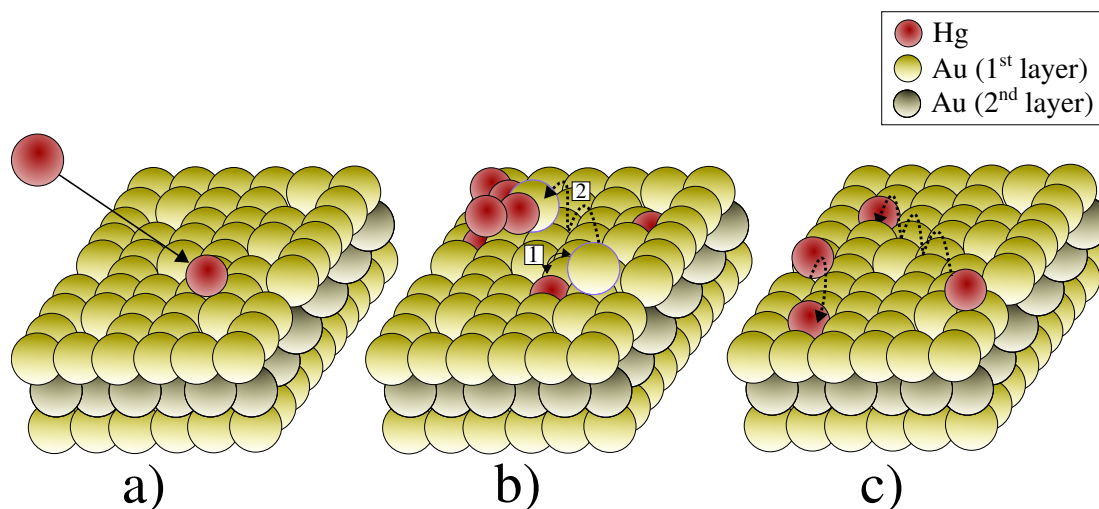


Figure 6.12: Schematic view of Hg adsorption on an inhomogeneous Au surface, in accordance with previous experimental observations given in Ref. [128–134]. a) A Hg atom adsorbs weakly in top or bridge position on the top Au layer. Two different diffusion processes can occur. b) First Hg diffuses underneath the first Au layer and exchanges its position with a Au atom (1). The ejected Au atom diffuses onto the surface with a hopping mechanism until it finds a surface defect, or another Hg atom to form Hg-Au alloy islands (2). c) Shows the second possible diffusion process, in which the Hg atom diffuses rapidly on the surface by the same hopping mechanism to a defect, where it binds strongly.

Two diffusion processes for Hg were observed:

- Since Hg atoms have a similar atomic radius as Au atoms (Hg \approx 171 pm, Au \approx 174 pm [135]), a place exchange could occur. This means, that a Hg atom diffused underneath the Au surface layer and exchanged places with the top Au layer atom, as shown in the step 1 of Fig. 6.12 b). The Au layer atom was ejected, and diffused on the surface until it strongly adsorbed at a defect (step, grain boundary, vacancy), or collided with another Hg atom forming Hg-Au alloy (amalgam) islands. The self-diffusion of a Au adatom on Au(111) surfaces was described as a hopping mechanism across the surface, for which an activation energy of about 0 to 20 kJ/mol was needed [136]; this is shown in step 2 of Fig. 6.12 b). For Hg to diffuse into the Au layer and exchange places with a Au atom, an activation energy had to be overcome.
- The second diffusion process, shown in Fig. 6.12 c), was the surface diffusion of the Hg atom on the Au surface to an energetically more favorable position. This process was found to be more probable than the place exchange mechanism. It was observed that Hg adatoms diffused rapidly across the Au surface with the hopping mechanism to a defect in the surface (vacancy, step or grain boundary). At the defects, the bonds between the Au atoms were not saturated, and a chemical bond between the Hg atom and the Au surface could be formed [129, 130, 132]. The activation energy needed for the surface diffusion of heteroatoms on the Au(111) surface, was reported for transition metals to be around -30 kJ/mol [137].

The results of the adsorption experiments of Hg in the SiO₂ and Au-covered COMPACT detector arrays, discussed in chapter 4, confirmed a strong interaction with the Au surface. MCS based on a simple adsorption-desorption mechanism used the adsorption enthalpy values above the diffusion-controlled deposition limit of 67 kJ/mol. The simulated distribution reproduced the experimentally determined deposition of short-lived Hg isotopes well (cf. section 4.3). Theoretical calculations based on homogeneous Au surfaces resulted in adsorption energies below -50 kJ/mol (shown in Fig. 1.12 curve b)), which was not in agreement with the experimental results. On the contrary, theoretical calculations based on inhomogeneous Au surfaces, resulted in an adsorption energy of ~-100 kJ/mol, which was in better agreement with the experimental data. This leads to the conclusion that the diffusion processes of Hg shown in Fig. 6.12 b) and c), also take place on the Au surface of the COMPACT detector arrays. Taking this into account, an extended code for the MCS was developed, in which the surface diffusion step was included.

The improvements in the MCS code focused only on the time at which the atom remained on the surface, the diffusion across the surface and the diffusion speed. The random time (τ_a) an atom spent on the surface, depended on the desorption energy (ε_{des}) and on the absolute temperature (T). It can be described by [138]:

$$\tau_a = (-\log(1 - RND)) \cdot \tau_0 \cdot \exp\left(\frac{\varepsilon_{des}}{k_B \cdot T}\right) \quad (6.4)$$

where τ_0 is an inverse oscillation frequency of the crystal lattice, ε_{des} is the desorption energy, RND is a random number between 0 and 1, and k_B is the Boltzmann constant and T is the absolute temperature, respectively. The desorption energy was equal to the $-\Delta H_{ads}$ for weakly bound adatoms on the Au surface [138]. During a time τ_a , the adatom diffused across the surface by the hopping mechanism, or diffused into the surface layer and exchanged position with the host surface atoms [136, 139, 140]. The diffusion processes only occurred if the energy barrier height for the diffusion process (E_{dif}) was lower than the desorption energy. If this condition was not fulfilled, the adatoms desorbed back into the gas phase and were transported further along the column, or diffused on the surface but with a low diffusion speed. The diffusion speed (D) on the surface depended on the activation energy for the diffusion step (E_{dif}), temperature (T), lattice parameter (a) and the frequency of the diffusion attempts (ν_0):

$$D = \nu_0 \cdot a^2 \cdot \exp\left(-\frac{E_{dif}}{k_B \cdot T}\right) \quad (6.5)$$

The number of diffusion attempts ν_0 was approximately equal to $\frac{k_B \cdot T}{h}$, in which h is the Planck constant. The random square diffusion displacement of the adatom (Δr^2) on the Au grain was twice the product of the diffusion speed (D) and the random time (τ_a):

$$\Delta r^2 = 2 \cdot D \cdot \tau_a \quad (6.6)$$

If Δr^2 exceeded the grain size, the adatom had reached a defect and was assumed to be chemically bound there.

After the inclusion of the diffusion mechanism into the MCS, the experimentally observed ^{182–184}Hg distribution in the Au-covered COMPACT detector was compared to the updated simulation. The MC was simulated using the following parameter values, which were based on theoretical calculations and data:

- Physisorption on Au (theory): -50 kJ/mol [71, 128, 129]
- Chemisorption on Au (exp.): -98 kJ/mol [113]
- Activation energy for diffusion (E_{dif}) (theory): varied from 10 to 20 kJ/mol. The limits were selected to the difference in adsorption energies at different adsorption positions, e.g. hollow and bridge position [71, 76, 128].
- Au grain size (exp.): 70 nm

The outcome of the simulation is shown as a red curve in Fig. 6.13. The MCS using the simple adsorption-desorption process is shown in the same figure. The data is equally well described by both simulation approaches. This does not mean that the diffusion step is irrelevant, but for Hg the diffusion speed on the surface is rapid enough ($D=1.14 \cdot 10^{-5}$ cm²/s) [141] that in the outcome of the simulations, the two mechanisms cannot be distinguished under experimental conditions.

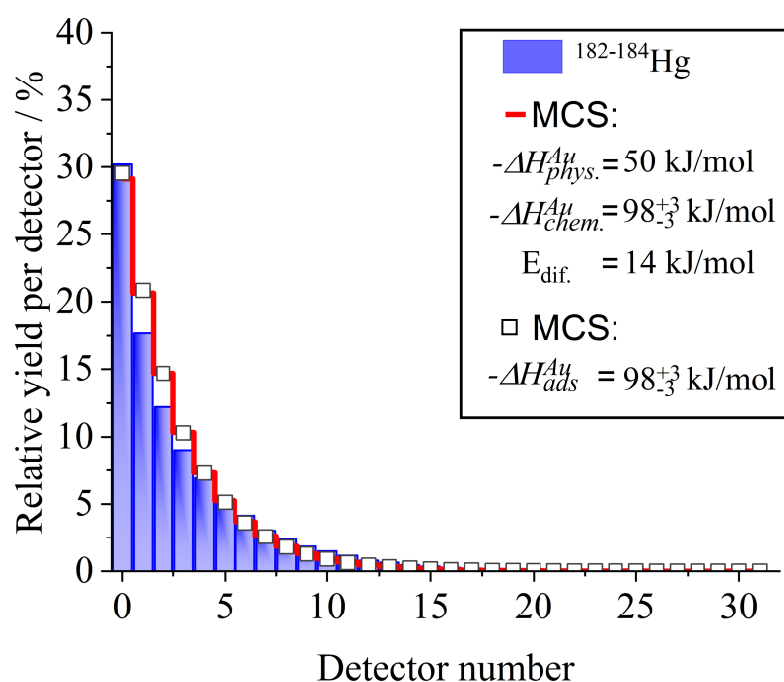


Figure 6.13: ^{182–184}Hg distribution (blue bars) on a Au-covered COMPACT detector measured in pure Ar gas. Red line shows the results of the MCS including surface diffusion, using $-\Delta H_{ads}$ values from Ref. [71, 76, 113, 128, 129]. White squares show the MCS with the simple adsorption-desorption mechanism with the $-\Delta H_{ads}$ taken from Ref. [113].

The MCS with inclusion of the surface diffusion step has proven to be a good description of the experimental results. Based on this, the same MCS was used (with different parameters) to try to describe the two

deposition zones of Fl on the Au-covered COMPACT detector arrays. A different MCS distribution was expected with respect to the simple adsorption-desorption MCS, due to the predicted lower adsorption strength of Fl on Au [71, 76], and a slower diffusion on the surface. The parameters used for simulation were:

- Adsorption on ice (exp.): -29 ± 2 kJ/mol
- Physisorption on Au (exp.): -34 kJ/mol [81]
- Chemisorption on Au (exp.): -67 kJ/mol (diffusion-controlled deposition limit)
- Activation energy for diffusion (E_{dif}) (theory): varied from 15 to 30 kJ/mol [71]

For the simulation only one parameter was variable, the activation energy for diffusion (E_{dif}). The other parameters were based on experimental data and remained constant. The adsorption enthalpy on ice was determined by the comparison of the MCS distribution with the experimentally observed Fl decay chains on ice (chains 3, 5 and 11). Hereby the simulation with the $-\Delta H_{ads}^{ice}(\text{Fl}) = 29 \pm 2$ kJ/mol described the experimental data best. The value for the weak adsorption (physisorption) of Fl on Au was taken from Ref. [81]. The diffusion-controlled deposition limit of -67 kJ/mol, which was determined for strongly adsorbing species on the COMPACT detector array (cf. chapter 4), was adopted for the chemisorption value of Fl on the Au surface. In order to determine the best activation energy value for the diffusion step multiple MCS distributions were performed, with different activation energy values in the range of 15 to 30 kJ/mol. The limits were selected from the difference in adsorption energies at different adsorption positions, e.g. hollow and bridge position [71]. The distribution obtained by the MCS had to agree with the proportion of the two deposition zones (Five Fl events on Au, and three on ice).

In Fig. 6.14, the distribution of the observed Fl atoms on the Au-covered COMPACT detector arrays are shown. In addition, the results of the MCS with variable activation energies ($E_{dif} = 15, 27$ and 30 kJ/mol) are shown as curves. From the comparison of the MCS distributions with the experimental data, it can be stated that neither the simulations with $E_{dif} = 15$ nor 30 kJ/mol could describe the experimental distribution sufficiently. In the case of 15 kJ/mol, similar results as assuming mobile adsorption (cf. Fig. 6.11) were obtained. With 30 kJ/mol, the two deposition zones on Au and ice could be reproduced, but the proportion between them was not as in the data. The MCS distribution which described the experimental data much better than either of the results assuming mobile adsorption and showed the closest proportion to the data had an activation energy value of 27 ± 2 kJ/mol. In Fig. 6.15 the Fl atom distribution in the Au-covered COMPACT detector arrays together with the optimal MCS distribution is shown.

The visible double-peak structure supports our interpretation that Fl followed the surface diffusion mechanism like Hg. However, for Fl this process was slower compared to the diffusion of Hg, and Fl possibly could not substitute a Au atom on the surface due to its larger atomic radius of about 330 pm [142].

The previous chemical investigations on Fl [56, 81] which seemed to have contradictory results, are now proven to be complimentary, and the chemical behavior of Fl in the two deposition zones in the COMPACT detector setup can be explained. The observation of Fl events on ice confirm that Fl is a very volatile element which interacts much weaker with the Au surface than its lighter homolog Pb. Its volatility results

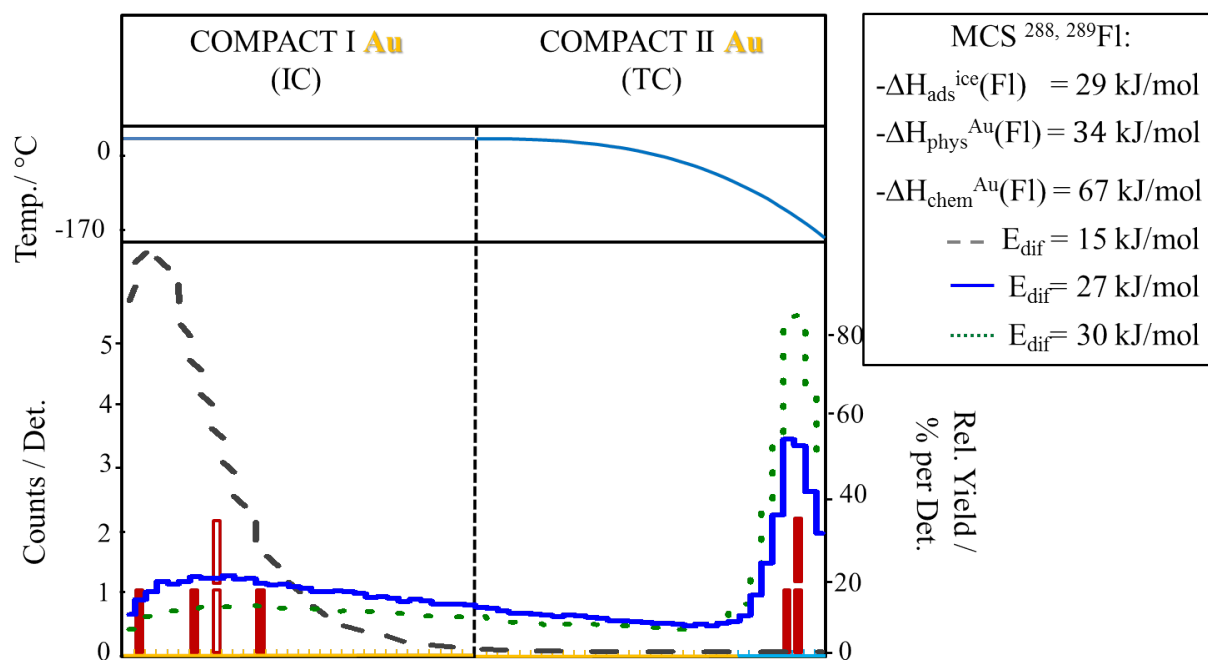


Figure 6.14: Simulations of the FI distribution in the COMPACT setup by the MC code including the surface diffusion step, with different activation energies (E_{dif}) but fixed $-\Delta H_{ads}$ values for the physisorption, chemisorption and adsorption on ice.

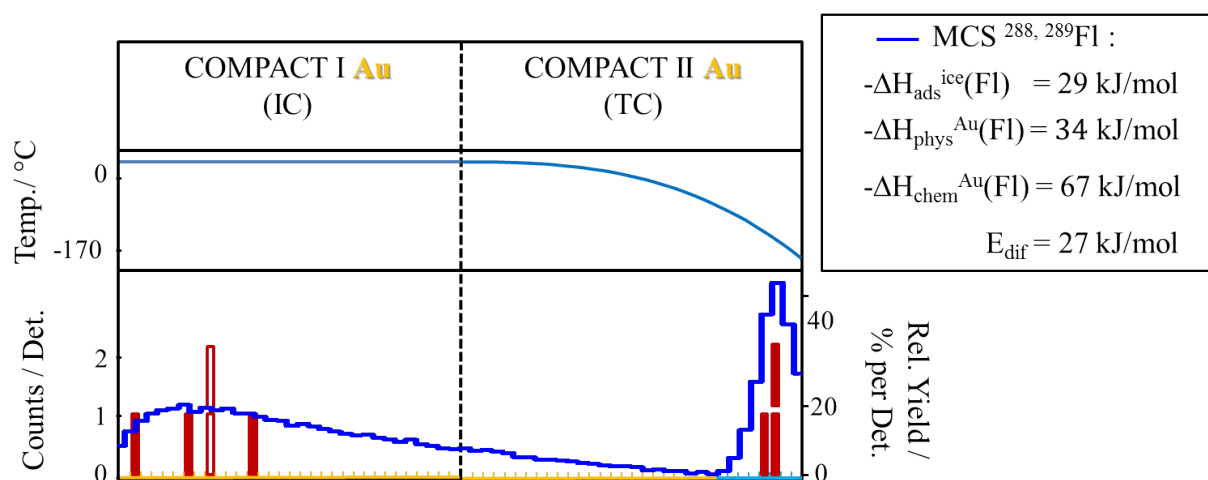


Figure 6.15: Simulation of the FI distribution in the COMPACT setup by the MC code including the surface diffusion step (blue line), using $-\Delta H_{ads}$ values obtained in this work, as also from Ref. [76, 81].

from the strong relativistic stabilization of the quasi closed electron shell configuration. The FI decay chains detected on the Au surface in COMPACT I can be explained as being due to the surface diffusion process on the inhomogeneous Au surface, which offers reactive sites (e.g., grain boundaries). The loosely bound FI atoms diffuse across the surface until they reach a defect (e.g. grain boundary, vacancy) where they are strongly bound and the decay is observed. The interpretation of the two deposition zones is supported by the theoretical calculations shown in section 1.5.2, Fig. 1.12. FI adatoms absorbing on the hollow position on the Au surface, were predicted to have an adsorption enthalpy of around 50 kJ/mol which corresponds to a bonding only due to van der Waals forces (physisorption) (cf. subsection 1.4.1).

On the contrary, for FI adatoms adsorbing onto a vacancy the adsorption energy was determined to be around -90 kJ/mol which corresponds to a chemical bonding (chemisorption), meaning it would be trapped and the decay would be observed as seen in the experiments.

Chapter 7

Conclusion and Future studies

The chemical investigations on Fl are to date still a topic of high interest for theoretical as well as experimental research. Contradictory results of previous experiments [56, 81] together with limited statistics, motivated our recent and improved experiments with the goal to clarify the chemical behavior of Fl.

To achieve this goal, higher statistics for Fl and a better comparison of its chemical behavior with elements in a wide volatility range were essential. Within the scope of this work, the experimental setup was optimized and the chemical separation in the detector channel was improved. The optimizations were tested with short-lived isotopes of Hg and Pb, the homologs of Fl, and its daughter Cn, under the same experimental conditions as used for the Fl studies. Various optimizations resulted in significant reduction of the transportation time from 0.81 ± 0.06 s ([56]) to 0.3 ± 0.03 s, and an increase of the overall chemical yield from 27% ([56]) to $62 \pm 0.5\%$ for volatile elements. The chemical separation was improved by combining COMPACT detector arrays with SiO₂ and Au-covered surfaces, which were operated in series as IC and TC systems. In this way, the separation of the rather non-volatile metal Pb (adsorbed on SiO₂ at 21°C), from the volatile metal Hg (adsorbed on Au at 21°C) and in addition from the noble gas Rn (deposited on ice) was achieved in one detection setup. It was demonstrated that with the new COMPACT detector setup it was possible for the first time to directly compare the chemical behavior of Fl with those of elements of different volatilities. The deposition processes of Hg and Pb in the COMPACT detector arrays were diffusion controlled. A lower limit for the adsorption enthalpy for the diffusion controlled deposition was determined to be -67 kJ/mol. In previous experiments, the experimentally determined distribution patterns of Hg and Pb were evaluated with MCS based on single adsorption-desorption mechanism using the adsorption enthalpies determined [85, 110, 113], and a good agreement between them was observed.

Two successful Fl experiments were performed at TASCA. The isotopes ^{288,289}Fl were produced in the nuclear fusion reaction ⁴⁸Ca+²⁴⁴Pu. By using the gas-filled separator TASCA, in combination with the COMPACT detector setup, it was possible to detect the characteristic α and spontaneous fission (SF) fragments under largely background-free conditions. In a 12-days campaign conducted in 2014, one full decay chain attributed to ²⁸⁹Fl was observed. Furthermore, one incomplete chain starting from ²⁸⁵Cn and four coincident SF fragments without α -precursor were detected. In a 30-days campaign in 2015, five full decay chains of ^{288,289}Fl were observed. In addition, two chains starting from ²⁸⁵Cn and three coincident SF fragments were detected. A longer experimental time in 2015, in combination with additional experimental

improvements, provided increased statistics. Since no definite chemical assignment could be made for the incomplete decay chains and SF fragments, they were not taken into consideration for the chemical interpretation of Fl. All investigations on the chemical properties of Fl conducted at TASCA resulted in the observation of eight Fl events in the COMPACT detector setup. The distribution of the Fl decay chains showed two deposition zones. Five Fl decay chains were observed on Au at 21°C, and three chains were observed on a thin ice layer covering the Au. The possible formation of two Fl species was excluded due to the experimental conditions.

To understand the adsorption behavior of Fl on the Au surface and to compare with theoretical predictions [71,74,76], an extensive surface study was performed on Au samples of the COMPACT detector arrays. The analysis showed that the 50 nm Au layer covering the silicon PIN diodes consisted mainly of polycrystalline Au grains with different sizes, heights, and different crystallite orientations. The mean grain size was determined to be around 70 nm. To some small extent, well ordered epitaxial Au(111) crystals were present, which had a grain size of about 200 nm, and were determined to be 20 nm taller than the grains originating from polycrystalline Au. Theoretical calculations showed that adatoms could adsorb on the Au surface on different adsorption sites, which had different adsorption energies [71,72,74,75]. The strongest adsorption energies were expected for the adatom interacting with vacancies [76]. The adsorbed adatoms could diffuse across the surface to an energetically favorable site [136]. According to experimental and theoretical studies on the adsorption of Hg with inhomogeneous Au surfaces, Hg was found to rapidly diffuse across the Au surface to a defect, where the formation of Hg islands was observed [128–134].

The Monte Carlo code which was used to simulate the adsorption-desorption process in the chromatography column was extended by including the diffusion mechanism across the surface. Thus, the adatom which was loosely bound on the surface was mobile, and could diffuse to a favorable site (e.g. grain boundary, defect) where it was strongly bound. This new approach was tested with the experimentally determined Hg distributions on the inhomogeneous Au COMPACT detectors. The simulations, based on known adsorption and diffusion parameters for Hg, provided a good description of the experimental data. The same MCS adapted to the Fl experiment, was applied to describe the two deposition zones of Fl in the COMPACT setup. The MCS used mainly four parameters, whose values were based on theoretical calculations and experimental data. The adsorption parameters on ice, physisorption and chemisorption on Au were determined experimentally, with values of -29 ± 2 kJ/mol, -34 kJ/mol [81] and ≥ -67 kJ/mol, respectively. The best activation energy value for diffusion was determined to be 27 ± 2 kJ/mol. These parameter values lead to a good agreement between experimental observations and the simulated distribution. This suggested that Fl follows the surface diffusion mechanism like Hg. The observation of the Fl events on ice confirm Fl to be a very volatile element, which interacts much weaker with the Au surface than its lighter homolog Pb. The Fl events observed on Au at 21°C, refer to a metallic character. However Fl is loosely bound at the regular Au crystals, and can rapidly move by diffusion to an energetically favorable position (e.g. defect, grain boundary), where it is trapped and the decay is observed. The previous chemical investigations on Fl which seemed to have contradictory results, are proven to be complimentary.

For the first time, online gas-phase studies on short-lived isotopes of Tl were performed as preliminary studies towards Nh chemistry. The isotopes $^{183-185}\text{Tl}$ were produced in the fusion reaction $^{50}\text{Ti}+^{141}\text{Pr}$, separated by TASCA and flushed out from the RTC to a SiO₂ and Au-covered COMPACT detector setup. The overall chemical efficiency was below 20%. Tl was observed to be very reactive, and deposited on the

SiO₂-covered COMPACT detector array, operated at 21°C. This result was in agreement with theoretical predictions and previous offline experiments [73, 111, 114].

Future studies

The experimental investigations on the chemical properties of Fl have successfully been completed. For the near future no further chemistry experiments on Fl are anticipated, since we are certain that an increase in statistics would show the same experimental results (two-deposition zones) as discussed in this work. Nevertheless, it would be recommendable to perform one more chemistry experiment on Fl, to proof the diffusion on the surface and interaction with defects. For this, COMPACT detector arrays with a homogeneous Au layer would need to be produced. On the physics side, the spectroscopy of Fl is a point of main interest. With a combination of TASCA and the spectroscopy device TISISPEC a definition of a precise Q_α value along the ²⁸⁹Fl decay chain is of interest. Furthermore, a search for the unknown decay chain of ²⁹⁰Fl is anticipated to probe the evolution of shell-stabilizing effects at proton number $Z=114$ towards $N=178$ and $N=184$.

The next SHE, whose chemical properties will be studied at TASCA is nihonium (Nh, $Z=113$). Due to similar production cross-sections as for ^{288,289}Fl and a half-life of about one second, ²⁸⁴Nh will be investigated. It can be produced in the reaction ²⁴³Am(⁴⁸Ca,3n)²⁸⁸Mc via α -decay of the short-lived mother nuclide ²⁸⁸Mc. Similar statistics as obtained for the Fl experiments are expected, nevertheless this may be reduced due to a predicted higher reactivity of Nh in comparison to Fl or Cn, which is predicted by theoretical calculations [73]. For this reason, prior to the Nh studies, further test experiments with the short-lived Tl isotopes will be performed. Online gas-phase studies in the optimized experimental setup will be performed under the same experimental conditions as they will be used for Nh chemistry. In this way, more detailed studies on the chemical adsorption behavior of Tl will be performed in order to increase the overall chemical yield.

In future, chemical studies on the even heavier transactinides moscovium (Mc, $Z=115$) and livermorium (Lv, $Z=116$) are planned, which are predicted to be relatively reactive. With the current optimized experimental setup, they cannot be investigated due to the fact that the transportation time is longer than their half-lives ($T_{1/2} < 0.2$ s). A new chemical setup is needed allowing to reduce the transportation time below 50 ms. For this, investigations on the use of a buffer gas cell instead of the RTC are conducted and test experiments are ongoing. In addition, special mini-COMPACT detector arrays which can be combined with the gas stopping cell, as also with a newly designed RTC have been produced. New transportation time measurements will be performed.

Bibliography

- [1] D. C. Hoffman *et al.*,: Chemistry of the heaviest elements-one atom at a time. *J. Chem. Educ.* 76, 331 (1999)
- [2] M. Schädel: Chemistry of Superheavy Elements. *Angew. Chem. Int. Ed.* 45, 368 (2006)
- [3] L. Öhrström, J. Reedijk: Names and symbols of the elements with atomic numbers 113, 115, 117 and 118. (IUPAC Recommendations 2016), *Pure Appl. Chem.* 88 (12), 1225-1229 (2016)
- [4] A. Türler, V. Pershina: Advances in the Production and Chemistry of the Heaviest Elements. *Chem. Rev.* 113, 1237-1312 (2013)
- [5] M. Schädel, D. Shaughnessy: *The Chemistry of Superheavy Elements. Second Edition*, Springer-Verlag Berlin/ Heidelberg (2014)
- [6] A. Sobiczewski, K. Pomorski: Description of structure and properties of superheavy nuclei. *Progress in Particle and Nuclear Physics* 58, 292-349 (2007)
- [7] Y. Oganessian: Heaviest nuclei from ^{48}Ca -induced reactions. *J. Phys. G: Nucl. Part. Phys.* 34, R165-R242 (2007)
- [8] P. Pykkö: Relativistic effects in structural chemistry. *Chem. Rev.* 88, 563-594 (1988)
- [9] B. Fricke: *Superheavy Elements: A Prediction of their Chemical and Physical Properties*. Springer Verlag, Berlin Heidelberg GmbH 21, 89-144 (1975)
- [10] P. Pykkö, J. Desclaux: Relativity and the Periodic System of Elements. *Acc. Chem. Res.* 12(8), 276-281 (1979)
- [11] C. F. von Weizsäcker: Zur Theorie der Kernmassen. *Z. Phys. A* 96(7), 431-458 (1935)
- [12] K. H. Lieser: *Einführung in die Kernchemie*, (Verl. Chem. Weinheim [u.a]), 2., neubearb. u. erw. Auflage, (1980)
- [13] M. G. Mayer: On Closed Shells in Nuclei II. *Phys. Rev.* 75, 1969-1970 (1949)
- [14] O. Haxel, J. H. Jensen, H. E. Suess: On the "Magic Numbers" in Nuclear Structure. *Phys. Rev.* 75, 1766 (1949)
- [15] H. A. Bethe, R. F. Bacher: Stationary States of Nuclei. *Reviews of Modern Physics. Nuc. Phys. A* 8, 82-229 (1936)

- [16] N. Bohr, J. A. Wheeler: The Mechanism of Nuclear Fission. *Phys. Rev.* 56, 426-450 (1939)
- [17] W.D. Myers, W. J. Swiatecki: Nuclear masses and deformations. *Nucl. Phys.* 81, 1-60 (1966)
- [18] S. G. Nilsson, S. G. Thompson, C. F. Tsang: Stability of superheavy nuclei and their possible occurrence in nature. *Phys. Lett.* 28B, 458-461 (1969)
- [19] M. G. Mayer: On Closed Shells in Nuclei. *Phys. Rev* 74, 235-239 (1948)
- [20] W. D. Myers: *Droplet Model of Atomic Nuclei*. Plenum, New York (1977)
- [21] M. G. Mayer: Nuclear Configurations in the Spin-Orbit Coupling Model I. Empirical Evidence. *Phys. Rev.* 78, 16-21 (1950)
- [22] M. G. Mayer: Nuclear Configurations in the Spin-Orbit Coupling Model II. Theoretical Considerations. *Phys. Rev.* 78, 22-23 (1950)
- [23] V. M. Strutinsky: Shell effects in nuclear masses and deformation energies. *Nuc. Phys. A* 95(952), 420-442 (1967)
- [24] V. M. Strutinsky: "Shells" in deformed nuclei. *Nuc. Phys. A* 122(1), 1-33 (1968)
- [25] S. G. Nilsson: Binding states of individual nucleons in strongly deformed nuclei. *Kgl. Danske Videnskab. Selskab, Mat.-fys. Medd.* 29(16) (1955)
- [26] J. R. Nix: Calculation of fission barriers for heavy and superheavy nuclei. *Annual Review of Nuclear Science* 22(1), 65-120 (1972)
- [27] P. Möller, J. R. Nix: In *Third International Atomic Energy Symposium on Physics and Chemistry of Fission*, Volume 1 , 103, Rochester, New York IAEA, Vienna, Paper SM-174/202 (1973)
- [28] W. D. Myers, W. J. Swiatecki: Nuclear properties according to the Thomas-Fermi model. *Nucl. Phys. A* 601, 141-167 (1996)
- [29] A. Sobczewski: Structure of Heaviest Nuclei. *Acta Physica Polonica B* 29, 2191 (1998)
- [30] G. A. Lalazissis *et al.*,: Superheavy nuclei in the relativistic mean-field theory. *Nucl. Phys. A* 608, 202-226 (1996)
- [31] S. Cwiok *et al.*,: Shell Structure of the Superheavy Elements. *Nucl. Phys. A* 611, 211-246 (1996)
- [32] J.-F. Berger *et al.*,: Superheavy, Hyperheavy and Bubble Nuclei. *Nuc. Phys. A* 685, 1c-16c (2001)
- [33] W. J. Swiatecki, K. Siwek-Wilczynska, J. Wilczynski: Fusion by diffusion. II. Synthesis of transfermium elements in cold fusion reactions. *Phys. Rev. C.* 71, 014602 (2005)
- [34] S. Hofmann: Auf der Jagd nach Superschwergewichten. *Physik Journal* 4, 37-43 (2005)
- [35] V. Zagrebaev, M. Itkis, Y. Oganessian: Fusion-Fission Dynamics and Perspectives of Future Experiments. *Physics of Atomic Nuclei* 66, 1033-1041 (2003)

BIBLIOGRAPHY

- [36] V. Pershina: Relativistic electronic structure studies on the heaviest elements. *Radiochim. Acta* 99, 459-476 (2011)
- [37] T. Sikkeland, J. Maly, D. F., Lebeck: Evaporation of 3 to 8 neutrons in reactions between ^{12}C and various uranium nuclides. *Phys. Rev.* 169, 1000-1006 (1968)
- [38] E. V. Fedoseev *et al.*: Thermochromatographic separation of the products of nuclear reactions in the form of β -diketonates. *J. Radioanal. Nucl. Chem. Letters* 119, 347-354 (1987)
- [39] I. Zvara *et al.*: The chemical properties of element 104. *J. of Nucl. Energy* 21 (7), 601-603 (1967)
- [40] R. Silva *et al.*: Chemical separation of rutherfordium. *In. and Nucl. Chem. Letters* 6, 871-877 (1970)
- [41] M. Schädel: Chemistry of the Transactinide Elements. *Radiochim. Acta* 70/71, 207-223 (1995)
- [42] M. Schädel: Aqueous chemistry of transactinides. *Radiochim. Acta* 89, 721-728 (2001)
- [43] M. Schädel: The chemistry of the transactinide elements-experimental achievements and perspectives. *J. Radioanal. Nucl. Chem.* 3, 113-120 (2002)
- [44] Y. Nagame *et al.*: Chemical studies on rutherfordium (Rf) at JAERI. *Radiochim. Acta* 93, 519-526 (2005)
- [45] J. P. Omtvedt *et al.*: Review of the SISAK system in transactinide research: recent developments and future prospects. *J. Alloys Compd.* 271-273, 303 (1998)
- [46] Ch. E. Düllmann: Chemical Investigation of Hassium (Hs, Z=108). Inauguraldissertation der philosophischen-naturwissenschaftlichen Fakultät der Universität Bern (2002)
- [47] A. Yakushev: Chemical Characterization of Element 108, Hassium and Synthesis of New Hassium Isotopes. Habilitation Thesis in the Field of Radiochemistry at Technical University of Munich (2009)
- [48] I. Zvara: The Inorganic Radiochemistry of Heavy Elements. (Springer Science + Business Media B. V.) (2008)
- [49] I. Zvara: Thermochromatographic method of separation of chemical elements in nuclear and radiochemistry. *Isotopenpraxis* 26, 251 (1990)
- [50] I. Zvara: Simulation of Thermochromatographic Processes by the Monte Carlo Methods. *Radiochimica Acta* 38, 95-101 (1985)
- [51] J. Even *et al.*: Rapid Synthesis of Radioactive Transition-Metal Carbonyl Complex at Ambient Conditions. *Inorg. Chem.* 51, 6431-6433 (2012)
- [52] B. Eichler, J. V. Kratz: Electrochemical deposition of carrier-free radionuclides. *Radiochim. Acta* 88, 475-482 (2000)
- [53] J. Even: Developments for transactinide chemistry experiments behind the gas-filled separator TASCA. Dissertation zur Erlangung des Grades "Doktor der Naturwissenschaften" am Fachbereich Chemie, Pharmazie und Geowissenschaften der Johannes Gutenberg-Universität Mainz (2011)

- [54] H. Poppe: Mass transfer in rectangular chromatographic channels. *J. Chromatogr. A* 948, 3-17 (2002)
- [55] E. R. Gilliland, *Industrial and Engineering Chemistry* 26, 681-685 (1934)
- [56] A. Yakushev *et al.*,: Superheavy Element Flerovium (Element 114) is a Volatile Metal. *Inorg. Chem.* 53, 1624-1629 (2014)
- [57] A. Türler, R. Eichler, A. Yakushev: Chemical studies of elements with $Z \geq 104$ in gas phase. *Nucl. Phys. A* 944, 640-689 (2015)
- [58] J. Even *et al.*,: Synthesis and detection of a seaborgium carbonyl complex. *Science* 345, 1491-1493 (2014)
- [59] Yu. Ts. Oganessian, V. K. Utyonkov: Super-heavy element research. *Rep. Prog. Phys.* 78, 036301 (2015)
- [60] V. K. Utyonkov *et al.*,: Experiments on the synthesis of superheavy nuclei ^{284}Fl and ^{285}Fl in the $^{239,240}\text{Pu}+^{48}\text{Ca}$ reactions. *Phys. Rev. C* 92, 034609 (2015)
- [61] Yu. Ts. Oganessian *et al.*,: Synthesis of superheavy nuclei in the $^{48}\text{Ca}+^{244}\text{Pu}$ reaction: $^{288}114$. *Phys. Rev. C* 62, 041604 (R) (2000)
- [62] Yu. Ts. Oganessian *et al.*,: Measurements of cross sections for the fusion-evaporation reactions $^{244}\text{Pu}(^{48}\text{Ca},xn)^{292-x}114$ and $^{245}\text{Cm}(^{48}\text{Ca},xn)^{293-x}116$. *Phys. Rev. C* 69, 054607 (2004)
- [63] L. Stavsetra *et al.*,: Independent verification of element 114 production in the $^{48}\text{Ca}+^{242}\text{Pu}$ reaction. *Phys. Rev. Lett.* 103, 132502 (2009)
- [64] P. A. Elisson *et al.*,: New superheavy element isotopes: $^{242}\text{Pu}(^{48}\text{Ca},5n)^{285}114$. *Phys. Rev. Lett.* 105, 182701 (2010)
- [65] J. M. Gates *et al.*,: First superheavy element experiments at the GSI recoil separator TASCA: The production and decay of element 114 in the $^{244}\text{Pu}(^{48}\text{Ca},3-4n)$ reaction. *Phys. Rev. C* 83, 054618 (2011)
- [66] Ch. E. Düllmann *et al.*,: Production and decay of element 114: high cross sections and the new nucleus ^{277}Hs . *Phys. Rev. Lett.* 104, 252701 (2010)
- [67] V. Zagrebaev *et al.*,: Synthesis of superheavy nuclei: How accurately can we describe it and calculate the cross sections?. *Phys. Rev. C* 65, 014607 (2001)
- [68] W. Reisdorf, M. Schädel: How well do we understand the synthesis of heavy elements by heavy-ion induced fusion?. *Z. Phys. A* 343, 47-57 (1992)
- [69] W. Kohn, A. D. Becke, R. G. Parr: Density functional theory of electronic structure. *J. Phys. Chem.* 100, 12974-12980 (1996)
- [70] A. Rosen: Twenty to thirty years of DV- $X\alpha$ calculations: A survey of accuracy and applications. *Adv. Quant. Chem.* 29, 1-47 (1997)

- [71] V. Pershina, J. Anton, T. Jacob: Theoretical predictions of adsorption behavior of elements 112 and 114 and their homologs Hg and Pb. *J. Chem. Phys.* 131, 084713 (2009)
- [72] V. Pershina: A relativistic periodic DFT study on interaction of superheavy elements 112 (Cn) and 114 (Fl) and their homologs Hg and Pb, respectively, with a quartz surface. *Phys. Chem. Chem. Phys.* 18, 17750-17756 (2016)
- [73] V. Pershina: Theoretical Study on the Adsorption Behavior of Element 113 and its Homologue Tl on a Quartz Surface: Relativistic Periodic DFT Calculations. *J. Phys. Chem. C* 120 (36), 20232-20238 (2016)
- [74] V. Pershina: Theoretical chemistry of superheavy elements: Support for experiment. *EPJ Web of Conferences* 131, 07002 (2016)
- [75] V. Pershina private communication, TAN conference (2014)
- [76] V. Pershina: Reactivity of Superheavy Elements Cn, Nh, and Fl and Their Lighter Homologues Hg, Tl, and Pb, Respectively, with a Gold Surface from Periodic DFT Calculations. *Inorg. Chem.* 57, 3948-3955 (2018)
- [77] K. S. Pitzer: Are elements 112, 114, and 118 relatively inert gases?. *The Journal of Chemical Physics* 63, 1032-1033 (1975)
- [78] A. Yakushev *et al.*: First attempt to chemically identify element 112. *Radiochim. Acta* 89, 743-745 (2001)
- [79] A. Yakushev *et al.*: Chemical identification and properties of element 112. *Radiochim. Acta* 91, 433-439 (2003)
- [80] H.W. Gäggeler *et al.*: Chemical and nuclear studies of hassium and element 112. *Nucl. Phys. A* 734, 208-212 (2004)
- [81] R. Eichler *et al.*: Indication for a volatile element 114. *Radiochim. Acta* 98, 113-139 (2010)
- [82] D. Wittwer *et al.*: Gas Phase chemical studies of superheavy elements using the Dubna gas-filled recoil separator- Stopping range determination. *Nucl. Instrum. Methods B* 268, 28-35 (2010)
- [83] A. Yakushev, R. Eichler: Gas-phase chemistry of element 114, flerovium. *EPJ Web of Conferences* 131, 07003 (2016)
- [84] R. Eichler *et al.*: Thermodynamische und physikalische Eigenschaften von Element 112. *Angew. Chem.* 120 (7), 3306-3310 (2008)
- [85] R. Eichler *et al.*: Chemical characterization of element 112. *Nature* 447, 72-75 (2007)
- [86] Ch. E. Düllmann: Superheavy element research at GSI. *Radiochim. Acta* 99, doi. 10.1524/ract.2011.1842 (2011)
- [87] J. Runke *et al.*: Preparation of actinide targets for the synthesis of the heaviest elements. *J. Radioanal. Nucl. Chem.* 299, 1081-1084 (2014)

- [88] A. Semchenkov *et al.*,: The TransActinide Separator and Chemistry Apparatus (TASCA) at GSI- Optimization of ion-optical structures and magnet designs. Nucl. Instr. and Meth. in Phys. Res. B 266, 4153-4161 (2008)
- [89] J. Even *et al.*,: The recoil transfer chamber-An interface to connect the physical preseparator TASCA with chemistry and counting setups. Nucl. Inst. and Meth. in Phys. Res. A 638, 157-164 (2011)
- [90] P. Scharrer: Charge state distributions of low-energy heavy ions Passing through dilute Gases: Basic studied and application in a pulsed Gas Stripper for the GSI UNILAC. Dissertation zur Erlangung des Grades "Doktor der Naturwissenschaften" am Fachbereich Physik der Johannes Gutenberg-Universität Mainz (2017)
- [91] J. Khuyagbaatar *et al.*,: $^{48}\text{Ca}+^{249}\text{Bk}$ Fusion Reaction Leading to Element Z=117: Long-Lived α -Decaying ^{270}FDb and Discovery of ^{266}Lr . PRL 112, 172501 (2014)
- [92] E. Jäger *et al.*,: High Intensity target wheel at TASCA : target wheel control system and target monitoring. J. Radioanal Nucl. Chem. 299, 1073-1079 (2014)
- [93] Ch. E. Düllmann: Physical separators for the heavies elements. Nucl. Inst. and Meth. in Phys. Res. B 266, 4123-4130 (2008)
- [94] Ch. E. Düllmann: Physical preseparation: A powerful new method for transactinide chemists. Eur. Phys. J. D 45, 75-80 (2007)
- [95] A. Ghiorso *et al.*,: SASSY, A Gas-Filled Magnetic Separator For The Study of Fusion Reaction Products. Nucl. Inst. and Meth. in Phys. Res. A 269, 192-201 (1988)
- [96] IAEA Nuclear Data Section, Nuclear Data Sheets 111, 275 (2010)
- [97] J. F. Ziegler, M. D. Ziegler, J. P. Biersack: SRIM-The stopping and range of ions in matter. Nucl. Inst. and Meth. Phys. Res. B 268, 1818-1823 (2010)
- [98] J. F. Ziegler: SRIM- The Stopping Range of Ions in Matter, www.srim.org, Downloaded: 08.10.2014 (2013)
- [99] V. Pershina, A. Borschevsky, E. Eliav, U. Kaldor: Atomic Properties of Element 113 and Its Adsorption on Inert Surfaces from ab Initio Dirac-Coulomb Calculations. J. Phys. Chem. A 112, 13712-13716 (2008)
- [100] V. Pershina, A. Borschevsky, E. Eliav, U. Kaldor: Adsorption of inert gases including element 118 on noble metal and inert surfaces from ab initio Dirac-Coulomb atomic calculations. J. Phys. Chem. 129, 144106 (2008)
- [101] U. W. Kirbach *et al.*,: The Cryo-Thermochromatographic Separator (CTS): A new rapid separation and α -detection system for on-line chemical studies of highly volatile osmium and hassium (Z=108) tetroxides. Nucl. Instr. and Meth. Phys. Res. A 484, 587-594 (2002)
- [102] Ch. E. Düllmann *et al.*,: Chemical investigation of hassium (element 108). Nature 418, 859-862 (2002)

BIBLIOGRAPHY

- [103] M. Wegrzecki *et al.*,: Design and properties of silicon charged-particle detectors developed at the Institute of Electron Technology (ITE). Proc. SPIE 8902, Electron Technology Conference 2013, 890212 (2013)
- [104] J. M. Gates *et al.*,: Background Reduction in TASCAs. GSI Scientific Report, PHN-NUSTAR-SHE-14 (2011)
- [105] U. Forsberg *et al.*,: First Experiment at TASCAs Towards X-Ray Fingerprinting of Element 115 Decay Chains. Acta Phys. Polonica B 43, 305-311 (2012)
- [106] Ch. E. Düllmann *et al.*,: Upgrade of the Gas-filled Recoil Separator TASCAs and First Search Experiment for the New Element 120 in the Reaction $^{50}\text{Ti}+^{249}\text{Cf}$. GSI Scientific Report, PHN-NUSTAR-SHE-02 (2011)
- [107] J. Khuyagbaatar *et al.*,: The Performance of TASCAs in the $^{48}\text{Ca}+^{206,207,208}\text{Pb}$ Reactions. GSI Scientific Report, NUSTAR-SHE-02 (2009)
- [108] J. Khuyagbaatar Private communication, GSI (2014)
- [109] Chu, S. Y. F., Ekström, L. P., Firestone, R. B.: The Lund / LBNL Nuclear Data Search. Version 2.0 (1999)
- [110] S. Soverna: Attempts to chemically characterize element 112. Inauguraldissertation der Philosophisch-naturwissenschaftlichen Fakultät der Universität Bern (2004)
- [111] A. Serov *et al.*,: Adsorption interaction of carrier-free thallium species with gold and quartz surfaces. Radiochim. Acta 101, 421-425 (2013)
- [112] B. Eichler: Das Verhalten flüchtiger Radionuklide im Temperaturgradientrohr unter Vakuum. Report ZFK-346, Zentralinstitut Kernforschung Dresden (1977)
- [113] S. Soverna *et al.*,: Thermochromatographic studies of mercury and radon on transition metal surfaces. Radiochim. Acta. 73, 1-8 (2005)
- [114] P. Steinegger, *et al.*,: Vacuum Chromatography of Tl on SiO_2 at the Single-Atom Level. J. Phys. Chem. C 120 (13), 7122-7132 (2016)
- [115] L. Lens, *et al.*,: Online chemical adsorption studies of Hg, Tl, and Pb on SiO_2 and Au surfaces in preparation for chemical investigations on Cn, Nh, and Fl at TASCAs Radiochim. Acta. 106(12), 949-962 (2018)
- [116] J. Goldstein *et al.*,: Scanning Electron Microscopy and X-Ray Microanalysis. Third Edition, Springer USA (2003)
- [117] A. Lorenz: Das Eindringen von Elektronen in Materie. EMTEC: Labor für Elektronenmikroskopie, www.analytik.de/emtec (30.04.1997)
- [118] Actinide Research Quarterly, Los Alamos National Laboratory operated by the University of California for the US Department of Energy, Copyright@UC 1998-2000

- [119] R. E. Van Grieken, A. A. Markowicz: Handbook X-ray Spectrometry. Second edition, revised and expanded, Marcel Dekker Inc., New York Basel (2002)
- [120] G. Haugstad: Atomic Force Microscopy Understanding Basic Modes and Advanced Applications. John-Wiley&Sons Inc. Hoboken New Jersey (2012)
- [121] N. G. Semaltianos, E. G. Wilson: Investigation of the surface morphology of thermally evaporated thin gold films, on mica, glass, silicon and calcium fluoride substrates by scanning tunneling microscopy. Thin Solid Films 366, 111-116 (2000)
- [122] Y. Golan, L. Margulis, I. Rubinstein: Vacuum-deposited gold films I. Factors affecting the film morphology. Surf. Sci. 264, 312-326 (1992)
- [123] M. A. George, W. S. Glaunsinger: The electrical and structural properties of gold films and mercury-covered gold films. Thin Solid Films 245, 215-224 2015 (1994)
- [124] Gaspar *et al.*: Influence of the layer thickness in plasmonic gold nanoparticles produced by thermal evaporation. Sci. Refp. 3, 1469 (2013)
- [125] N. Mahmoodi, A. I. Rushdi, J. Bowen, A. Sabouri, C. J. Anthony, P. M. Mendes, J. A. Preece: Room temperature thermally evaporated thin Au film on Si suitable for application of thiol self-assembled monolayers in micro/nano-electro-mechanical-systems sensors. Journal of Vacuum Science and Technology A: Vacuum, Surfaces, and Films 35, 041514-1 -6 (2017)
- [126] B. Eichler, I. Zvara: Evaluation of the Enthalpy of Adsorption from Thermochromatographical Data. Radiochim. Acta 30, 233-238 (1982)
- [127] P. Schwerdtfeger and M. Seth: Relativistic quantum chemistry of the superheavy elements. Closed-shell element 114 as a case study. J. Nucl. Radiochem. Sci. 3, No. 1, (2002)
- [128] J. A. Steckel: Density functional theory study of mercury adsorption on metal surfaces. Phys. Rev. B 77, 115412 (2008)
- [129] D. -H. Lim, S. Aboud, J. Wilcox: Investigation of adsorption behavior of mercury on Au(111) from first principles. Environ. Sci. Technol. 46, 7260-7266 (2012)
- [130] L. Ling *et al.*: Application of computational chemistry in understanding the mechanisms of mercury removal technologies: A review. Energy Environ. Sci. 8, 3109-3133 (2015)
- [131] M. A. George, W. S. Glaunsinger, T. Thundat, S. M. Lindsay: Investigation of mercury adsorption on gold films by STM. Journal of Microscopy, Vol. 152, Pt 3, 703-713 (1988)
- [132] T. Hou, M. Chen, G. W. Greene, R. G. Horn: Mercury Vapor Sorption and Amalgamation with a Thin Gold Film. ACS Appl. Mater. Interfaces 7, 23172-23181 (2015)
- [133] M. Levlin, H. E.-M. Niemi, P. Hautojärvi, E. Ikävalko: Mercury adsorption on gold surfaces employed in the sampling and determination of vaporous mercury: a scanning tunneling microscopy study. Fresenius J. Anal. Chem. 355, 2-9 (1996)

BIBLIOGRAPHY

- [134] M. A. Butler, A. J. Ricco, R. J. Baughmann: Hg adsorption on optically thin Au films. *J. Appl. Phys.* 67, 4320 (1990)
- [135] Mathematics Element Data: Atomic Radius of the elements. www.periodictable.com (05.12.2018)
- [136] G. Antczak, G. Ehrlich: Jump processes in surface diffusion. *Surf. Sci. Rep.* 62, 39-61 (2007)
- [137] S. M. Rossnagel, R. S. Robinson: Surface diffusion activation energy determination using ion beam microtexturing. *J. of Vacuum Science and Technology*
- [138] Y. M. Sabri, S. J. Ippolito, J. Tardio, S. K. Bhargava: Study of Surface Morphology Effects on Hg Sorption-Desorption Kinetics on Gold Thin-Films. *J. Phys. Chem. C* 116, 2483-2492 (2012)
- [139] T. T. Tsong: Mechanisms of surface diffusion. *Progress in Surface Science* 67, 235-248 (2001)
- [140] G. Antczak, G. Ehrlich: *Surface Diffusion: metals, metal atoms, and clusters*. Cambridge University Press, New York (2010)
- [141] H. N. Aiyer, T. Kawazoe, J. Lim, Y. Echigo, M. Ohtsu: Mercury treatment of optical near-field fibre probes for smoother tips with reduced light leakage. *Nanotechnology* 12, 368-371 (2001)
- [142] V. Pershina: Electronic structure and chemical properties of superheavy elements. *Russ. Chem. Rev.* 78, 1153 (2009)

Appendices

A.1 HIVAP predictions

In this section plots of predicted cross-sections for the reactions $^{48}\text{Ca}+^{142}\text{Nd}$, $^{48}\text{Ca}+^{144}\text{Sm}$, $^{50}\text{Ti}+^{140}\text{Ce}$, $^{50}\text{Ti}+^{141}\text{Pr}$, and $^{50}\text{Ti}+^{142}\text{Nd}$ are shown. They were calculated with the statistical model HIVAP [68, 108].

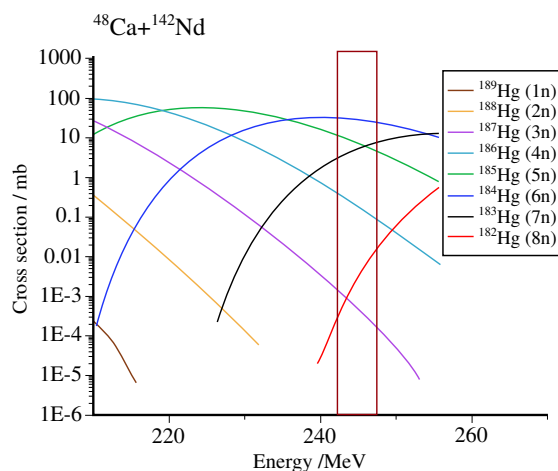


Figure A.1: HIVAP calculations for the reaction $^{48}\text{Ca}+^{142}\text{Nd}$. The framed area, is the beam energy in the center of the target (242-246 MeV) in which the cross-sections were determined.

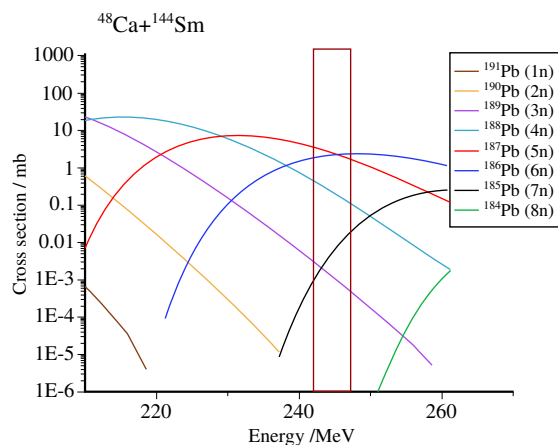


Figure A.2: HIVAP calculations for xn channel of the reaction $^{48}\text{Ca}+^{144}\text{Sm}$. The framed area, is the beam energy in the center of the target (242-246 MeV) in which the cross-sections were determined.

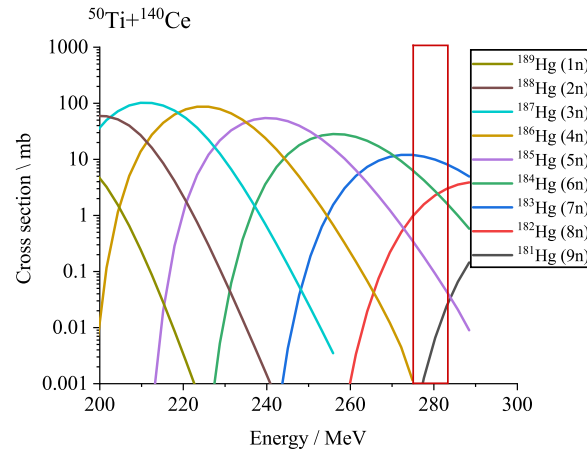


Figure A.3: HIVAP calculations for xn channel of the reaction $^{50}\text{Ti}+^{140}\text{Ce}$. The framed area, is the beam energy in the center of the target (277-284 MeV) in which the cross-sections were determined.

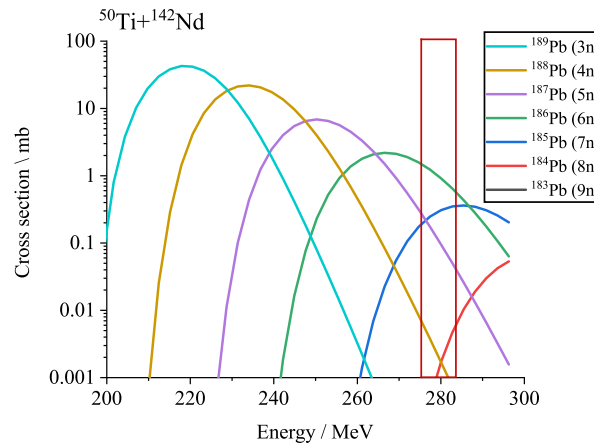


Figure A.4: HIVAP calculations for xn channel of the reaction $^{50}\text{Ti}+^{142}\text{Nd}$. The framed area, is the beam energy in the center of the target (277-284 MeV) in which the cross-sections were determined.

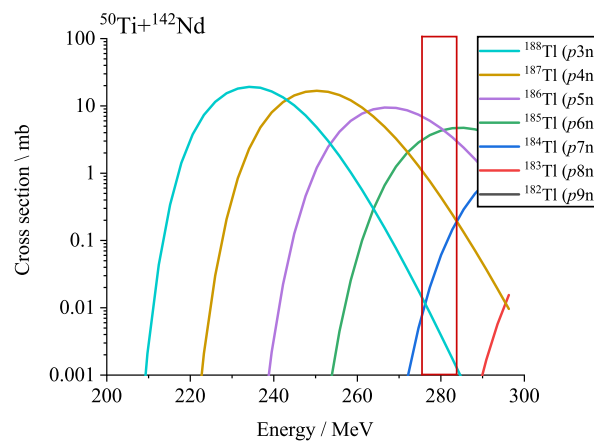


Figure A.5: HIVAP calculations for pxn channel of the reaction $^{50}\text{Ti}+^{142}\text{Nd}$. The framed area, is the beam energy in the center of the target (277-284 MeV) in which the cross-sections were determined.

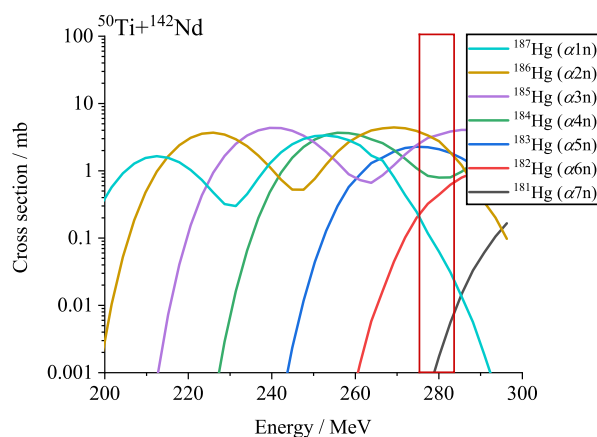


Figure A.6: HIVAP calculations for αxn channel of the reaction $^{50}\text{Ti}+^{142}\text{Nd}$. The framed area, is the beam energy in the center of the target (277-284 MeV) in which the cross-sections were determined.

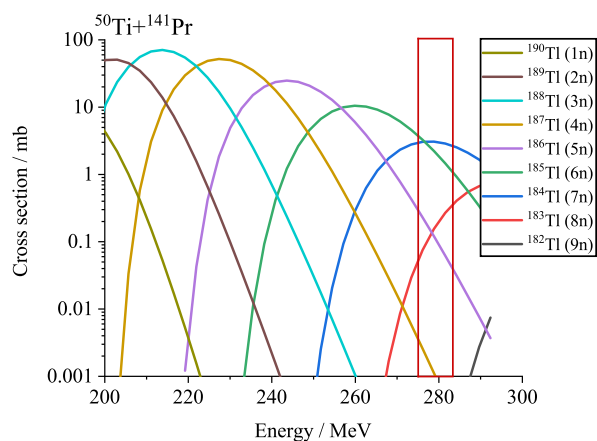


Figure A.7: HIVAP calculations for xn channel of the reaction $^{50}\text{Ti}+^{141}\text{Pr}$. The framed area, is the beam energy in the center of the target (277-284 MeV) in which the cross-sections were determined.

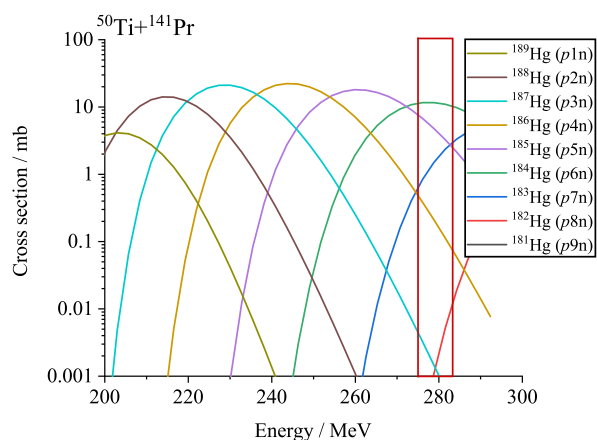


Figure A.8: HIVAP calculations for pxn channel of the reaction $^{50}\text{Ti}+^{141}\text{Pr}$. The framed area, is the beam energy in the center of the target (277-284 MeV) in which the cross-sections were determined.

A.2 Source codes of the Monte Carlo Simulations

The Monte Carlo codes presented in this section used to determine simulations for the comparison to the experimentally determined distribution patterns. In subsection A.2.1 the MC code will be given which was based on the simple adsorption-desorption mechanism [50]. The extended MC code, in which the surface diffusion step was included is given in subsection A.2.2.

A.2.1 Monte Carlo code based on the simple adsorption-desorption mechanism

```

#include <iostream>
#include <time.h>
#include <stdlib.h>
#include <cmath>
#include <fstream>
#include <assert.h>
#include <math.h>
#include <vector>

using namespace std;
int main ()

// Setting the Parameters
{
cout << "choose your standard temperature, press 0 if you want to run the program
with 273.15 K, press 1 if you want to run the program with 298.15 K:";
int STD;
cin >> STD;
double Tstd;
if (STD==1)
{Tstd= 298.15;}
else {Tstd=273.15;}
cout << Tstd << "\n";
double Pstd;
Pstd = 1.01325;

// Input data to the code. Adjusted for every experiment and investigated isotope

cout << "Number of molecules for each dHads: " ;
long int I;
cin >> I ;

double DHa;
cout << "Adsorption enthalpy [-kJ/mol]: " ;
cin >> DHa ;

cout << "Molecular mass of the investigated species [g/mol]: " ;
double M1 ;
cin >> M1 ;

```

```
cout << "Molecular mass of the carrier gas [g/mol]: " ;
double M2 ;
cin >> M2 ;

cout << "Density of the investigated species [g/cm^3]: " ;
double D1 ;
cin >> D1 ;

cout << "Density of the carrier gas at its boiling point [g/cm^3]: ";
double D2 ;
cin >> D2 ;

cout << "Half-life of the isotope [s]: " ;
double halflife ;
cin >> halflife ;

cout << "Gas flow rate [cm^3/s]:" ;
double Q ;
cin >> Q;

cout << "Pressure of the carrier gas in the RTC [bar] : " ;
double p ;
cin >> p ;

cout << "Period of oscillations [10^-12 s]: " ;
double osc ;
cin >> osc ;
double p0 ;
p0 = osc*(1e-12) ;

cout << "Length of the column [cm]: " ;
int LENGTH ;
cin >> LENGTH ;

double WIDTH;          // width of the column [cm]
WIDTH = 1;

double HEIGHT;         // Height of the column [cm]
HEIGHT = 0.06;

cout << "Number of steps in the histogram: ";
int hist_steps ;
cin >> hist_steps;

// Definition of constants

double phi;
phi = WIDTH / HEIGHT;
cout << "width/height"; cout << phi ; cout << "\n";
double f1 ;
double f2 ;
double f3 ;
```

```

f1= 7.3; f2=31.05; f3=47.94;           // Poppe coefficients
cout << f1; cout << "\n";
cout << f2; cout << "\n";
cout << f3; cout << "\n";

double R=8.31432e+7;                   //Ideal gas constant
double PI=3.141592653589;

cout << R ;cout << "\n";

// Definition of variables

double T1,T2;                          //The temperatures at the place of the molecule
double d, D273;                         //Diffusion coefficient
double Nm,Ni;                           //Mean jump length; Random jump length
double xi;                               //The coordinate variable in the column
double ti;                               //The summed time for Ith molecule
double tai;                             //Random time of a full adsorption cycle
double tf;                              //Time of one jump
double tmi;                             //Mean time for staying on the surface
double lifetime;                       //Lifetime of the Ith molecule
double Roo;                             //Retention coefficient according to Poppe
double vi;                              //The mean number of collisions
double Temp_x;
double cm[LENGTH];
double t[LENGTH];

int a,b;                                //counters for various loops
int L;                                   //counter for the index of the Lth molecule
double Random (void);

double out;

/* Temperatures of the COMPACT detector arrays. As an example, two COMPACT
   detector arrays. The first detector was kept at room temperature and
   along the second a negative temperature gradient was applied. The fit
   function for the temperature gradient was defined with origin. It has
   to be changed in the program for every new gradient. A definition has
   to be made, from which detector on there is a thin ice layer. */

for(xi=0; xi<64; xi++)
{
t[int(xi)] = 295;
}
t[64]=294.15;
t[65]=292.43;
t[66]=291.11;
t[67]=289.69;
t[68]=288.12;
t[69]=286.37;

```

```
t[70]=284.43;
t[71]=282.28;
t[72]=279.90;
t[73]=277.27;
t[74]=274.37;
t[75]=271.19;
t[76]=267.69;
t[77]=263.87;
t[78]=259.70;
t[79]=255.16;
t[80]=250.21;
t[81]=244.85;
t[82]=239.03;
t[83]=232.73;
t[84]=225.92;
t[85]=218.58;
t[86]=210.67;
t[87]=202.14;
t[88]=192.98;
t[89]=183.15;
t[90]=172.59;
t[91]=161.28;
t[92]=149.17;
t[93]=136.22;
t[94]=122.38;
t[95]=107.60;
t[96]=107.60;

//Calculate the diffusion coefficient in the carrier gas, using Gillilands formula.

D273=0.0044 * pow(273.15,1.5) * sqrt(1.0/(M1)+1.0/(M2)) /
((p)*pow((pow((M1)/(D1),1.0/3)+pow((M2)/(D2),1.0/3)),2));
cout << "D="; cout<< D273; cout<< "\n";
cout << "\n";

srand((unsigned int)time(NULL));

for(a=0; a<LENGTH; a++)
{
    //Initialize array
    cm[a]=0;
}

{
    //Loop for I Molecules
    L=0;
    do
    {
        xi=0.; //Reset distance coordinate
        ti=0.; //Reset total time
        tf=0.; //Time of one jump
        tai=0.; //Time of one adsorption cycle
        Roo=1.; //Ro is 1 for the first molecule to avoid error message
```

```

//Calculate the lifetime of the atom
lifetime=(-log(1-Random())/log(2))*halflife;

//-----
//--Loop for adsorption cycles while the total time is less than lifetime--
//-----

do
{
    //-----
    //-----subcycle 1: Jump-----
    //-----
    T1 = t[(int)xi]; //Temperature in position x
    // Calculate the diffusion
    d=D273*pow((T1/273.15),1.5);
    if(tai!=0)
    Roo=tai/(tf+tai);

    // Then calculate the mean jump length

    Nm = ((2 * HEIGHT * WIDTH * d) / (Q*(Pstd/p)*T1/Tstd))+
    ((f1 + f2 * Roo + f3 * Roo*(Roo))*(Q*(Pstd/p)*T1/Tstd)*
    HEIGHT*(HEIGHT))/(WIDTH*HEIGHT*105 * d*(1+Roo)*(1+Roo));

    //Determine the random jump length

    Ni=-Nm*log(1-Random());

    //Evaluate the coordinate of the molecule
    xi+=Ni;
    if(xi>LENGTH)
    {
        L++;
        out++;
        break;
    }

    // Determine the temperature at the new position
    T2 = t[(int)xi];
    tf=0;

    //Calculate the flight time
    tf=2 * WIDTH * HEIGHT * Ni / ((Q*(Pstd/p)*T1/Tstd)+(Q*(Pstd/p)*T2/Tstd));

    //Determine the total time of the Ith atom
    ti+=tf;

    // Calculation of random time an atom spends on the surface
    tmi=p0*exp((DHa)*(1e10)/(R*T2));

    // Determination of the mean number of collisions
    vi = ((WIDTH + HEIGHT) / (Q*(Pstd/p)*T2/Tstd)) * sqrt(2*R*T2/(PI*M1));

```

```

//Generate a random time of a full adsorption cycle
tai= (-vi) * tmi * Nm * log(1-Random());

//Update total time
ti+=tai;

if(ti>=lifetime)
{
//add the final position of this molecule to the output-array
(cm [(int)xi])++;
L+=1;
break;
}

}while(ti<lifetime);          //This is the end of the loop for one molecule

}while(L<I);          //This is the end of the loop for I molecules

} //This brace closes the DHa-loop

for(a=0; a<LENGTH; a++)
{
cout << "\n", cm[int(xi),a], a;
cout << cm[a] ;
};
cout << "\n" << "out \n" << out;
cout << "\n";
getchar();

// Output file
ofstream myfile;
myfile.open ("result.txt");
myfile << "-----\n";
myfile << "Date:          Time:          \n\n";
myfile << "Number of molecules for each adsorption enthalpy:  " << I << "\n";
myfile << "Adsorptionenthalpy [kJ/mol]:          " << -DHa << "\n";
myfile << "Molecular weight of the gas:          " << M2 << "\n";
myfile << "Density of carrier gas at boiling point:  " << D2 << "\n";
myfile << "Molecular weight of the investigated species:  " << M1 << "\n";
myfile << "Density of the investigated species:  " << D1 << "\n";
myfile << "Gas flow rate [sscm/s] :          " << Q << "\n";
myfile << "Pressure [bar]:          " << p << "\n";
myfile << "Period of oscillations of the molecule (1e-12):  " << p0 << "\n";
myfile << "Half-life of the nuclide [s]:          " << halflife << "\n";
myfile << "Diffusion Coefficient at 273.15 K [cm^2/s]  " << D273 << "\n";
myfile << "Column lenght [cm]:          " << LENGTH << "\n";
myfile << "Height of the column [cm]          " << HEIGHT << "\n";
myfile << "Width of the column [cm]          " << WIDTH << "\n";
myfile << "Width / heigth ratio          " << phi << "\n";
myfile << "Parameter in Golays eq. according to Poppe:  f0:  " << f1 << "\n";
myfile << "          f1:  " << f2 << "\n";

```

```

myfile << "                                     f2:  " << f3 << "\n";
myfile << "\n";

for(a=0; a<LENGTH; a++)
{
myfile << "\n", cm[int(xi),a], a;
myfile << cm[a]  ;
};
myfile << "\n" << "out \n" << out;
myfile.close();
printf("\n");
}

double Random (void)    //returns a Random number between 0 and 1
{
double a=1;
while(a==1)    //a=1 leads to underflow in Tau. a MUST be between 0 and 0.99999
a=(double)rand()/((double)RAND_MAX);
return (double)rand()/((double)RAND_MAX);
}

```

A.2.2 Extended Monte Carlo Code including the surface diffusion step

```

#include <iostream>
#include <time.h>
#include <stdlib.h>
#include <cmath>
#include <fstream>
#include <assert.h>
#include <math.h>
#include <vector>

using namespace std;
int main ()
{
// Setting the Parameters
int STD;
STD=0;
//cin >> STD;
double Tstd;
if (STD==1)
{Tstd= 298.15;}
else {Tstd=273.15;}
cout << Tstd << "\n";
double Pstd;
Pstd = 1.01325;

/* Input data to the code. They are adjusted for every experiment and
investigated isotope of an element. */

```

```
cout << "Number of molecules for each dHads: " ;
long int I;
cin >> I;

double DHaphysAu;
cout << "Physisorption enthalpy on Au [-kJ/mol]: " ;
cin >> DHaphysAu ;

double DHaphysIce;
cout << "Physisorption enthalpy on ice [-kJ/mol]: " ;
cin >> DHaphysIce ;

double DHachem;
cout << "Chemisorption enthalpy [-kJ/mol]: " ;
cin >> DHachem ;

double Ed;
cout << "Diffusion energy [kJ/mol] :" ;
cin >> Ed ;

double Rc;
cout << "Cluster diameter [cm] :" ;
cin >> Rc ;

cout << "Molecular mass of the investigated species [g/mol]: " ;
double M1 ;
cin >> M1 ;

cout << "Molecular mass of the carrier gas [g/mol]: " ;
double M2 ;
cin >> M2 ;

cout << "Density of the investigated species [g/cm^3]: " ;
double D1 ;
cin >> D1 ;

cout << "Density of the carrier gas at its boiling point [g/cm^3]: " ;
double D2 ;
cin >> D2 ;

cout << "Half-life of the isotope [s]: " ;
double halflife ;
cin >> halflife ;

cout << "Gas flow rate [cm^3/s]: " ;
double Q ;
cin >> Q ;

cout << "Pressure of the carrier gas in the RTC [bar]: " ;
double p ;
cin >> p ;
```



```

cout << "Period of oscillation [10^-12 s]: " ;
double osc ;
cin >> osc ;
double p0 ;
p0 = osc*(1e-12) ;

cout << "Length of the column [cm]: " ;
int LENGTH ;
cin >> Length ;

double WIDTH; //width of the column [cm]
WIDTH = 1;
double DHa;
double DHaphys;

double HEIGHT; // Height of the column [cm]
HEIGHT = 0.06;

cout << "Number of steps in the histogram: " ;
int hist_steps ;
cin >> hist_steps ;

// Definition of constants

double phi;
phi = WIDTH / HEIGHT;
cout << "width/height"; cout << phi ; cout << "\n";
double f1 ;
double f2 ;
double f3 ;

f1= 7.3; f2=31.05; f3=47.94; // Poppe coefficients
cout << f1; cout << "\n";
cout << f2; cout << "\n";
cout << f3; cout << "\n";

double R=8.31432e+7; //Ideal gas constant
double PI=3.141592653589;
double KB=1.38065e-16; // Boltzmann constant
double h=6.626e-27; // Planck constant

cout << R ;cout << "\n";

// Definition of variables

double T1,T2; //The temperatures at the place of the molecule
double d, D273; //Diffusion coefficient on surface and in gas
double Nm,Ni; //Mean jump length; random jump length
double xi; //The coordinate variable in the column

```

```

double ti;           //The summed time for Ith molecule
double tai;         // Random time of a full adsorption cycle
double tdi;
double td;          //Total Time for a diffusion
double Nmax;        //Max number of diffusion attempts
double ta;          //Time for an adsorption step
double tf;          //Time of one jump
double tm;          //Mean time for staying on the surface
double tmi;         // Mean random time for staying on the surface
double lifetime;   //Lifetime of the Ith molecule
double Roo;         //Retention coefficient according to Poppe
double vi;          //The mean number of collisions
double Temp_x;
double cm[LENGTH];
double t[LENGTH];
double dx;
double dxi;         // Random distance for diffusion on surface
double Rci;         // Mean diameter of grain cluster
int a,b;            //Counters for various loops
int L;              //Counter for the index of the Lth molecule
int N;              //Number of diffusion attempts
double random (void);
//double D273;
// T gradient 1.0 L/min
double out;

/* Temperatures of the COMPACT detector arrays. As an example,
two COMPACT detector arrays. The first detector was kept at room
temperature and along the second a negative temperature gradient
was applied. The fit function for the temperature gradient was
defined with origin. It has to be changed in the program for every
new gradient. A definition has to be made, from which detector on
there is a thin ice layer. */

for(xi=0; xi<32; xi++)
{
    t[int(xi)] = 294;
}

t[32]=267;
t[33]=266.9;
t[34]=266.8;
t[35]=266.7;
t[36]=266.6;
t[37]=266.6;
t[38]=266.5;
t[39]=266.4;
t[40]=266.3;
t[41]=266.2;
t[42]=266.1;
t[43]=265.3;
t[44]=264.09;

```

```

t[45]=262.31;
t[46]=260.1;
t[47]=257.39;
t[48]=254.11;
t[49]=250.22;
t[50]=245.67;
t[51]=240.24;
t[52]=234.2;
t[53]=227.36;
t[54]=219.67;
t[55]=210.78;
t[56]=201.51;
t[57]=190.63;
t[58]=179;
t[59]=165.86;
t[60]=151.96;
t[61]=136.86;
t[62]=120.53;
t[63]=102.9;

//Calculation of diffusion coefficient in the carrier gas, using
Gilliland's formula

D273=0.0044 * pow(273.15,1.5) * sqrt(1.0/(M1)+1.0/(M2)) /
((p)*pow((pow((M1)/(D1),1.0/3)+pow((M2)/(D2),1.0/3)),2));
cout << "D="; cout<< D273; cout<< "\n";

srand((unsigned int)time(NULL));

for(a=0; a<LENGTH; a++)
{
//Initialize array
cm[a]=0;
}

{

L=0; //Loop for I Molecules
do{
xi=0.; //Reset distance coordinate
ti=0.; //Reset total time
tf=0.; //Time of one jump
tai=0.; //Time of one adsorption cycle
tdi=0.;
tmi=0.;
dx=0.;
dxi=0.;
Rci=0.; //Time of one adsorption cycle
Roo=1.; //Roo is 1 for the first molecule to avoid error message
lifetime=(-log(1-random())/log(2))*halflife;

//-----

```

```

//-----Surface diffusion step-----
//-----

/* Loop for adsorption cycles while the total time is less than
lifetime. The temperature at the place of the molecule is
determined. If the position of the molecule is higher than detector
determined as limit for ice, then the physisorption enthalpy of ice
is used. In other cases, physisorption enthalpy for Au is used. The
random time an atom spends on the surface is determined, as also
the random distance it diffuses on the surface. If the random
distance exceeds the cluster barrier, then the chemisorption
adsorption enthalpy is taken for the simulation. */

do{
T1 = t[(int)xi];
if (xi > 55)
{
DHaphys = DHaphysIce;
}
else DHaphys = DHaphysAu;

// Calculation of random time an atom spends on the surface.

tmi=(-log(1-random()))*p0*exp((DHaphys)*(1e10)/(R*T1)) ;

// Calculate the mean distance the atom diffuses on the surface

dxi = sqrt(2 * KB*T1/h*(pow((2.87e-8),2))*exp(((Ed)*(-1e+10)/
(R*T1))*tmi);

// Calculate the mean diameter of the grain.

Rci = (-log(1-random()))*Rc;
if (dxi>Rci)
{
DHa = DHachem;
}else DHa=DHaphys;

// Calculate the diffusion

d=D273*pow((T1/273.15),1.5);
//cout<< "d"; cout<< ( d);cout << "\n";
//Calculate Ro
if(tai>0 and tf>0)
Roo=tai/(tf+tai); //THIS IS ALWAYS 1!!!

//-----
//-----
//-----

// Calculate the mean jump length in the gas

```

```

    Nm = ((2 * WIDTH*HEIGHT * d) / (Q*(Pstd/p)*(T1/Tstd)))+(f1 + f2 *
Roo + f3 * Roo*(Roo))*(Q*(Pstd/p)*(T1/Tstd)*HEIGHT*HEIGHT) /
        (WIDTH*HEIGHT*105 * d*(1+Roo)*(1+Roo));

    // Determine the random jump length

    Ni=-Nm*log(1-random());

    //Determination of the position of the atom in the column

    xi=xi+Ni;
    if(xi>LENGTH)
    {
    L++;
    out++;
    break;
    }

    // Calculate temperature in new position

    T2 = t[(int)xi];

    // Calculate the flight time

    tf=2 * WIDTH * HEIGHT * Ni / ((Q*(Pstd/p)*T1/Tstd)+(Q*(Pstd/p)*T2/
Tstd));
    ti=ti+tf;

    //Calculate the mean number of collisions

    vi = ((WIDTH + HEIGHT)*2 / (Q*(Pstd/p)*T2/Tstd)) * sqrt((R*T2)/
(2*PI*M1));

    // Determine the mean time the atom stays on the surface

    tm=p0*exp((DHa)*(1e10)/(R*T2));

    // Generate random time of a full adsorption cycle

    tai= (-vi) * tm * Nm * log(1-random());
    //Update total time
    ti=ti+tai;
    if(ti>=lifetime)
    {
    //add the final position of this molecule to the output-array
    (cm [(int)xi])++;

    L+=1;
    break;
    }
}while(ti<lifetime);

```

```

}while(L<I);
//DHaN++;
}

for (a=0; a<LENGTH; a++)
{
cout << "\n", cm[int(xi),a], a;
cout << cm[a] ;
};
cout << "\n" << "out \n" << out;
cout << "\n";
getchar();

// Output file

ofstream myfile;
myfile.open ("result.txt");
myfile<<"-----\n";
myfile<<"Date:           Time:           \n\n";
myfile<<"Number of molecules for each adsorption enthalpy: "<<I<<"\n";
myfile<<"Adsorption enthalpy on Au [kJ/mol]:      " << -DHaphysAu <<"\n";
myfile<<"Adsorption enthalpy on Ice [kJ/mol]:      " << -DHaphysIce <<"\n";
myfile<<"Chemisorptionenthalpy [kJ/mol]:          " << -DHachem <<"\n";
myfile<<"Diffusion energy [kJ/mol]:                " << Ed <<"\n";
myfile<<"Molecular weight of the gas:              " << M2 << "\n";
myfile<<"Density of carrier gas at boiling point:  " << D2 << "\n";
myfile<<"Molecular weight of the investigated species: " << M1<< "\n";
myfile<<"Density of the investigated species:      " << D1 << "\n";
myfile<<"Gas flow rate [sscm/s] :                  " << Q << "\n";
myfile<<"Pressure [bar]:                           " << p << "\n";
myfile<<"Period of oscillations of the molecule (1e-12): " << p0<< "\n";
myfile<<"Half-life of the nuclide [s]:             " << halflife << "\n";
myfile<<"Diffusion Coefficient at 273.15 K [cm^2/s] " << D273 << "\n";
myfile<<"Adsorption time [s]                       " << tai << "\n";
myfile<<"Mean jump lenght [cm]                     " << Nm << "\n";
myfile<<"Number of collisions                       " << vi << "\n";
myfile<<"Diffusion path                             " << dxi << "\n";
myfile<<"Column lenght [cm]:                       " << LENGTH <<"\n";
myfile<<"Height of the column [cm]                 " << HEIGHT <<"\n";
myfile<<"Width of the column [cm]                  " << WIDTH << "\n";
myfile<<"Width / heighth ratio                     " << phi << "\n";
myfile<<"Parameter in Golay's equation according to Poppe: f0:"<<f1<<"\n";
myfile<<"                                           f1:"<<f2<<"\n";
myfile<<"                                           f2:"<<f3<<"\n";

myfile<< "\n";
for(a=0; a<LENGTH; a++)
{
myfile << "\n", cm[int(xi),a], a;
myfile << cm[a] ;
};
};

```

```
myfile << "\n" << "out \n" << out;
myfile.close();
printf("\n");
}
double random (void) //returns a random number between 0 and 1
{
double a=1;
while(a==1) //a=1 leads to underflow in Tau. a MUST be between 0 and 0.9999
a=(double)rand()/(double)RAND_MAX;
return (double)rand()/(double)RAND_MAX;
}
```

A.2.3 Specifications gas purification cartridges

Hydrosorb® Gas Purification Systems **spectromol**

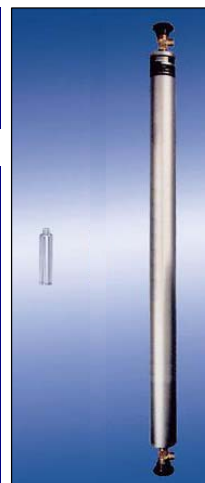
Hydrosorb® gas purification systems are designed for the removal of moisture from gas flows.

The applied process is based on **physisorption**:

Physisorption: moisture (and carbon dioxide) are physically bound to a porous mass and therefore permanently removed from the gas flow. Molecular sieve 5A is used as absorption material.

Hydrosorb®	
Applicable for	Rare gases, N ₂ , H ₂ , CO, CO ₂ , saturated HC halogenated HC, N ₂ O, O ₂ and compressed air
Removed contaminants	Moisture (and carbon dioxide)
Process	physisorption
Final purity	Moisture < 20 ppb

Hydrosorb®		
	Small cartridge	Large cartridge
Shield gas	Helium	Argon
Capacity	moisture 1 Ltr	Moisture 100 Ltr
Optical indication	no	no
Max. gas flow	1 m ³ /h	10 m ³ /h
Max. working pressure	10 bar ¹⁾	
Length	125 mm	1.170 mm
Diameter	29 mm	71 mm
Material	Aluminium	Aluminium
Remarks	-	Complete with 2 diaphragm type valves Connections: NPTF ¼"
Delivery	2-pack	single
Part no.	123326	123348



1) Small cartridges can be applied with high pressure housing PN200 for working pressure up to 200 bar.

For removal of oxygen and moisture:

see Oxisorb®

For removal of HC and oil vapour:

see Accosorb®

For removal of mercaptan, COS, SC, H₂S, SO₂, und NO:

see Sulfosorb®

For removal of Fluoride

see Excisorb®-F

For holders, purge systems and accessories:

see Spectromol accessories

Figure A.9: Specifications of Hydrosorb gas purifications cartridges of the company Spectromol. In the gas loop system we used the small cartridges.

Oxisorb[®] Gas Purification Systems **spectromol**

Oxisorb[®] gas purification systems are designed for the removal of oxygen and moisture from gas flows.

The applied processes are **chemisorptions** and **physisorption**:

Chemisorptions: Oxygen is chemically bound to the absorption material and therefore permanently removed from the gas flow. Silica gel with chromium oxide is used as absorption material. As a side effect, moisture is removed by physisorption.

Physisorption: Moisture is being physically bound to Silica gel and therefore removed from the gas flow.

Oxisorb [®]	
Applicable for	rare gases, N ₂ , H ₂ , CO, CO ₂ , saturated HC
Not applicable for	O ₂ , compressed air, non-saturated HC
Removed contaminants	oxygen, moisture
Process	O ₂ : chemisorptions H ₂ O: physisorption
Final purity	O ₂ < 5ppb H ₂ O < 30 ppb

Oxisorb [®]			
	Small cartridge		Large cartr.
	Aluminium	Glass	Aluminium
Capacity	O ₂ : 0,1 Ltr H ₂ O: 0,5 Ltr		O ₂ : 9 ltr H ₂ O: 45 Ltr
Optical indication	no	blue - brown	no
Max. gas flow	1 m ³ /h		10 m ³ /h
Max. working pressure	10 bar ¹⁾		
Length	125 mm	130 mm	1.170 mm
Diameter	29 mm	30 mm	71 mm
Material	Aluminium	Glass ²⁾	Aluminium
Remarks	-	-	Complete with 2 diaphragm type valves connections: NPTF 1/4"
Delivery	2-pack		single
Part no.	123325	123342	123311



¹⁾ Small cartridges can be applied with high pressure housing PN200 for working pressure up to 200 bar.

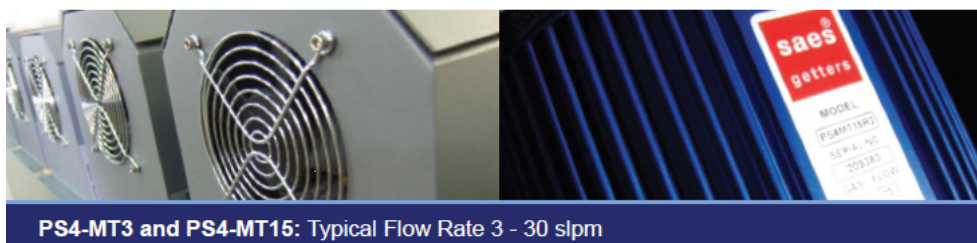
²⁾ Attention: Glass cartridges must be applied with a „splinter protection“ only!

For removal of moisture: see Hydrosorb[®]
 For removal of HC and oil vapour: see Accosorb[®]
 For removal of mercaptan, COS, SC, H₂S, SO₂, und NO: see Sulfosorb[®]

For removal of Fluoride see Excisorb[®]-F

For holders, purge systems and accessories: see Spectromol accessories

Figure A.10: Specifications of Oxysorb gas purifications cartridges of the company Spectromol. In the gas loop system we used the small aluminium cartridges. Since the year 2017 these specific Oxysorb cartridges are no longer available. This is why we now use cartridges of the company Agilent.



PS4-MT3 and PS4-MT15: Typical Flow Rate 3 - 30 slpm



Impurities Removed	Gases Purified		
	Rare Gases	Nitrogen	Hydrogen
H ₂ O	<1 ppb	<1 ppb	<1 ppb
O ₂	<1 ppb	<1 ppb	<1 ppb
CO	<1 ppb	<1 ppb	<1 ppb
CO ₂	<1 ppb	<1 ppb	<1 ppb
Total Hydrocarbons	<1 ppb	<1 ppb	N/A
H ₂	<1 ppb	<1 ppb	N/A
N ₂	<1 ppb	N/A	<1 ppb

Product specifications:

- MT3 (5 slpm Average Flow)
 - 50 slpm maximum flow rate (Nitrogen, Helium, Argon)
 - 30 slpm maximum flow rate (Hydrogen)
 - 3 slpm maximum flow rate (Xenon)
- MT15 (15 slpm Average Flow)
 - 75 slpm maximum flow rate (Nitrogen, Helium, Argon)
 - 50 slpm maximum flow rate (Hydrogen)
 - 9 slpm maximum flow rate (Xenon)
- High temperature alarm
- Outlet gas temperature < 50° C
- Average power consumption 125 W (MT3), 187 W (MT15)
- 0.003µm metal particle filter
- Life Status Sensor (Rare Gas and Nitrogen only)
- Bypass assembly
- Surface mountable enclosure with cooling fan

Dimensions:

- Height 86.4 cm (34 inches)
- Width 20.3 cm (8 inches)
- Depth 20.9-22.7 cm (8.25-8.94 inches)
- Weight 23-28 kg (50-61 lbs)

Optional equipment:

- 110-120 VAC or 220-240 VAC



Figure A.11: Specifications of the hot moisture getter of the company SAES (model: Mono Torr PS4-MT3-R-2).

Curriculum Vitae

Lotte H. L. Lens

Dec 12th 1988, Port-Elizabeth South Africa

Education

- | | |
|-------------------|--|
| Since Feb 2014 | PhD , Institut für Kernchemie, Johannes Gutenberg-Universität Mainz, DE.
Title: Advanced chemical investigations of the volatile element flerovium (Fl, Z=114) |
| Oct 2011-Jan 2014 | Master of Science , European Master in Nuclear Applications.
FH-Aachen, Campus Jülich, DE.
Title: Experimental investigations on RuO ₄ retention in a Filtered Containment Venting System.
GPA: 1.6 |
| Oct 2008-Aug 2011 | Bachelor of Science , Applied Chemistry, FH-Aachen, Campus Jülich, DE.
Title: Correlation of oxygen isotopes of water and ethanol to prove the addition of water to wine.
GPA: 1.5 |

List of Publications

- L. Lens et al., Online chemical study of Hg, Tl, and Pb on SiO₂ and Au surfaces at TASCA, GSI Sci. Rep. 2014, p 183 (2015)
- L. Lens et al., Improvements for superheavy element chemistry behind TASCA, GSI Sci. Rep. 2015, p 114 (2016)
- L. Lens et al., Online chemical adsorption studies of Hg, Tl, and Pb on SiO₂ and Au surfaces in preparation for chemical investigations on Cn, Nh, and Fl at TASCA, Radiochimica Acta, published online DOI: 10.1515/ract-2017-2914 (2018).

Talks and posters

- May 2015 Oral presentation at The 5th International Conference on the Chemistry and Physics of the Transactinide Elements, Urabandai Japan.
- Aug 2015 Oral presentation at GDCh-Wissenschaftsforum Dresden, Germany
- Oct 2015 Oral presentation at University Mainz Workshop, Vallendar Germany.
- Oct 2015 Oral presentation at Transactinide Separator and Chemistry Apparatus (TASCA) Workshop, Darmstadt, Germany.
- Aug 2016 Oral presentation at Transactinide Separator and Chemistry Apparatus (TASCA) Workshop, Darmstadt, Germany.
- Aug 2016 Poster presentation at 9th International Conference on Nuclear and Radiochemistry, Helsinki, Finland.
- Feb 2017 Invited Talk at Seminar für Kern- und Radiochemie, Mainz Germany.
- Aug 2017 Invited Talk at 254th American Chemical Society (ACS) National Meeting and Exposition, Washington D.C., USA.
- Sep 2017 Oral presentation at GDCh- Wissenschaftsforum, Berlin Germany.
- Feb 2018 Invited Talk at NUSTAR Annual meeting 2018, Darmstadt Germany.
- Nov 2018 Invited Talk at 4th International Conference on Application of Radiotracers and Energetic Beams in Sciences (ARCEBS), Kolkata, India..